Doctoral Thesis

Versatile Optical Imaging Technique for Dynamic Monitoring and Quantitative Analysis in Tissue Engineering

Yujin Ahn

Department of Biomedical Engineering

Graduate School of UNIST

2020

Versatile Optical Imaging Technique for Dynamic Monitoring and Quantitative Analysis in Tissue Engineering

Yujin Ahn

Department of Biomedical Engineering
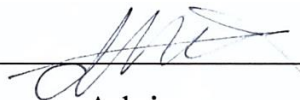
Graduate School of UNIST

Versatile Optical Imaging Technique for Dynamic Monitoring and Quantitative Analysis in Tissue Engineering

A thesis/dissertation
submitted to the Graduate School of UNIST
in partial fulfillment of the
requirements for the degree of
Doctor of Philosophy

Yujin Ahn

12. 09. 2019

Approved by

_____

Advisor

Woonggyu Jung

Versatile Optical Imaging Technique for Dynamic Monitoring and Quantitative Analysis in Tissue Engineering

Yujin Ahn

This certifies that the thesis/dissertation of Yujin Ahn is approved.

12. 09. 2019

signature

_____

Advisor: Woonggyu Jung

signature

_____

Thesis Committee: Hae-Kwang Lee

signature

_____

Thesis Committee: Jae Hyun Jung

signature

_____

Thesis Committee: Sang Woo Kim

signature

_____

Thesis Committee: Hyun-Wook Kang

signature

_____

Thesis Committee: Jung-Hoon Park

ABSTRACT

Many researches in the tissue engineering are investigating the development of technologies that have covered a broad range of applications and closely associated with the tissue regeneration and replacement of lost or damaged tissues as well as tissue manipulation. However, there are challenges regarding monitoring and assessing outcomes to analyze a variety of morphological and structural changes in tissue engineering applications. Most tissue engineering studies have utilized histopathological techniques for morphological analysis and evaluation of the tissues. Although the conventional methods provided a high definition and clear distinction under optical microscopy, it has still limitations in the visualization of tissue constructs without destruction of the tissues. Also, these methods have not allowed a volumetric assessment and functional information. Due to the destructive process and limited information in a two-dimensional approach, the conventional methods were difficult not only to analyze the specimens at continuous time points but also to compare inconsistencies of the results between different samples. For these reasons, there are clear needs for the development of advanced optical imaging techniques available for non-invasive and consistent observation and quantitative analysis in tissue engineering applications.

Optical coherence tomography (OCT) has emerged as appropriate candidate for studying tissue morphology dynamically and quantitatively. OCT equips optimal imaging characteristics for dynamic monitoring because it offers cross-sectional, high-resolution, real-time tissue imaging in a non-invasive manner. Unlike most optical imaging techniques, OCT does not require any contrast agent or labeling process even it provides a deep penetration depth of about 2 mm in the tissue. Here, we utilized OCT technique to carry out application for the tissue engineering research ranging from the observation of biological tissues, dynamic monitoring, and quantitative analysis, as well as fabrication of image-guided engineered tissue. In the chapter 2, we utilized 3D OCT imaging to observe the tissue regeneration after laser irradiation, epidermal biopsy, and skin incision in *in vitro* and *in vivo* skin model. We utilized OCT system to monitor and analyze the wound recovery process after laser irradiation on the engineered skin. Also, we presented a quantitative evaluation of drug efficiency that affect the wound recovery on the engineered skin model after epidermal biopsy. Next, we analyzed quantitatively a recovery process of the wound width and depth in skin incised rat model *in vivo* with tissue adhesives treatment under the OCT monitoring. In the chapter 3, we utilized optical coherence microscopy (OCM) imaging modality to observe and quantitatively analyze the morphological changes of biological tissue in subcellular level. We introduced depth trajectory-tracking technique to acquire homogenous quality OCM images regardless of the height difference of the sample surface. Also, we developed the serial block-face OCM (SB-OCM) system to acquire the whole tissue information by repeating tissue sectioning and image acquisition using the serial block-face imaging technique. In the chapter 4, we developed the hand-held probe based portable OCT system for

convenience in human target studies. We monitored and quantitatively analyzed various changes in the human skin using the hand-held probe based portable OCT system. Especially, we studied quantitative analysis of human skin wrinkle in terms of depth and volume as well as roughness parameters in comparison with conventional platforms. In the chapter 5, we suggested the feasibility to fabricate the engineered tissue based on a volumetric information of optical imaging. Here, we studied a fabrication of wrinkle mimicked engineered skin for anti-aging assessment and a protocol of imaging guided personalized engineered cornea for cornea transplantation. In conclusion, we confirmed that OCT system was able to provide various quantitative information from the biological tissues by its advantages such as high-resolution, non-invasive, label-free, deep penetration depth with real-time imaging. These characteristics of OCT imaging enables the quantitative analysis of tissue recovery and replacement as well as tissue manipulation in the tissue engineering research.

CONTENTS

LIST OF FIGURES AND TABLES

CHAPTER 1. Introduction

1.1 Research Background

Optical Imaging in Tissue Engineering

Many kinds of researches in the tissue engineering fields are investigating the development of new technologies that have covered a broad range of applications and closely associated with the regeneration and replacement of lost or damaged tissues as well as manipulation of partial or whole tissues [1, 2]. However, there are distinct challenges regarding monitoring and assessing outcomes to analyze a variety of changes such as a morphological and structural transition from interfaces between biomaterials, cells, and tissues found in tissue engineering applications [3, 4]. Traditionally, most tissue engineering studies have utilized histological and immunohistochemical techniques for morphological analysis and evaluation of the tissues. Although the conventional methods provided a high definition and clear distinction under optical microscopy, it has still limitations in the visualization of tissue constructs without destruction of the tissues [5]. Also, these methods have not allowed a volumetric assessment and provision of functional information, especially in the case of preclinical and clinical approaches. Due to the destructive process and limited information in a two-dimensional approach, the conventional methods were difficult not only to observe and analyze the specimens at continuous time points but also to compare inconsistencies of the results between different samples as well as different regions in the same samples. For these reasons, there are clear needs for the development of advanced optical imaging techniques available for non-invasive and consistent observation and quantitative analysis in tissue engineering applications.

Optical imaging techniques have developed to acquire morphological and structural information in biological tissues with steadily enhanced and improved resolution, penetration depth, and image sensitivity as well as specificity [6-8]. The optical imaging techniques have received attention in the tissue engineering fields because it has many advantages in comparison with medical imaging modalities such as inexpensive, portable, non-invasive, and providing morphological and functional information with high-resolution and various contrasts. Also, optical imaging inherently offers many advantages which are well suited for evaluating the study of cell and tissue engineering: (1) higher spatial resolution and sensitivity, (2) tissue and cellular information based on scattering, absorption, and fluorescence, and (3) availability of contrast agents for specific targeted biomarkers. In the tissue engineering fields, the most important aspect of optical imaging is to suggest non-a destructive procedure to evaluate the tissue characteristics at continuous time points with high spatial resolution up to the cellular level. The optical imaging is based on the signal acquisition from light-tissue interactions in the case of the reflection, transmission, scattering, and absorbance when the light

propagated into the biological tissues. The characteristic of imaging modality is determined depending on light source properties such as wavelength, bandwidth, and intensity as well as optics specifications.

Optical microscopy, which is the representative microscopic imaging modality, has mainly used for observation and analysis of tissue morphologies and structural organizations in tissue engineering fields. The optical microscopy includes various imaging modalities and a wide range of techniques, and it would be classified in terms of image acquisition mechanism. Among these techniques, confocal microscopy and multiphoton microscopy have been widely utilized to acquire various information of biological tissues with a chemical composition such as fluorescence markers. The confocal microscopy utilized in various applications for evaluation of normal or abnormal tissues because it provides a high-resolution image of *ex vivo* and *in vivo* tissues for morphological and structural investigation with a penetration depth of around 200 μm [9, 10]. It utilized the pinhole where is located at the focus plane in front of the detector to block the light outside the focal region, therefore the signals only from the imaging plane can be acquired by the detector. The multiphoton microscopy, which is a nonlinear optical imaging modality to overcome the diffraction limit, enables long-term imaging without photobleaching and photodamage phenomena and high signal-to-noise ratio with a high penetration depth increased up to 500 μm compared to the confocal microscopy [11]. Unlike the confocal microscopy that utilized the pinhole to block out of focused light, the multiphoton microscopy acquired the signals based on multiphoton absorption to reduce optical attenuation and background noises by multiple photons of longer wavelengths. However, although many advanced optical imaging methods have emerged for the tissue engineering research, most applications of optical imaging methods still have limitations in terms of penetration depth and three-dimensional visualization to acquire volumetric information of tissue morphologies.

1.2 Research Purpose and Motivation

Visualization of three-dimensional structure of tissues is very critical to quantitatively analyze the morphological changes of tissue in the tissue engineering applications. Even though there are clear needs for high-resolution and deep tissue imaging capability in optical imaging technique, it has inherent restrictions to enhance the light penetration into the tissue due to the high scattering of turbid biological specimens. Here, we utilized the optical coherence tomography (OCT) and its expanded technique for continuous monitoring and volumetric assessment in tissue engineering studies. Among various optical imaging modalities, OCT is the most emerging imaging technology which allows real-time cross-sectional imaging with high resolutions. OCT could be a very promising technique which has the potential to be used as an adjunct to histological tissue observation when it is not practical to take specimens for histological processing, when large areas of tissue need investigating, or when rapid microscopic imaging is needed.

CHAPTER 2. Optical Coherence Tomography for Wound Healing

2.1 Optical Coherence Tomography (OCT)

2.1.1 Summary of OCT

Optical coherence tomography (OCT) is a tomographic imaging-based diagnostic modality that provides a high-resolution, deep penetrated cross-sectional image of the surface and internal morphological microstructures in the biological tissues using the measurement of backscattered light and interfered signals. Among the various optical imaging systems, OCT uses the range of near infrared light and is appropriate as the morphological imaging modality in terms of providing precise real-time morphological information. The OCT is widely used in various fields, such as the biological, analytical, and medical studies; it realizes real-time cross section images of biological samples with high-resolution and deep penetration depth [12, 13]. In this way, OCT enables non-invasive, painless imaging technique on samples. In addition, OCT provides high-resolution two-dimensional cross-sectional images as well as three-dimensional volumetric imaging using a rapid transverse scanning technique.

The main operating principle of OCT is based on the Michelson interferometer which creates two different light paths, one of the reference arm and the other on the image acquisition unit called the sample arm. The light source emits light divided by the beam splitter or fiber coupler. Each beam propagated to the sample or target and reference mirror following a given optical path. After the beam returns to the beam splitter, the backscattered light from each pathway generated optical fringe patterns. And this signal detected by a spectrometer consisting of a transmission type diffraction grating and line scan camera. The captured interference signal from the line scan camera was digitized by a frame grabber, processed by FFT, and converted to a log intensity profile for plotting the depth information which is the axial scans called OCT A-line.

2.1.2 OCT system specification

In this study, we utilized spectral domain OCT (SD-OCT) and swept source OCT (SS-OCT) for monitoring and quantitatively analysis of morphological changes in biological tissues [14, 15].

Spectral domain OCT(SD-OCT)

A super-luminescent diode (SLD, EXALOS Inc.) with a 50 nm full-width half-maximum spectral bandwidth at the center wavelength of 840 nm, was incorporated into the SD-OCT system, which provided ~6 μm axial resolution in the tissue. The emitted light from SLD was coupled into the 2×2 fiber coupler and divided into two optical paths, reference and sample arm. The sample arm consisted of a collimator, beam expander, dual-axis galvanometer scanners and an objective lens to image tissue specimens with ~15 μm lateral resolution. The reflected lights from the sample and reference arms were interfered with the 2×2 fiber coupler and detected by a customized spectrometer consisting of a transmission type diffraction grating (1145 lines/mm, Wasatch Photonics), a focusing lens, and a 1024-pixel line scan camera (SUI Goodrich). The captured interference signal from the line scan camera was digitized by a frame grabber (National Instruments), processed by FFT, and converted to a log intensity profile for plotting the depth information. OCT images accumulated by 1000 axial scans were visualized at a rate of ~20 frames/s. The 3D OCT image was constructed by a 500 OCT image set. The corresponding speed for a single three-dimensional volumetric image was ~25 second.

Swept-source OCT (SS-OCT)

The swept source laser (Axsun Technologies, Inc., US) integrated into the SS-OCT system has 1,310 nm center wavelength and 110 nm tuning range with a sweep rate of 20 mW and axial resolution of ~ 8 μm in tissue. The light emitted from the swept source laser moved along the fiber optics based on Mach-Zehnder interferometry and it split into sample arm and reference arm following fiber coupler and a circulator. The sample arm responsible for imaging of the skin sample was composed of a collimator, two-axis galvanometer scanner, and objective lens providing lateral resolution of ~ 15 μm in tissue. Reflected light from the sample and reference arm were combined and these interference signals converted to an electrical signal by a balanced photodetector (PDB450C, Thorlabs Inc., US). The electrical signals digitized by a digitizer (ATS9350, AlazarTech Inc., Canada), and then an intensity-based image was generated. The intensity-based 1D arrays called A-line images were accumulated using a galvanometer scanner in the sample arm to reconstruct a 2D OCT image which is the cross-sectional image of the sample. Also, a 3D OCT image which has volumetric information of the skin can be obtained by an accumulation of the 2D OCT images using the scanner on the same way.

2.2 OCT Monitoring in In Vivo and In Vitro Skin Model

Optical coherence tomography (OCT) has emerged as the most appropriate candidate for studying skin morphology dynamically and quantitatively. OCT equips optimal imaging characteristics for dynamic skin monitoring because it offers cross-sectional, high-resolution, real-time tissue imaging in a non-invasive manner [16, 17]. Unlike most optical imaging techniques, OCT does not require any contrast agent or labeling process even it provides a deep penetration depth of about 2mm in the tissue. Recently there have been dramatic advances in OCT technology in terms of imaging speeds. Thus, current high-speed OCT systems present three-dimensional volumetric imaging in real-time which is suitable for applying to in vivo study with less motion artifact. To date, OCT has been intensively utilized in biomedical applications for diagnosing a variety of tissue abnormalities, but only a few OCT studies have been specifically targeted for wound healing monitoring, despite a clear need and enough potential.

2.2.1 Engineered Skin Fabrication

First, we fabricated engineered skin to observe the regeneration process of skin wounds in the *in vitro* skin model with OCT imaging. Engineered skin (or artificial skin) is a three-dimensional reconstructed scaffold including skin cells and skin constituents such as collagen and elastin. It is also called skin equivalent or reconstructed skin because it consists of fibroblast and keratinocytes that exhibit similar structural and functional properties to the actual skin. Engineered skin is used not only for replacement or regeneration of damaged skin such as burn and wound but also for various studies such as skin physiology research, irritation and efficacy assessment.
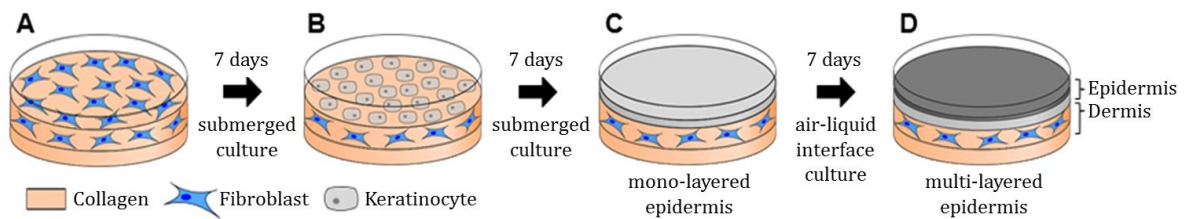
Figure 2-1. Schematic of engineered skin preparation procedure. (A) Dermal layer of engineered skin was composed of acellular dermis containing collagen, and cellular dermis containing collagen and fibroblast. (B, C) After seven days, keratinocytes were cultured on the surface of a dermal layer. The epidermal monolayer formed as keratinocytes were proliferated and differentiated. After monolayer development, the submerged medium removed except the bottom of engineered skin for air exposure. (D) The epidermal multi-layer constructed using air-liquid interface culture.

In this study, customized engineered skins consisting of dermal and epidermal layers were developed as presented in Figure 2-1. The major fabrication steps of engineered skin include (1) the construction of the acellular layer with collagen compound, as well as the cellular layer containing fibroblast for a dermal layer, (2) seeding of keratinocytes on the second dermal layer, and (3) proliferation and differentiation for an epidermal layer [18]. Through the above procedure, two dermal layers were cultured in a medium for seven days at 37 °C, 5 % CO_2, and the epidermal layer was seeded by human epidermal neonatal keratinocytes on the second dermal layer. To proliferate the keratinocytes, the layered skin was then submerged in a culture medium for another seven days. Lastly, the engineered skin was completed after the procedure of air exposure for epidermal differentiation.
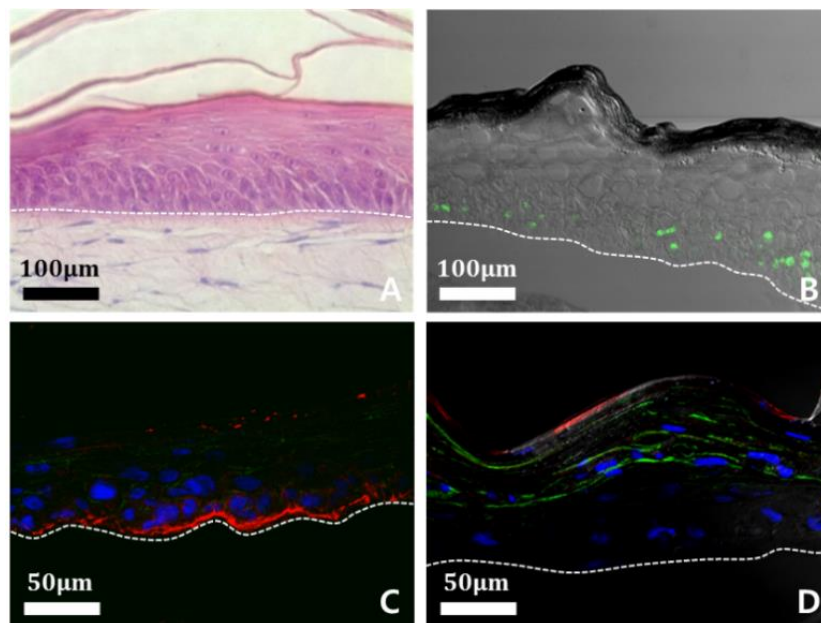
Figure 2-2. Analysis of constitutive of engineered skin structures using a confocal microscope; epidermis is above the white dotted line and dermis is below the line. (A) Cross-sectional H&E stained image of engineered skin. (B) Proliferation of keratinocyte is shown by using proliferation marker, Ki-67 (green). (C) Epidermis-dermis junction is shown by using junctional protein, Laminin-5 (red). (D) Differentiation of keratinocyte is shown by using differentiation markers, involucrin (green) and filaggrin (red). Nucleus of keratinocyte demonstrates using DAPI staining method (blue).

Figure 2-2 shows the H&E stained engineered skin structure that is a proliferation of the epidermis with keratinocyte and of the dermis with fibroblast. The histology indicates that the engineered skin has two major layers (epidermis and dermis), distinguishable by the extent of staining. The multi-layers of the epidermis are composed of stratum corneum and epidermal keratinocyte. The dermis is located below the epidermis multi-layers and is composed of dermal fibroblasts and an organized extracellular matrix. Figure 2-2(B)-(D) shows confocal microscopy images of the engineered skin.

Figure 2-2(B) represents the proliferation of keratinocyte, which is a primary component of the epidermis basement using a proliferation marker, Ki-67. The green color of Ki-67 demonstrates that the engineered skin has a well-grown epidermis, and it shows a usual pattern of epidermis stem cell proliferation. In Figure 2-2(C), the junctional protein, Laminin-5 strongly attaches to a junction protein that is mainly expressed in the epidermis-dermis junction. The clear red color indicates that the engineered skin grows in a similar way to human skin. Figure 2-2(D) represents the differentiation of keratinocyte in engineered skin using differentiation markers; involucrin and filaggrin. Those markers are an indicator of how similar the engineered skin is to human skin. The blue marker, made by DAPI (4', 6-diamidino-2-phenylindole) staining shows the nucleus of keratinocyte. It demonstrates that the nucleus of keratinocyte gradually disappears to the top of the epidermis as differentiation of keratinocyte is processed. These engineered skin models which proven biologically was used to monitor the regeneration process of skin wound after epidermal biopsy and laser irradiation.

2.2.2 Quantitative Analysis of Laser-treated Engineered Skin

Research Motivation

As laser technology is advanced, laser therapy becomes a common method for treating various dermatological troubles [19]. The laser treatment offers effective care of acne and wrinkle in the skin, and it has been extensively used in medical and cosmetic fields. Current laser treatment often requires the procedure to observe laser irradiated skin dynamically and quantitatively [20, 21]. It is because frequent and quantitative observation of skin prevents side effects such as hyperpigmentation, redness, and burning [22, 23]. However, there exists no optimal method to characterize the variation of skin before and after laser therapy. In order to study wound healing processes in laser irradiated tissue, various monitoring methods have been tried. Histology is still the golden standard for investigating tissue structure in the biological and medical field, but it has inherent limitations when applied to dynamic studies due to its destructive treatment of specimens. Optical imaging techniques, including reflectance confocal microscopy, fluorescence microscopy, and second harmonic microscopy, have also been considered as promising tools for investigating structural change of tissue. Each optical imaging modality has clearly visualized biological components such as keratinocyte, melanocyte, and collagen, and was applied to investigate the collagen-elastic fiber interaction during a photo-aging process [11, 24-26]. Even though most microscopic techniques provide high-contrast, and cellular resolution imaging, there still remains some critical restriction in monitoring laser irradiated tissue regions due to its shallow penetration depth and narrow field of view. Considering that the depth of laser treated regions is more than 1 mm, most optical imaging technologies are beyond deep tissue imaging.

In this study, we utilized 3D optical coherence tomography (OCT) to observe light-tissue interaction and tissue regeneration after laser irradiation. OCT is a cross-sectional imaging tool that visualizes high-resolution tissue structure, non-invasively [16]. Thus, it is very suitable to monitor skin generation at the same site over time [20, 21]. Our interest is to understand laser tissue interaction and to evaluate the healing process of laser irradiated tissue. Here, we demonstrate the feasibility of three-dimensional OCT for quantitative tissue monitoring after laser irradiation. In this study, we hired engineered skin which reflected that animal study is currently prohibited in the cosmetic field due to ethical issues. Engineered skin is also a good research platform to evaluate wound healing processes due to its good manipulability and an experimental reliability that is higher than animal models. The customized engineered skin was fabricated to mimic the diversity of human skin and was then irradiated at various laser parameters. Quantitative recovery over time was investigated by OCT imaging and intensive image processing.

Laser irradiation and OCT imaging

The injury model was produced by laser ablation on the engineered skin. The fractional CO_2 laser resurfacing (Lutronic Co., Ltd) was used by adjusting several irradiation conditions, such as pulse energy, spot density, and the irradiation area. The pulse energy of the laser for the major experiment was treated at 40, 80, and 120 mJ/cm^2. The laser-irradiated an 8 mm circular region, and the corresponding spot density was 100 $spots/cm^2$.

We prepare two groups of engineered skin samples which were irradiated by resurfacing laser to compare both OCT data and fixed reference data. After laser irradiation, the first group was cultured continuously in a medium to observe the skin regeneration process every 6 hours using the 3D OCT system. The second group was fixed by using formalin solution every 6 hours. For histological analysis, engineered skin samples were embedded in optimal cutting temperature compound for cryostat sectioning, or in paraffin for hematoxylin and eosin staining. Each sample slice was captured using a digital camera integrated optical microscope.
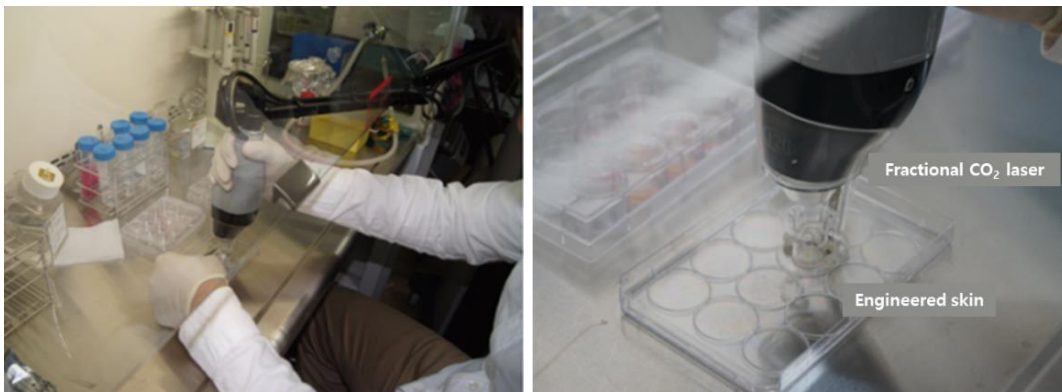
Figure 2-3. Laser irradiation by fractional CO_2 laser on a surface of the engineered skin for monitoring of wound regeneration.

Correlation study of wound regeneration

The recovery process of laser-treated skin was monitored by OCT and compared to corresponding histology and microscopic images over time. Figure 2-4 shows the representative correlation data set over 18 hours after laser irradiation. Conventional observation using a microscope and histology provides the surface view and cross-sectional view, respectively. OCT images offer both surface and cross-sectional morphology together and show strong similarities to images acquired from existing methods. All OCT images were acquired from the same engineered skin; thus, it was possible to identify the dynamic variation of very thin remaining tissue structure, after laser irradiation, without damage, as presented in Figure 2-4. The image acquisition time of the OCT system was fast enough to monitor and maintain the engineered skin while minimizing denaturation.

In the *en-face* OCT image, shown in column C of Figure 2-4, the laser-irradiated regions on the engineered skin are denoted as round spots with regular spacing. The structure of *en-face* OCT images including spots and even the scratch (indicated by an arrow) was strongly coincident with light microscopic images as presented in column A and B of Figure 2-4. The boundary of irradiated spots in *en-face* OCT images has gradually recovered over time, and adjacent irradiated spots even in the same engineered skin have a different healing process. This indicates that the tissue recovery depends on the location of engineered skin and is also very sensitive to tissue structure as well as irradiation conditions such as exposure angle and distance. In the B-mode OCT image, the skin layers and laser-irradiated zone were identified [14].
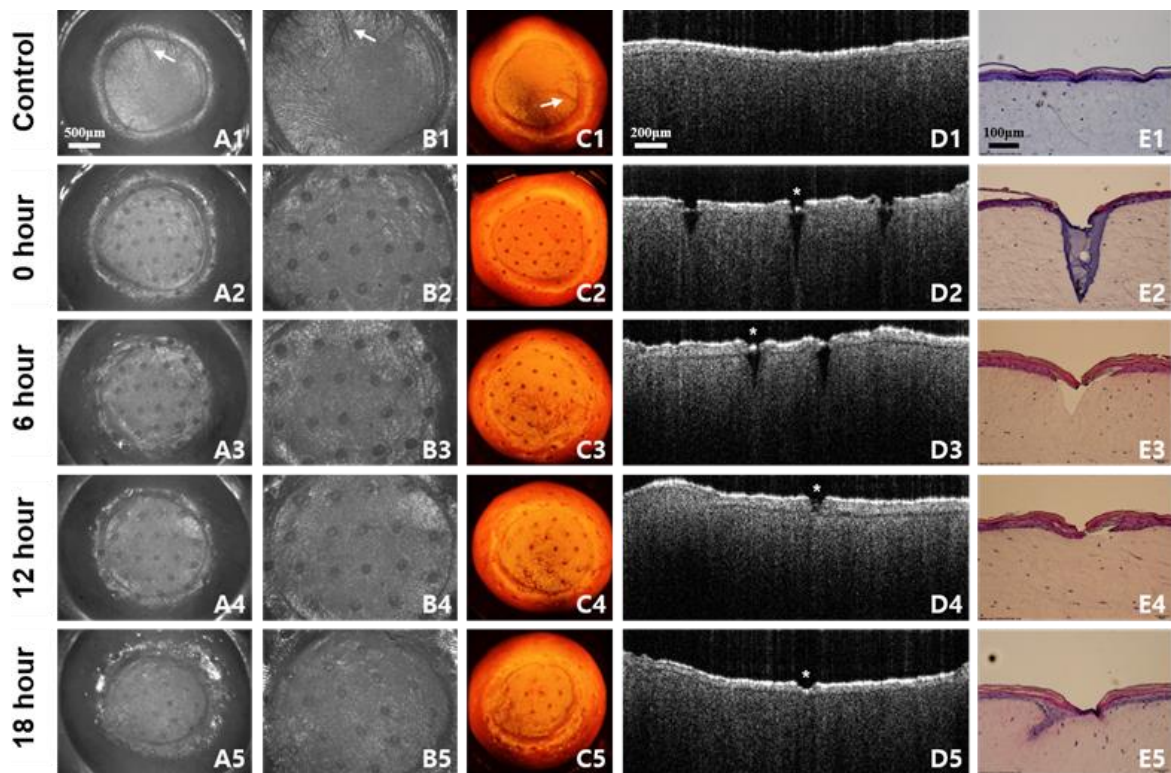
Figure 2-4. The recovery process of engineered skin over 18 hours after laser irradiation. The samples are irradiated by 40 mJ/cm^2 laser power monitored every 6 hours. No laser irradiated samples (A1-E1) show the difference compared to laser irradiated samples (A2-E2). (A, B) Microscopic images are corresponding to 3D OCT images in (C). The white arrow indicates the correlation of 3D OCT images compared to microscope images. (D) Cross-sectional 2D OCT images demonstrate similar aspects of H&E stained images in (E). The white star indicates the corresponding location of OCT image to H&E stained image.

As shown in Figure 2-4(D2, E2), the collagen of the engineered skin was denatured, and a V-shaped wound was formed immediately after the laser irradiation. After 6 hours, the stratum corneum and epidermis were recovered as shown in Figure 2-4(D3, E3). Our results show that the irradiated zone

in the dermis recovered more slowly than that in the epidermis at a given irradiation condition and tissue structure. The irradiated zone was filled and recovered within 24 hours. The research protocol including a comparison study, shown in Figure 2-4, was repeated for the entire experiment.

Wound segmentation for quantitative analysis

To quantify the skin regeneration process, we developed an automatic segmentation algorithm using MATLAB, as shown in Figure 2-5. The automatic segmentation involves three steps: (1) pre-filtering, (2) hole detection, and (3) hole estimation. Firstly, we applied the Laplacian of Gaussian filter on an original gray-scale OCT image to remove noise. Using the Otsu's threshold method, the filtered gray-scale image is converted into binary values. The connected component labeling and the morphological close operation are used to find the gross morphology of the irradiated skin. These two operations are repeated until the skin morphology no longer changes. Next, we apply the Sobel operator to detect the boundary while preserving the boundary of the skin damaged due to laser irradiation. Using the curve fitting method, we estimate the original skin boundary before laser irradiation in which the skin does not have holes. Combining these two boundaries provides us the enclosed objects which can be holes or local fluctuations such as wrinkles. Regarding the depth of each detected object, we determine whether the detected object is a hole or not. Lastly, after detection, the volume of a hole is measured by repeating the routines as mentioned above for an entire image set and adding the areas together.
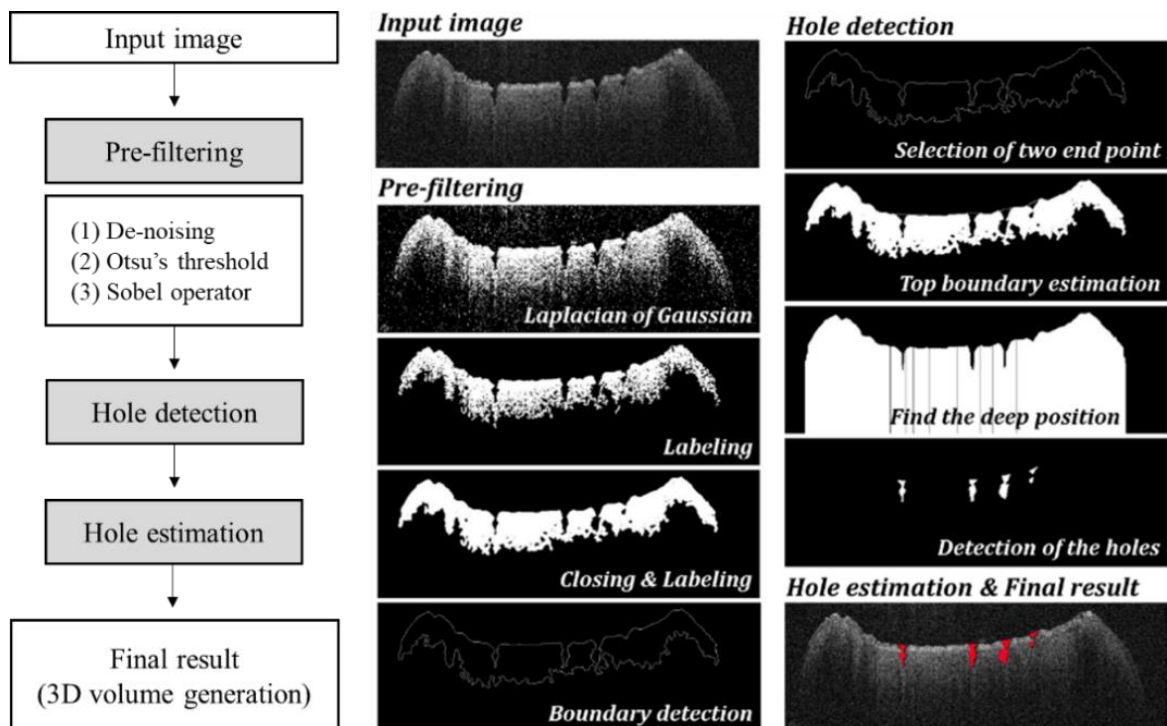
Figure 2-5. The automatic segmentation algorithm for quantitative analysis of skin regeneration. The whole process is consisted of 'Pre-filtering', 'Hole detection', and 'Hole estimation'.
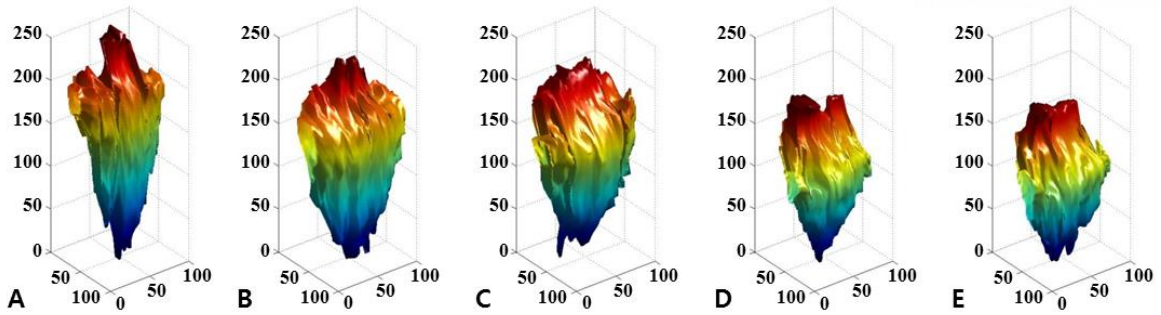
Figure 2-6. Reconstructed volumetric image of irradiated hole. The images were reconstructed by automatic segmentation. The engineered skin was irradiated by 80 mJ/cm^2 laser power and monitored every 6 hours; (A) 0 hours, (B) 6 hours, (C) 12 hours, (D) 18 hours, and (E) 24 hours after laser treatment was conducted.

All the cross-sectional images corresponding to the hole were segmented, and they were accumulated to reconstruct a three-dimensional hole according to a corrected value between the voxel and actual distance. Figure 2-6 shows the result of the image reconstruction and visualizes intuitive and quantitative data of the wound regeneration process. Consequently, the values for the wound volume are automatically calculated to observe the morphological change, and the results are quantified and visualized for each observation time of 6 hours.

Wound healing: Epidermis thickness of engineered skin
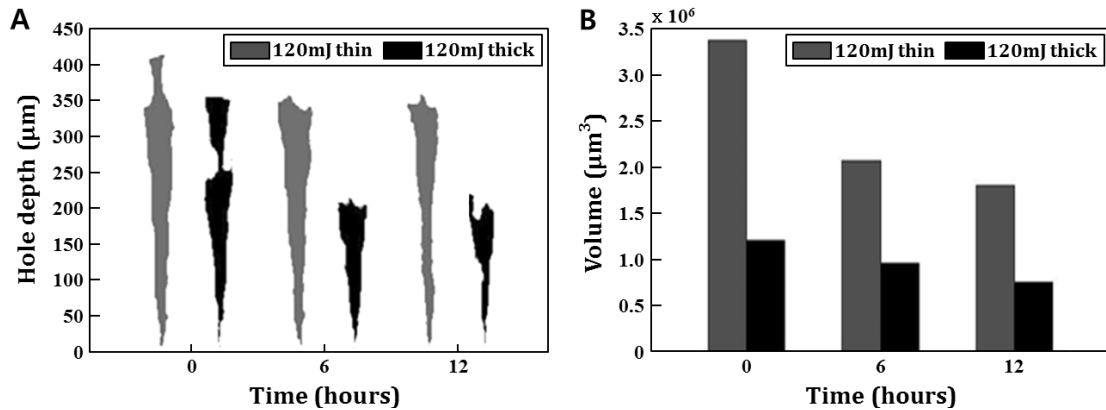
Figure 2-7. Comparison of the relationship between epidermis thickness and wound depth with volume. The grey one indicates thin epidermal engineered skin, and the dark one is thick epidermal skin. (A) The thin epidermal skin has an epidermal layer of 50 μm, and the initial penetrated hole depth after layer irradiation is about 400 μm. In thick epidermal skin, the epidermal thickness is about 100 μm and the initial penetrated hole depth is about 350 μm. (B) The initial hole volume after irradiation is 3.3 million μm^3 in thin epidermis skin and 1.2 million μm^3 in the thick sample.

We evaluated the laser-induced wound healing in the different engineered skins[14]. In this study, the two types of engineered skin with different epidermis thicknesses were prepared and treated at the same laser dosage, 120 mJ/cm^2. The laser-irradiated region was then imaged with 3D OCT, segmented, and its morphological change at different time points were compared. The segmented OCT image acquired from the central location of the laser-treated zone of each skin is visualized in Figure 2-7(A). The OCT image of the wound shows that light energy penetrated more deeply at the thin epidermal skin. OCT images also show that the width of an irradiated zone at the epidermal layer is narrower than that at the dermal layer. Irradiated light initially interacted with the epidermis of skins which has a role as resistance against light energy. Through this experiment, we confirm that the epidermal layer has higher resistance compared to the dermal layer when the light propagates into the engineered skin. The reason appeared different value of resistance is that stratum corneum, the outmost layer of the epidermis, has a fully differentiated and tightly bound keratinocyte structure embedded in the intercellular lipids [27]. This unique structure called, 'bricks and mortar' form a physiological barrier of the skin and regulates the entrance of the external substances. Due to the physical characteristics of stratum corneum, the thickness of epidermis affects the degree of skin penetration by the light. Experiment results also show that the irradiated zone of thin recovered faster while filling the area compared to thick epidermal skin. However, the entire wound healing process of thick epidermal skin was completed earlier than that of thick epidermal skin. This means that wound recovery time is proportional to the area of the irradiated zone.

Wound healing: Exposure energy of laser irradiation

We investigated the wound healing process in varying laser exposure power [14]. To maintain experimental analogy, engineered skins were pre-scanned by OCT and their structures were analyzed. Engineered skins with around 70 µm epidermal thickness were selected, and irradiated by three different laser energy levels, 40, 80 and 120 mJ/cm^2. Finally, sorted skins were then imaged by OCT again to monitor tissue recovery every 6 hours for a day. For the quantitative analysis of the wound zone, the same image processing protocol described in the previous chapter was applied and repeated.

As presented in Figure 2-8, the laser-irradiated zone of engineered skins was proportional to the light energy applied. Our results showed that the recovery time of engineered skin varied by the amount of light energy. In 120 mJ/cm^2 dosage, the recovery of the epidermis was faster than in the dermis layer. On the other hand, the tendency of recovery at the dermis and epidermis was opposite when the relatively low energy, 40 mJ/cm^2, was applied. In 80 mJ/cm^2 dosage, the recovery process was very slow for the first 6 hours and then tends to be healed steadily every hour. As shown in Figure 2-8(B1), the recovery time in 80 mJ/cm^2 has a uniform healing process at each epidermal and dermal layer. Through experimental results, we found that light energy influences the variation of regional recovery between the dermis and epidermis. This effect indicates that the adjustment of laser exposure energy is essential to adjust balanced tissue recovery at skin layers as well as the tissue recovery time.

Considering the morphological change of a segmented OCT image, we also found that the recovery process of the laser-irradiated zone is more active in the horizontal direction than in the vertical direction. As mentioned, the advantage of OCT in wound healing studies is dynamic imaging capability. Thus, the graphical visualization of the healing process using volumetric OCT images offers comprehensive knowledge for better understanding tissue recovery and unique information, such as regional observation, which cannot be acquired by existing monitoring tools.
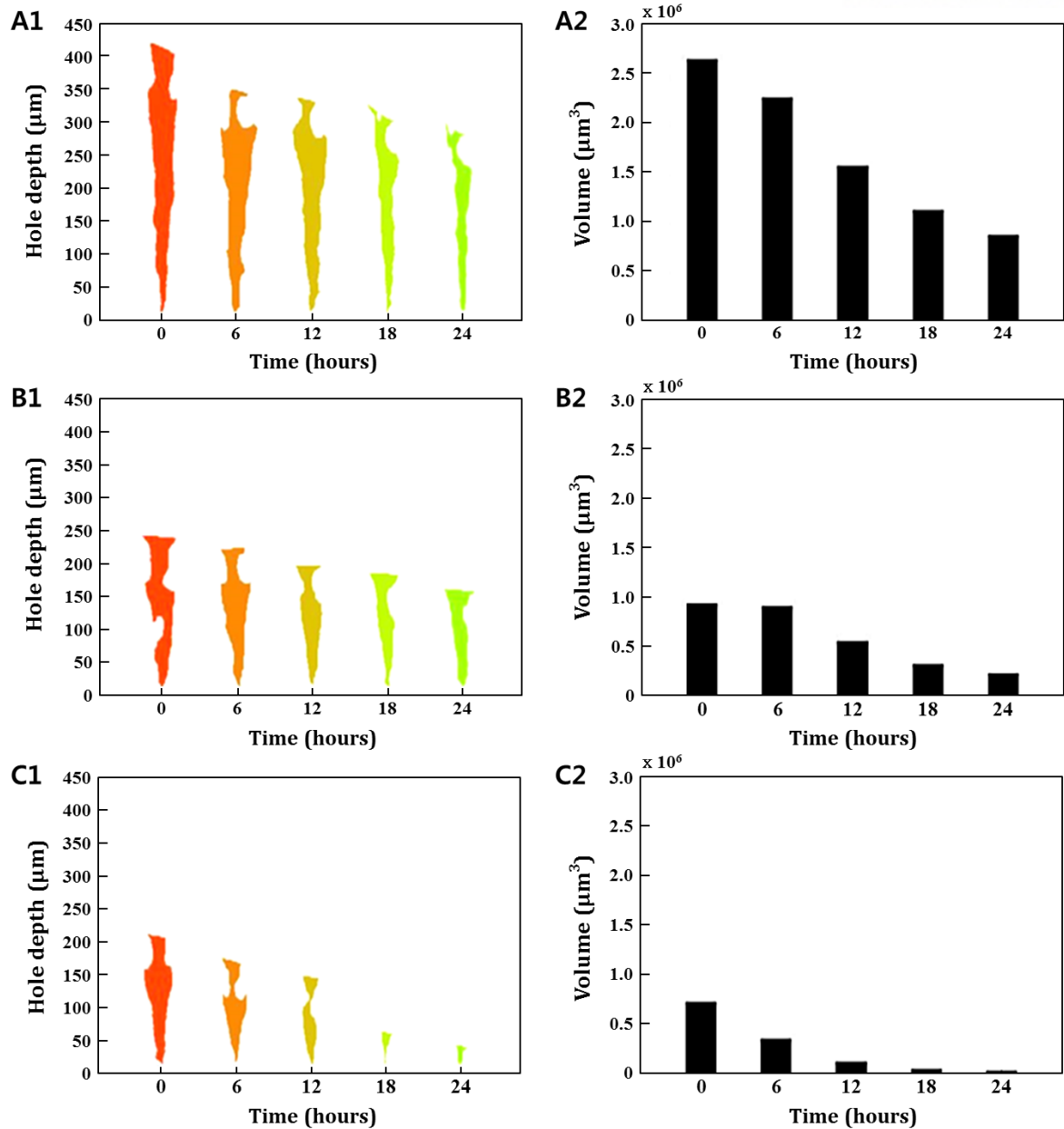
Figure 2-8. Comparison of the relationship between different laser powers and wound depth with volume. (A1) The hole depth after irradiation is about 420 μm in 120 mJ/cm² laser power, (B1) 240 μm in 80 mJ/cm² laser power, and (C1) 220 μm in 40 mJ/cm² laser power. (A2) The volume after irradiation is about 2.6 million μm³ in 120 mJ/cm² laser power, (B2) 0.9 million μm³ in 80 mJ/cm² laser power, and (C2) 0.7 million μm³ in 40 mJ/cm² laser power.

Wound healing: Correlation between epidermis thickness and exposure energy

In the previous experiment, we found that tissue recovery was varied by light exposure energy [14]. We also found that the wound healing process differed by skin thickness as well. Most current protocols of laser treatment in the clinic, laser exposure parameters are adjusted with less consideration about the skin thickness and structure. It is because of a lack of tissue monitoring tools. To approach a more accurate and realistic experiment, we considered experiment variations in both laser exposure energy and tissue structure. In this study, three kinds of engineered skins were fabricated which have a different epidermal thickness, 50, 70, and 100 μm. Each skin was equally irradiated at 40, 80, and 120 mJ/cm^2, and its recovery process was then monitored by OCT.

Figure 2-9 presents the recovered volume (first column) and normalized recovery ratio (second column) to verify the relation between two experimental variations. To derive the recovery volume, the irradiated zone in the engineered skin was imaged by OCT, segmented and calculated its increment every 6 hours for 24 hours. The increment by time was plotted in the first column of Figure 2-9. The recovery ratio was derived from the comparison between the initial volume and recovered volume of the laser irradiated zone as each time point. Our results clearly explain that different skin structure is closely related to tissue recovery. The recovered volume of the irradiated zone at 50 μm epidermis skin was larger than other skins with thicker epidermal layers. As we described in Figure 2-7, this is because the thickness of the epidermis is very sensitive to light-tissue interaction and has effects on the penetration of light energy. Therefore, thin epidermis skin had a larger irradiated area with a deeper dermis region and the recovered volume was relatively larger. This tendency is more obvious when exposed light energy is increased. On the other hand, the overall recovery ratio has less deviation by skin structure. In particular, the recovery ratio is very similar regardless of epidermal thickness when time goes by.

Through this experiment, we found that both the structure of the skin and the variable of laser exposure have a strong influence on the volume of irradiated as well as recovered zone. However, the influence of the recovery ratio is more sensitive to the laser exposure power.
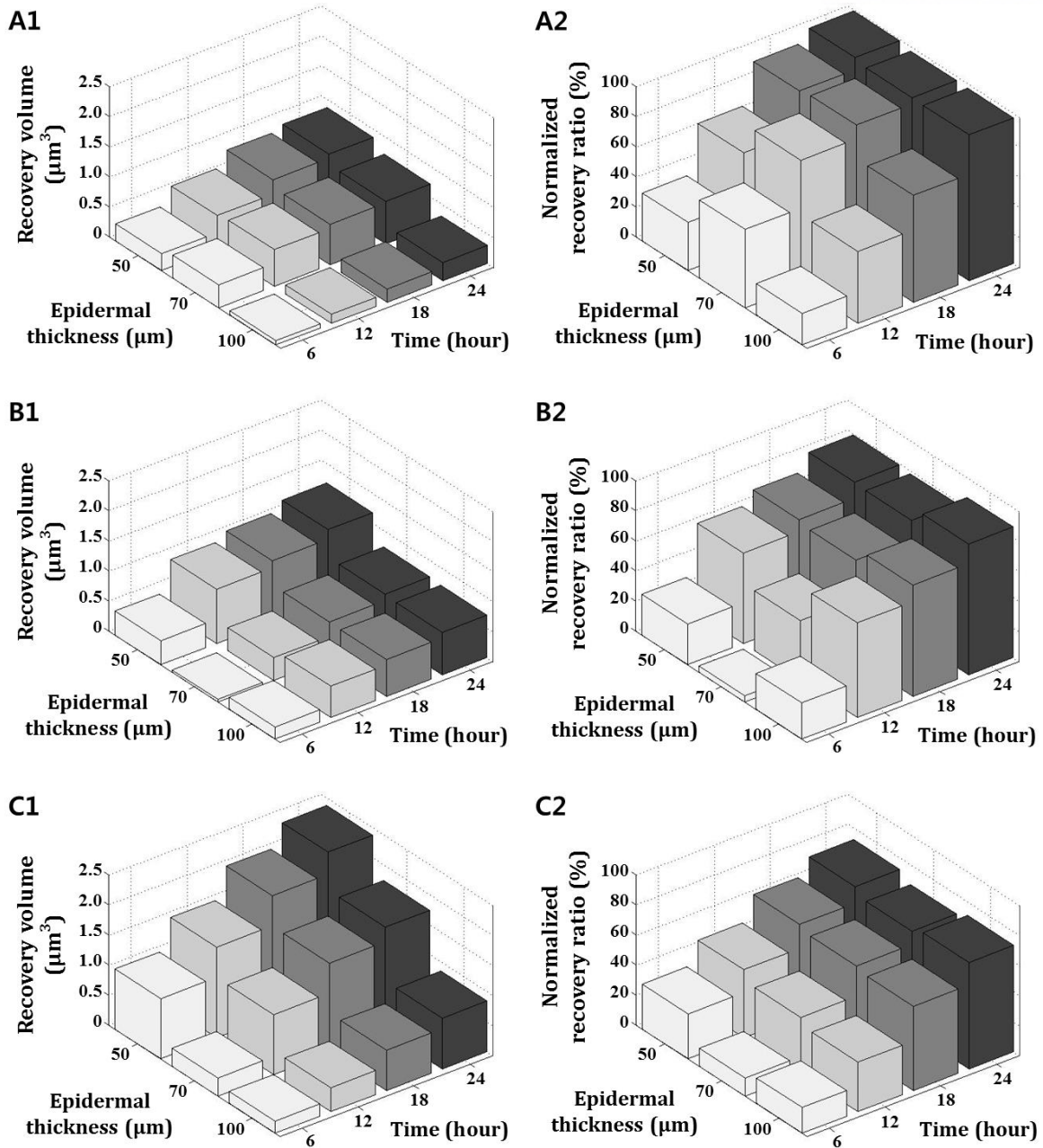
Figure 2-9. Comparison of the change of recovery volume and normalized recovery ratio according to a variation of laser exposure power and epidermal thickness. The recovery volume indicates the difference between initial and the volumes which were measured every 6 hours. Similarly, the normalized recovery ratio was measured every 6 hours and indicates the extent of the wound that was recovered from the initial wound. (A1) The recovery volume and (A2) the recovery ratio of after 40 mJ/cm^2 laser exposure, (B1) and (B2) after 80 mJ/cm^2 laser exposure, (C1) and (C2) after 120 mJ/cm^2 laser exposure.

Discussions and conclusions

OCT is a proper imaging modality to monitor the wound healing process, because it provides morphological change of tissue, non-invasively and dynamically [14]. As OCT technology is advanced, it is also possible to observe volumetric and quantitative healing process of wound region. Even though OCT has strong potential to be utilized to wound healing study, only few researches have been reported for laser wound monitoring as shown in Table 1.

Table 2-1. Comparison of laser wound healing study-based OCT monitoring

	Laser Type (Wavelength)	Laser Dosage	Irradiated Area	Subject	Recovery Time	Monitoring Tool
Our Study	Ablative Fractional Laser (CO_2) (10,600 nm)	40, 80, and 120 mJ/cm^2	~ 100 μm diameter	Engineered Skin	Around 1~2 days	OCT
W. Jung, et al. [20]	Nd:YAP Laser (1,341 nm)	25 and 35 J/cm^2	~ 1.5 mm diameter	Engineered Skin	~ 7 days	OCT
A. T. Yeh, et al. [21]	Nd:YAP Laser (1,341 nm)	20 J/cm^2	~ 1.5 mm diameter	Engineered Skin	~ 7 days	OCT Multi-photon Microscopy (MPM)
M. T. Tsai, et al. [28]	Non-Ablative Fractional Laser (Erbium doped) (1,550 nm)	15, 20, and 25 mJ	~ 200 μm diameter at NAFL	Human Skin (Belly and Face)	6 days at NAFL	OCT
	Ablative Fractional Laser (CO_2) (10,600 nm)		~ 150 μm diameter at AFL		14 days at AFL	
E. C. E. Sattler, et al. [29]	Ablative Fractional Laser (CO_2) (10,600 nm)	8 and 16 W	~ 400 μm diameter	Human Skin	7 ~ 14 days	OCT Confocal Laser Scanning Microscopy (CLSM)
C. A. Banzhaf, et al. [30]	Ablative Fractional Laser (CO_2) (10,600 nm)	5, 15, and 25 mJ	~ 100 μm diameter	Human Skin (Forearm)	2 ~ 7 days	OCT Reflectance Confocal Microscopy (RCM)

One of interest in tissue regeneration study is to investigate the recovery time of wound region. As previous works present, the tissue recovery is varied by the targeted tissues as well as the laser irradiation parameters such as laser dosage, duration, and exposed area. Our previous and current works utilized the engineered skin, but it showed different recovery time [20, 21]. As aforementioned, the laser treated region in this study was mostly recovered within 1~2 days which was faster than one in our previous studies, 7 days. It is because that laser energy exposed in previous work, 20~35 J/cm^2 was much higher than what we used in this study, 40, 80, and 120 mJ/cm^2. Entire area of laser irradiated region is also crucial component to make the different recovery time. Thus, the shorter recovery time presented in this study is reasonable. On the other hand, M. T. Tsai, et al. and C. A. Banzhaf, et al. used human skin rather than engineered skin. Even though they hired similar laser irradiation condition to our study, the wound healing time shows the big disparity [28, 30]. It indicates the engineered skin is structurally analogous to human skin, but it has still restriction to fully mimic the human skin. In general, most engineered skins have simple skin structure which is composed of essential elements such as fibroblast, keratinocyte, and collagen. Whereas human skin contains

additional extracellular matrix and other cells which forms tight junctions between biological components [31]. In human skin, wound healing process involves systemic and complex events including hemostasis, cell migration, matrix deposition and tissue remodeling [32]. However, the tissue regeneration in engineered skin having basic structure and loose biological junction is mainly governed by simplified process, cell proliferation and remodeling. Therefore, faster laser wound recovery in this study can be explain by structural and functional difference as well as different healing events between engineered skin and human skin. When the engineered skin is mature and closer to human skin, it is believed that wound healing study combined with engineered skin and OCT quantification could be emerging research platform with high reliability.

In conclusion, we have demonstrated quantitative OCT in a laser wound recovery study. Experimental results showed that the wound healing process is active in the vertical direction, and recovery time varies by the tissue structure as well as the irradiation condition. We also confirm that OCT is the most promising tool for monitoring the wound healing process, when it is integrated with other contrast, such as stiffness and polarization.

2.2.3 Monitoring of Epidermal Regeneration in Wound Engineered Skin

Research Motivation

Recently, many alternative methods have been studied for the replacement of animal experiments [33, 34]. Engineered skin model as one of the most representative alternatives is a three-dimensional skin equivalent reconstructed by epidermal and dermal cells with scaffolds [35, 36]. The engineered skin is widely used to evaluate the substance efficacy because it is easy for observing skin response to external stimulation. The existing methods for efficacy evaluation using engineered skin were to observe the skin surface with a camera or the naked eye or used tissue sectioning and staining method. In this case, however, it is difficult to monitor and analyze significant morphological changes quantitatively in the tissue.

In this study, we utilized the engineered skin to monitor and analyze quantitively the wound regeneration process after epidermal biopsy with several substances that are well known for accelerating wound regeneration. We monitored continuously and analyze quantitatively the wound regeneration process on the engineered skin using optical coherence tomography (OCT). As mentioned earlier, OCT is good for monitoring of morphological changes over time with visualization of high-quality 3D tissue information. We selected several materials that affect skin regeneration and we analyzed quantitatively how these substances worked in the skin regeneration process on the epidermal biopsied engineered skin model.

Monitoring of epidermal regeneration for drug efficacy assessment

Madecassoside extracted from *Centella Asiatica* is known to have effective potential in the treatment of skin diseases such as wounds and psoriasis. Several studies have verified that the madecassoside has a significant effect on promoting cell growth, accelerating wound and scar regeneration [37, 38]. Also, it has the potential to help improve various symptoms by its functions as antioxidant, antiulcer, sedative, and anti-inflammatory properties. In recent, in the cosmetic fields, the madecassoside has been used as a functional substance that promotes cell activity and helps skin recovery.
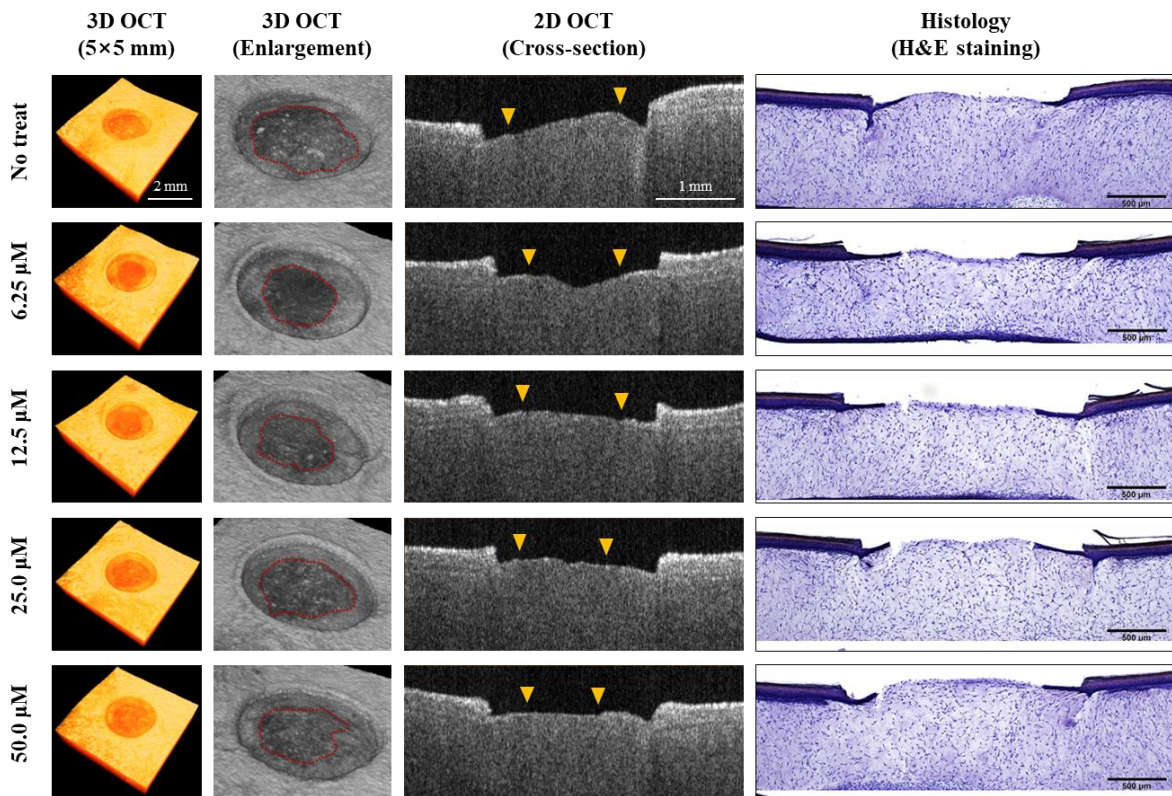
Figure 2-10. Skin regeneration on engineered skin by madecassoside concentration. The epidermal layer of engineered skin model was removed by 2 mm diameter biopsy and the skin models were exposed to different concentrations of madecassoside for 2 days. Cross-sectional 2D OCT image demonstrates similar aspects of H&E staining image. In 2D OCT image, epidermal regeneration confirmed by keratinocyte differentiation over the exposed dermis regions. Also, we confirmed regeneration area which provides a quantitative degree of epidermal regeneration in 3D OCT image.

Here, we utilized OCT modality to observe and analyze quantitatively the wound regeneration on engineered skin which was treated with different concentrations of the madecassoside. After the epidermal biopsy (2.0 mm, Miltex® biopsy punch) on engineered skin, we monitored how the different concentration of the madecassoside affects the migration of keratinocyte in the epidermal layer. Each engineered skin was treated by madecassoside solution with different concentration about

6.25, 12.5, 25.0, and 50.0 µM for 2 days. After the treatment, for the morphological analysis with correlation study, we acquired 2D and 3D OCT images of all skin samples and the samples were embedded into the paraffin for hematoxylin and eosin (H&E) staining. The histological analysis such as H&E staining is mainly used to observe the recovery of epidermal layers by differentiation of the keratinocyte under the two-dimensional image of optical microscopy.

In Figure 2-10, we confirmed the high correlations between the cross-sectional 2D OCT image and histology image. In the 2D OCT image, the epidermal layer has a high-intensity signal because the keratinocyte which is a major constituent of the epidermis has strong reflections on the near-infrared light. Therefore, we distinguished clearly between the recovered and the unrecovered regions in the cross-sectional OCT image, as with the results of the tissue staining. As shown in the histology image of Figure 2-10, the degree of epidermal regeneration was evaluated by measuring the length of the newly differentiated keratinocyte layer from the epidermis over the exposed dermis on the wound area. However, this method measuring the transverse length of the new epidermal layer has an inaccurate result, because the wound is not recovered uniformly and simultaneously in all directions. This problem occurs because histological analysis by tissue staining shows only part of the wound with two-dimensional information under the microscope. In the 3D OCT images of Figure 2-10, we confirmed that the degree of the recovered epidermis was different in every radial direction based on the center of the wound. For this reason, we demonstrated that the existing quantification method for epidermal regeneration by measuring the transverse length of the new epidermis has an error or inaccurate values on the tissue stained image.
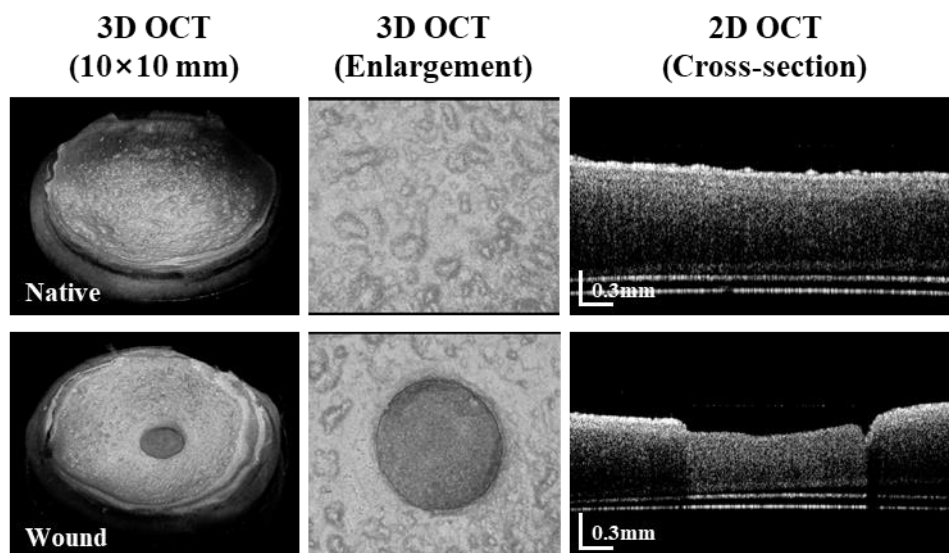
Figure 2-11. Three-dimensional reconstructed and cross-sectional images of skin wound model on engineered skin before and after epidermal biopsy. The only epidermal layers of skin wound model was removed and it monitored after drug treatment at the different time positions.

(A) No treat
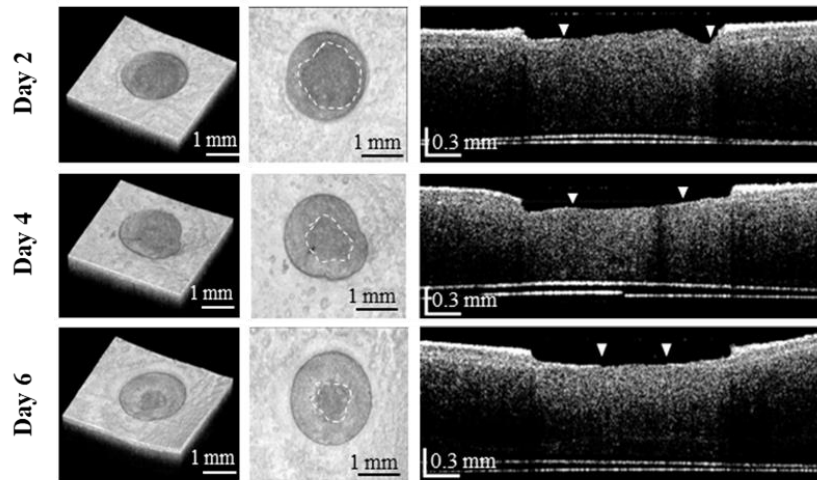
(B) 1.0 mg/ml
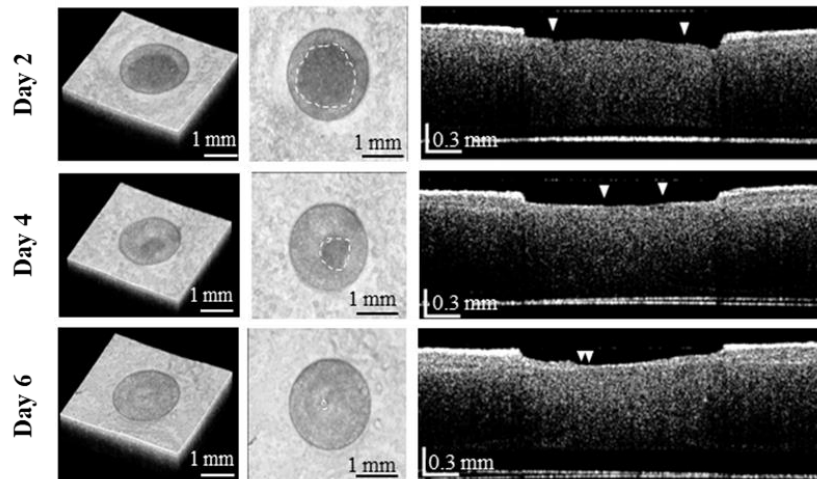
(C) 10.0 mg/ml
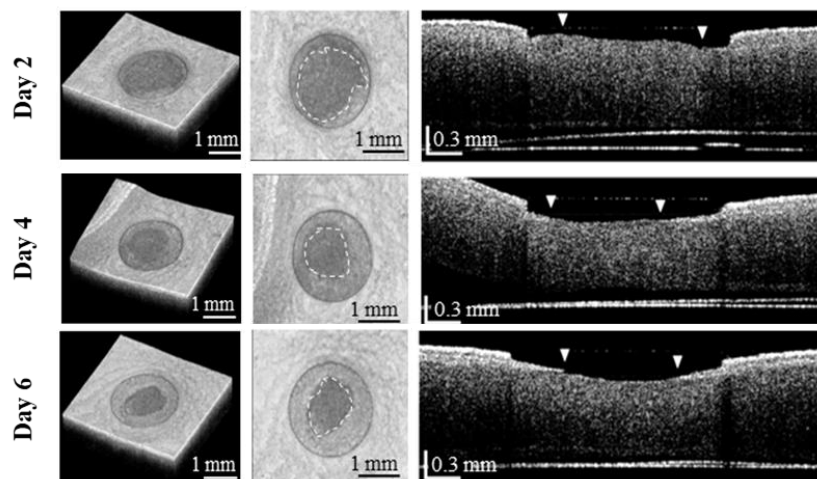
Figure 2-12. Effects of chondroitin sulfate on wound regeneration process using engineered skin model and OCT imaging. (A) Serial wound regeneration process monitoring on 2, 4, and 6 days with no treatment, (B) and (C) with different concentration of chondroitin sulfate treatment.

We also analyzed and evaluated the effect of chondroitin sulfate to wound regeneration on the epidermal biopsied engineered skin model. Chondroitin sulfate is a type of glycosaminoglycan and it functions as a major component of the extracellular matrix. Chondroitin sulfate affects the wound regeneration process which includes accelerating of fibroblast migration and proliferation as well as keratinocyte proliferation [39, 40].

Here, we monitored wound regeneration with the treatment of chondroitin sulfate continuously under the low and high concentrations of chondroitin sulfate solution every 2, 4, and 6 days. OCT provides morphological information non-invasively without any damage to the sample. It is an important advantage for the continuous monitoring of morphological changes by different external factors in the sample skin model. Figure 2-11 represents 2D and 3D OCT images before and after wound formation by epidermal biopsy. The epidermis layer of the wound region was removed clearly, and only the dermis was exposed. In Figure 2-12(A), we monitored the wound recovery process of the control group which is untreated by chondroitin sulfate. Also, Figure 2-12(B) and (C) shows the wound recovery process of the chondroitin sulfate treated wound skin model. For the wound model exposed to 10 mg/ml concentration of chondroitin sulfate over 6 days, we could not identify significant results about the positive influence on wound regeneration compared to the control group. However, for a case of 1 mg/ml concentration, we confirmed the significant wound regeneration on the wound region. In the 3D OCT image, the epidermis layer consisted of keratinocyte has a higher intensity signal than a dermis region where was not yet covered with the epidermis layer. Therefore, we confirmed that most of the exposed dermis regions were covered with a new epidermal layer by keratinocyte differentiation and migration on day 2. On the sixth day, all the wound regions were covered with the epidermal area.

Wound segmentation for quantitative analysis
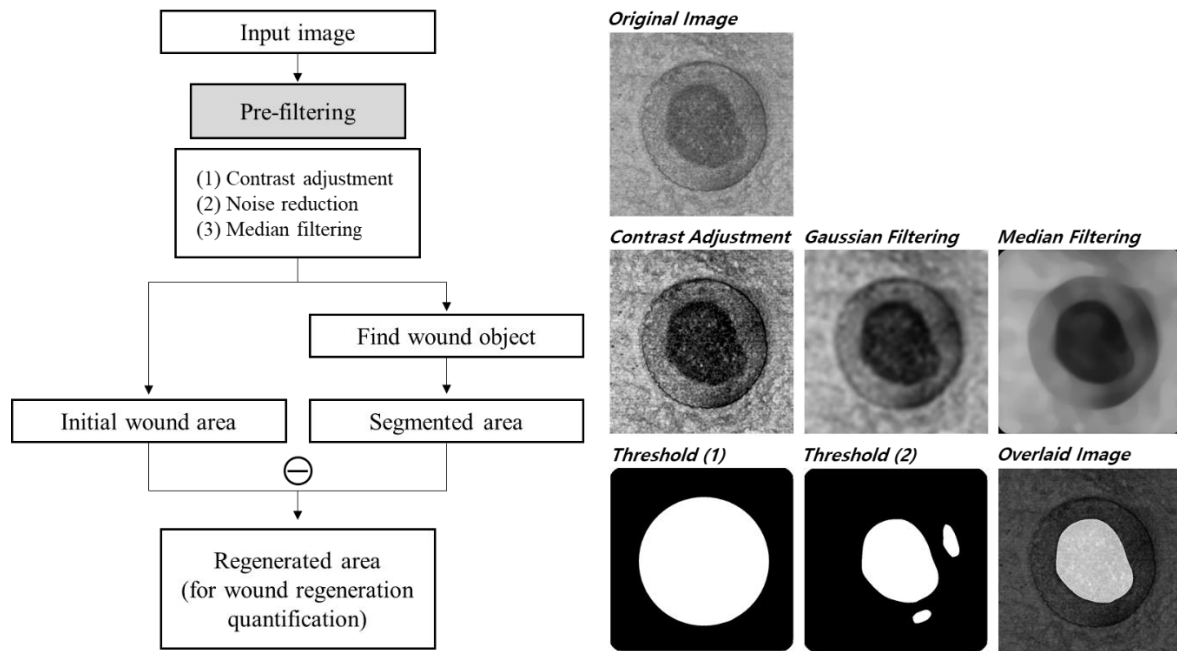
Figure 2-13. The segmentation algorithm of initial wound region and regenerated region by keratinocyte differentiation and migration for quantitative analysis of wound regeneration after epidermal biopsy.

We made a MATLAB based segmentation algorithm to quantify the extent of epidermal regeneration as shown in Figure 2-13. In 3D OCT images of engineered skin, there is a clear contrast difference between the non-invasive epidermal region and the biopsied wound region. Also, even in the biopsied wound region, there is a difference in contrast between the regenerated region progressed by keratinocyte differentiation and wound region that remains unrecovered. We tried the pre-filtering process to reduce the image noise for accurate image processing and image contrast was adjusted to set the correct threshold values. After then, we found the boundary where the contrast value changed dramatically based on the center of an image. The first dramatic change point determined as the boundary between the regenerated region by keratinocyte and unrecovered dermis region, and the second point determined to be a boundary of an initial wound by epidermal biopsy. We segmented the remained wound area where it was not recovered yet based on the boundary we found first. Similarly, the initial wound area was segmented based on the second boundary, and then we analyzed the extent of wound regeneration quantitatively using these two areas.

(A1)

(A2)

(B)
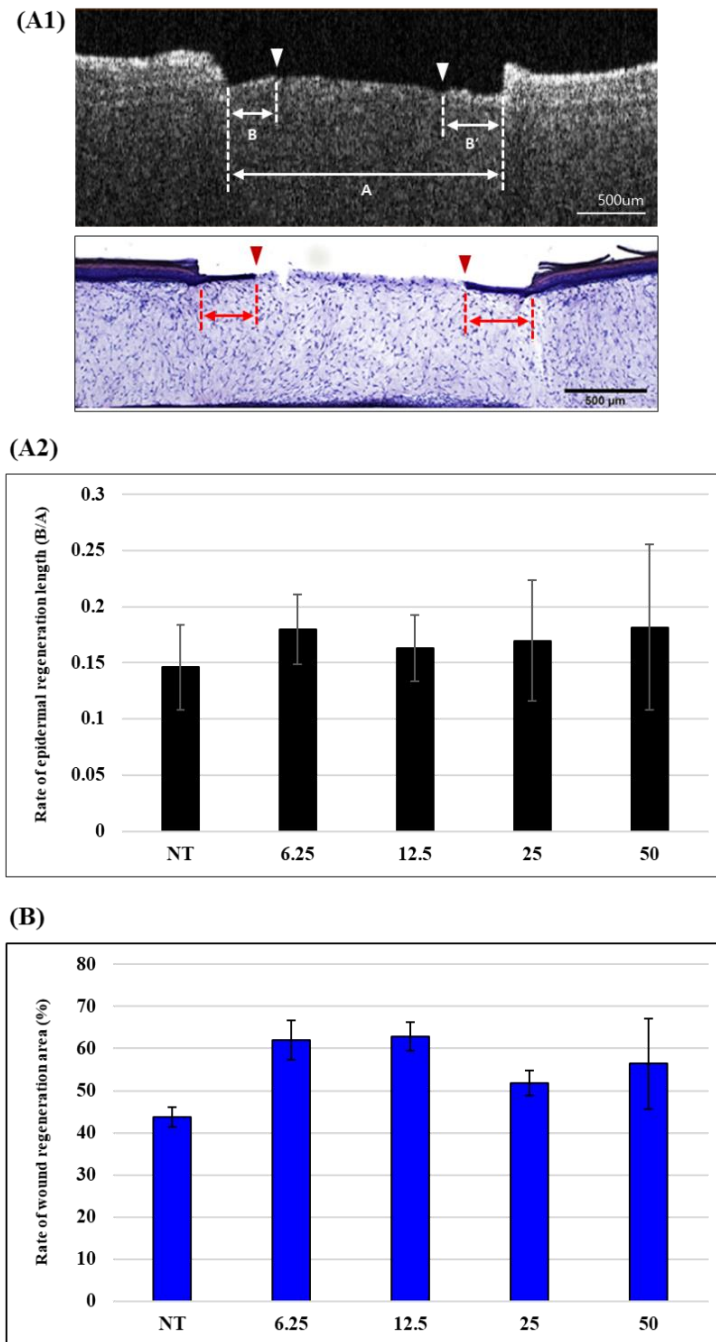
Figure 2-14. Comparison of quantitative analysis method between transverse length measurement in 2D image of histology and wound area measurement in 3D OCT image about the effectiveness of madecassoside in wound regeneration. (A1) Existing quantification method to evaluate wound regeneration by measuring newly differentiated epidermal layer, (A2) The results from (A1) show that madecassoside has slight effectiveness in epidermal regeneration under all concentration conditions. The value is calculated by dividing the length of the recovered part 'B' by the length of the entire wound 'A', (B2) The results show a quantitative analysis of regenerated wound area in biopsied engineered skin using the segmentation algorithm based on 3D OCT images.

Figure 2-14 presents the quantitative analysis of wound regeneration on the epidermal biopsied engineered skin depending on the concentration of the madecassoside. In Figure 2-14(A1), we acquired a cross-sectional OCT image and histological image of the same region at the center of the wound after the epidermal biopsy. We confirmed that a new epidermal layer was formed by keratinocyte differentiation and migration over the exposed dermis region from the boundary of the initial wound. The evaluation of the wound recovery in epidermal biopsied engineered skin was calculated by measuring the transverse length of the newly formed epidermal layer in the histology images. In Figure 2-14(A2), the rate of epidermal regeneration was calculated by dividing the transverse length of the newly formed epidermis layer, 'A' by the transverse length of the entire wound, 'B'. As mentioned earlier, however, the method of length measurement was not accurate to measure the epidermal regeneration which was occurred in all directions simultaneously. We analyzed quantitatively the area of the newly formed epidermal layer by keratinocyte differentiation on the top-view of the 3D OCT image. The results using the area segmentation algorithm in Figure 2-14(B) suggested accurate quantitative values about the extent of the regenerated area in comparison with the transverse length measurement in 2D images. In Figure 2-14(A2), the madecassoside treated wound skin models had less significant results for the epidermal wound regeneration, also it has a huge deviation within the same conditions. However, the results of the epidermal regeneration analysis based on the area segmentation in Figure 2-14(B) present that the madecassoside has significant effects on the wound regeneration compared to the control groups. Also, the results from the area segmentation of 3D OCT image has a less deviation than the length measurement method. It means that area measurement has accurate values in terms of uniformity and reproducibility.
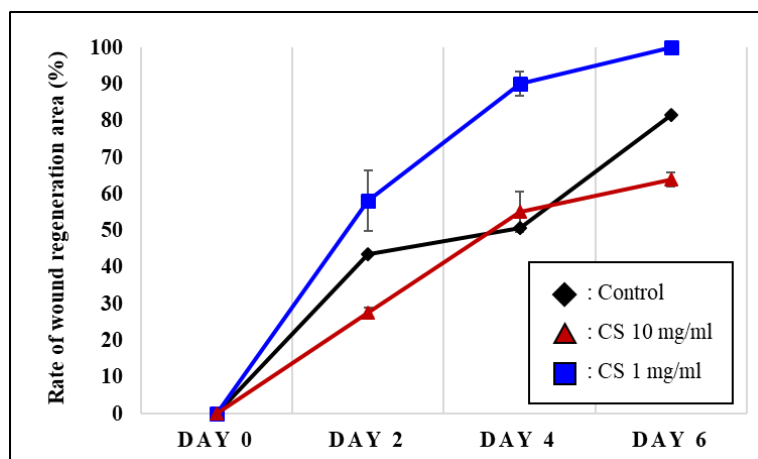
Figure 2-15. Quantitative analysis for the effectiveness of chondroitin sulfate in wound regeneration by concentration and time. The high concentration (10 mg/ml) chondroitin sulfate has not a significant effect on wound regeneration in comparison with control group. However, the low concentration (1 mg/ml) chondroitin sulfate has a positive effect to wound regeneration. The biopsied wound of 2 mm diameter recovered in 6 days in low concentration of chondroitin sulfate.

In Figure 2-15, we analyzed quantitatively the epidermal biopsied wounds recovered over time at different chondroitin sulfate concentrations using the area segmentation of 3D OCT images as shown in Figure 2-12. As a result, in the high concentration of chondroitin sulfate solution (10 mg/ml), there were no significant effects on wound regeneration compared to the control group which was treated by the only medium. However, we confirmed that the wound regeneration was accelerated in a low concentration of chondroitin sulfate (1 mg/ml). The wound recovered steadily in low concentration conditions, and the exposed dermis was fully covered by the new epidermis layer after 6 days despite the regeneration area of about 70% in high concentration and control groups. Here, we demonstrated that even the same material or substance promotes or inhibits wound regeneration depending on the concentration.

Discussions and conclusions

In this study, we presented a quantitative evaluation of drug efficiency that affect the wound recovery on the engineered skin model after epidermal biopsy using the OCT imaging modality. In recent, there are many researches has been introduced to evaluate responses to different drugs and stimuli in the engineered skin for a replacement of animal experiments. The histological staining which has been most commonly used for morphological evaluation has a complex procedure and it is hard to monitor morphological changes in the same sample due to invasive manner. Also, because histology is observed with two-dimensional images under the microscope, it is difficult to analyze three-dimensional changes in the tissue. Therefore, we suggested that OCT can be utilized to evaluate the efficacy of material treatments on the engineered skin using its advantages of non-invasive and real-time monitoring.

Here, we evaluated the wound regeneration according to the concentration of madecassoside and chondroitin sulfate in epidermal biopsied engineered skin. We created the segmentation algorithm based on MATLAB to quantify the newly regenerated epidermis area and suggested quantitative values that are more accurate than conventional methods. As a result, the significant outcome has been derived that madecassoside and chondroitin sulfate have positive effects on wound regeneration. It was also confirmed that the same substance may interfere with the recovery of the wound depending on the concentration. In conclusion, efficacy assessment and evaluation in engineered skin using OCT modality can provide the optimum conditions such as concentration and treated time for most effective wound regeneration.

2.2.4 Quantification of Wound Regeneration in Rodents Wound Model

Tissue adhesive

In the medical field, a suture has mainly used to inosculate the biological tissues as the most basic method. However, there is a possibility that the suture is loosened, and it can cause an inflammatory reaction due to unexpected cut as a foreign substance. For this reason, many tissue adhesives have been developed to bond incised tissues and help regeneration without the traditional suture. The tissue adhesive has to satisfy following conditions; (1) non-toxic and non-fatal toxicity, (2) sterilizable, (3) applicable in water-soluble environments, (4) sufficient mechanical properties, (5) biodegradability, (6) reasonable cost, etc. [41].

Wound healing monitoring in skin incised rat model

In this study, we analyzed quantitatively the effects of tissue adhesive on the wound recovery of skin incised rat model using chitosan-based tissue adhesive and OCT imaging system [15]. We monitored how the chitosan-based tissue adhesive affected wound regeneration compared with fibrin which is one of the conventional tissue adhesives and a suture used for stitching up the wound as a control group. The chitosan-based tissue adhesive was fabricated to help inhibit infection in the early stage of the wound with antibacterial properties while the wound was enclosed tightly by strong adhesion of tissue adhesive. The most important advantage of chitosan-based tissue adhesive is that it can be treated to any wound region quickly with the desired form based on *in situ* fabrication. Also, it was designed to fall off naturally a day later for the reduction of side effects during the wound regeneration process.
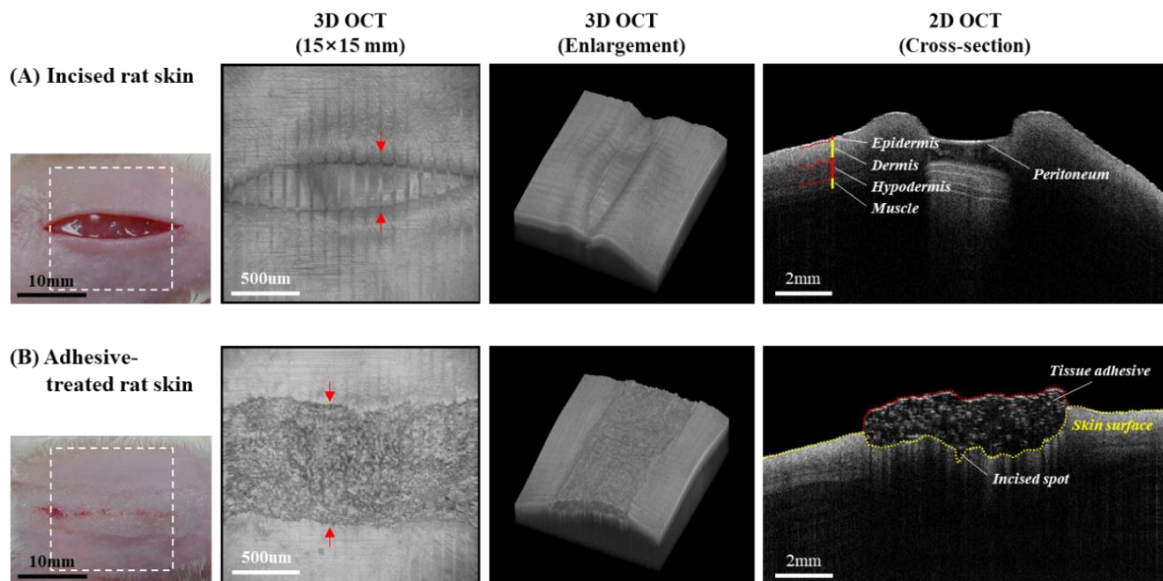
Figure 2-16. Cross-sectional (2D) and 3D OCT image before and after a treatment of the chitosan-based tissue adhesive. (A) 2D and 3D OCT image after the skin incision with 20mm by surgical knife, (B) OCT image after a treatment of the tissue adhesive.

Figure 2-16 presents a photo and OCT images before and after the treatment of the chitosan-based tissue adhesive in the skin incised rat model. All animal procedures were performed with the approval from Institutional Animal Care and Use Committee (#UNISTIACUC-18-22) of Ulsan National Institute of Science and Technology (UNIST). We designed the skin incised rat model, which produced a 2 cm-long incision by sterilized surgical knife with a 5 cm × 5 cm area on the dorsal region of the SD rat (three weeks, male) under the anesthesia ventilator. Figure 2-16 shows a 2D and 3D OCT images of the wound after the skin incision. We identified the morphological structure of the skin wound in the cross-sectional 2D OCT image and the overall structure of the wound in the 3D OCT image. In Figure 2-16(B), we acquired the OCT image of the wound in the skin incised rat model after the treatment of the chitosan-based tissue adhesive. We confirmed that the tissue adhesive was well-sealed to protect the wound.
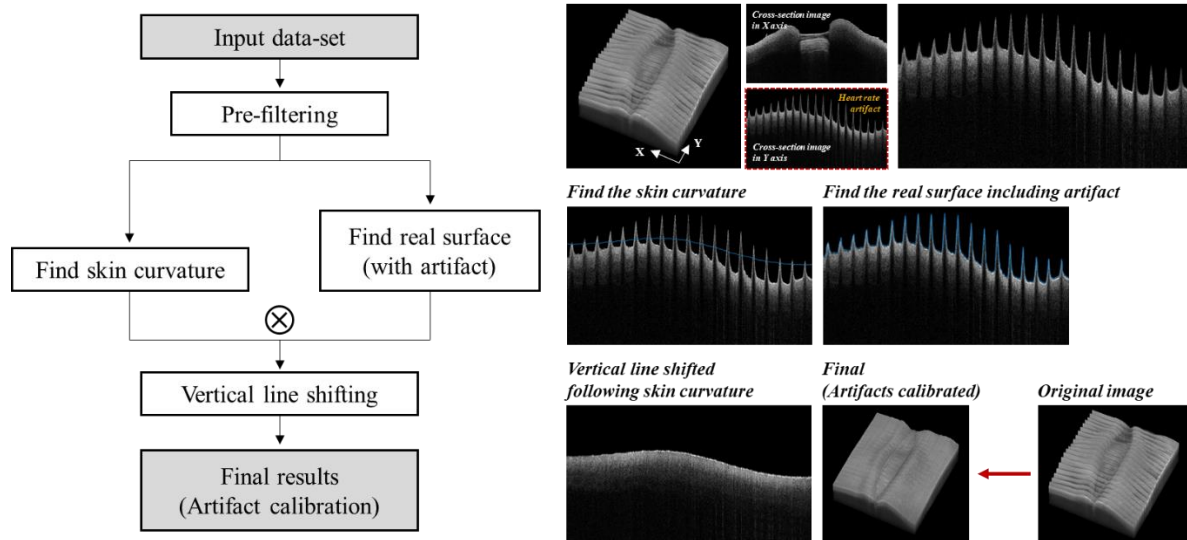
Figure 2-17. The image reconstruction algorithm for artifact calibration from a heartbeat in a cross-sectional OCT image. The trend line of skin curvature and surface line including the artifact were found and these lines used to be applied in a vertical line shifting for compensation of heartbeat artifacts that occurred during OCT image acquisition.

Here, we conducted a quantitative analysis of wound regeneration treated by the chitosan-based tissue adhesive in the rat wound model in vivo using OCT imaging. Therefore, the artifacts caused by a heartbeat in alive SD rats occurred during a continuous acquisition of a cross-sectional 2D OCT image for the volumetric reconstruction of 3D OCT images. As shown in Figure 2-17, the artifact of the heartbeat appeared in periodic patterns on the 3D OCT image. To compensate for the artifacts, we reconstructed OCT images acquired along the X direction to cross-sectional OCT images in the Y direction. The heartbeat artifact was observed in detail in the reconstructed cross-sectional 2D OCT image in the Y direction. First, we tried image de-noising to extract a clear surface line that was shifted

vertically due to the heartbeat. We extracted a surface line containing artifacts (blue line in the step of 'Find the real surface including artifact' in Figure 2-17) by detecting the point of dramatic intensity change along the vertical direction. Next, we applied a median filter to the same artifact included image as before to find the curvature of actual skin surface, and we extracted the trend line of a skin curvature (blue line in the step of 'Find the skin curvature' in Figure 2-17). Finally, the coordinate difference between the trend line of skin curvature and the artifact included surface line was calculated and it applied to correct the cross-sectional OCT image including artifact by a vertical shifting. As a result, we acquired a clean 2D and 3D OCT image of wound area in skin incised rat model without heartbeat artifacts.
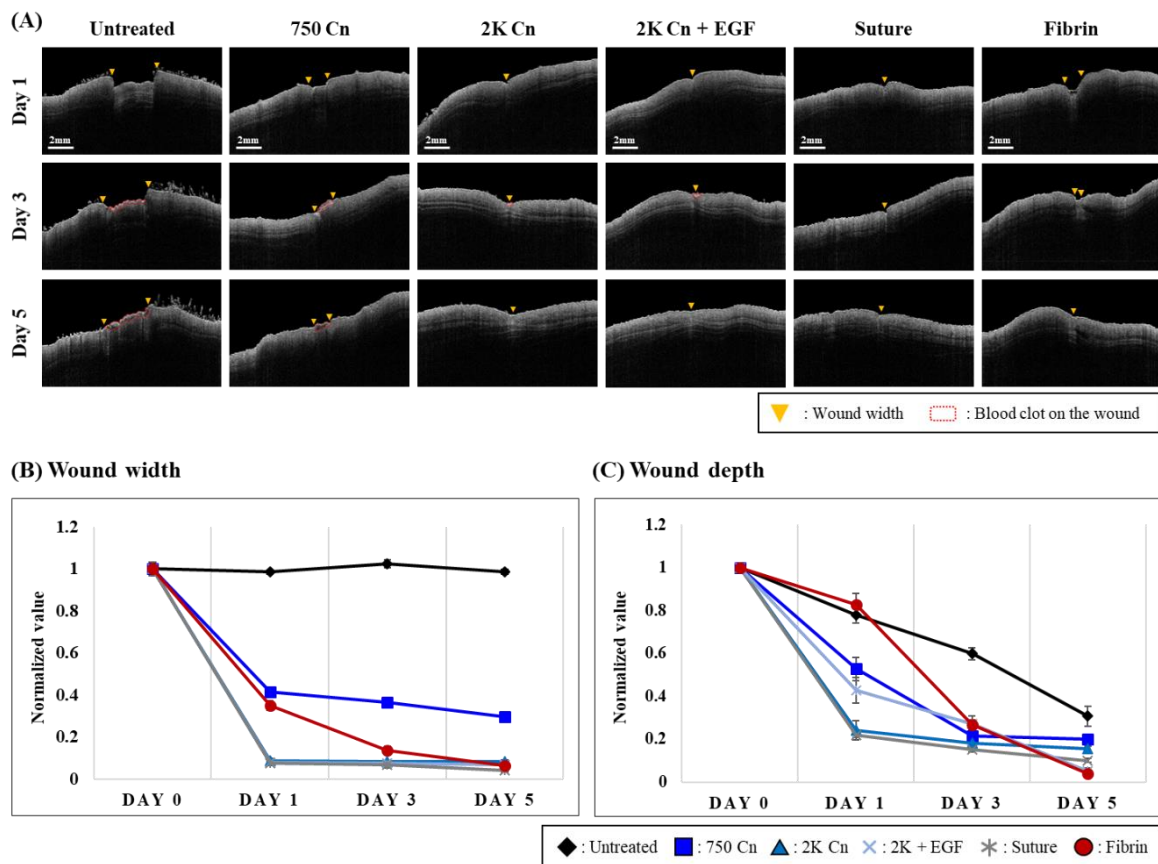
Figure 2-18. Quantitative analysis of the wound regeneration in a skin incised rat wound model after the treatment of a chitosan-based tissue adhesive using the OCT monitoring. (A) Cross-sectional image of OCT monitoring results for each experimental condition every 1, 3, and 5 days after the treatment. 'Untreated' group had no treatment after the skin incision. In '750 Cn', 2K Cn', and '2K Cn + EGF' groups, the chitosan-based adhesives by *in situ* reaction were treated to the wound site using a customized syringe, (B) Analysis of the wound width after the treatment in the skin incised rat model for five days, (C) Analysis of the wound depth after treatment on the wound site for five days. We measured the wound width and depth based on the cross-sectional OCT image data-set.

We acquired OCT images every 1, 3, and 5 days for the treated group by the chitosan-based tissue adhesive of several conditions, the untreated group as a control, and conventional method groups such as a suture and fibrin adhesive. Chitosan-based tissue adhesive was treated to the wound site of the skin incision model through a customized syringe. It closed the wound in an early stage with strong adhesion and then naturally fell off a day later as it gradually dried up. The untreated group did not treat with any adhesives after the skin incision, and the suture group has performed a suture at the three points with 5 mm intervals. The fibrin, another control group, was treated to the wound site in the same way as the chitosan adhesive. A specially designed wound protector was attached around the wound site to prevent natural wound regeneration from external interferences. Also, we utilized the breathing anesthetic machine while the acquisition of OCT images.

Twenty cross-sectional images were selected within 250 μm of left and right based on the center of the wound for quantification of wound width and gap. We measured the wound width by drawing a straight line connecting both ends of the incision site in the cross-sectional 2D OCT image. Also, the wound depth was measured by drawing a perpendicular line from the line of wound width to the exposed wound site. In the case of the untreated group where tissue adhesive was not treated, a bluest and wound scab were formed as the wound was left not enclosed in the early stages. As a result, we confirmed in the untreated group that the wound width had no significant change in five days and that the wound depth was slow to recover compared to other groups. On the other hand, the chitosan-based tissue adhesive treated group was identified to have a significant positive effect on the wound regeneration by rapidly decreasing the wound width and depth. Chitosan-based tissue adhesive sealed the wound tightly for a day and it fell off, indicating that the wound encloses in the early incision stage play an important role in recovering the wound afterward. A faster injury recovery tendency was identified at the 2K Cn group, which was more viscous than 750 Cn group, indicating a similar wound recovery trend to the typical wound enclose method of suture and fibrin-based tissue adhesive.

Discussions and conclusions

The chitosan-based tissue adhesive can be applied quickly to any desired location through *in situ* reaction, also it has antibacterial properties and strong adhesion. We analyzed quantitatively a recovery process of the wound width and depth in skin incised rat model *in vivo* with tissue adhesives treatment using the OCT imaging technique. Also, we acquired improved OCT images using the compensation algorithm for a heartbeat artifact. As a result, we confirmed that the tissue adhesive treated group enclosed the wound in the early stage, and it accelerated faster wound regeneration than the untreated group. Also, we demonstrated the wound recovery tendency of the adhesive relative to suture or fibrin. In conclusion, OCT has the advantage of monitoring morphological changes in the *in vivo* studies because it provides non-invasive cross-sectional images in real-time.

CHAPTER 3. Serial Block-face Optical Coherence Microscopy for Whole Tissue Imaging

3.1 Optical Coherence Microscopy (OCM)

In this chapter, we introduce optical coherence microscopy (OCM) imaging modality to observe the changes in sub-cellular level, which is difficult to observe with OCT imaging. The OCM imaging technique is a branch of OCT technique that combines each advantage from OCT and confocal microscopy using a high numerical aperture (NA) objective lens to provide high lateral resolution up to cellular level [42]. Also, the OCM modality utilizes high NA objectives to provide higher resolution compared to that of OCT. Besides, OCM allows imaging depth up to 500 μm which is deeper than confocal microscopy. The OCM is appropriate for analyzing biological samples owing to the capability of high-quality *en-face* imaging without labeling or contrast agents, unlike the confocal microscope. It has potential in biomedical fields that offer 3D structural, functional imaging capability and visualization of anatomic as well as subcellular features without the requirement for sample pre-processing or labeling.

3.1.1 Hardware Configuration and Specification

The schematic of the optical coherence microscopy (OCM) is shown in Figure 3-1. The OCM system was constructed with a light source, sample collector, XY axis stage, and spectrometer. The broadband super-luminescent diode (SLED) having a center wavelength of 800 nm and a bandwidth of 100 nm (D-840-HP-I, Superlum, Ireland) was used to provide ~ 6.7 μm depth resolution [43]. This source was bridged with fiber optic coupler to comprise interferometer. The sample arm consisted of a silver coating galvanometer scanner and microscope objective lens for high lateral resolution. We incorporated multiple objective lenses (Olympus, UPlanSAPO) having 4X, 10X and 20X magnification with lateral resolutions of 2.7, 1.6 and 0.6 μm in air, respectively. 4X objective (NA=0.16) with a focal length of 17 mm was used for deep imaging, where lower NA enables to visualize higher signals in the depth over a large FOV. Furthermore, the 10X magnification objective lens (NA=0.40) and 20X magnification objective lens (NA=0.50) were utilized for the high-resolution imaging to provide a detailed examination of the sample. These objective lenses were mounted on the turret to rapidly interchange the magnification and FOVs as required. We used two linear motor stages (XMS100, Newport Corp., Irvine, CA) to carry out automatic imaging functionality on a position where we target in the sample. The customized spectrometer incorporated a transmission grating (1200 l/mm, Wasatch Photonics, Logan, Utah), and a 2048-pixel line scan camera (spL2048-140km, Basler,

Germany). To compensate for the signal from the nonlinearity of light in the spectrometer due to physical issues, the k-linearization method was realized in this system. The interfered signals acquired from a line scan camera were transferred from frame grabber (PCIe-1433, National Instruments Corp., Austin, TX) for post processes.
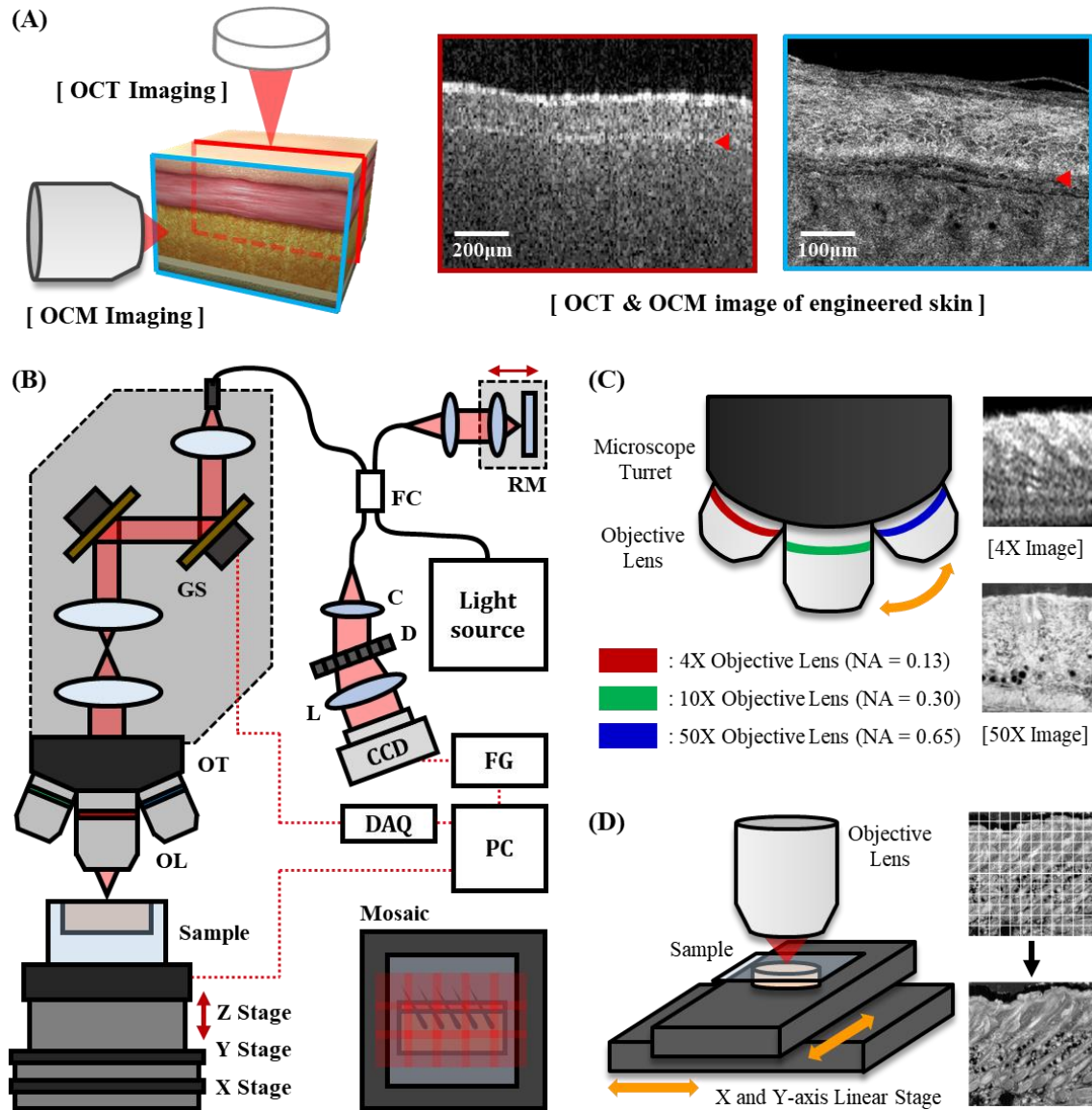
Figure 3-1. Introduction of optical coherence microscopy (OCM) system. (A) OCM provides sub-cellular resolution in lateral direction, however the penetration depth is shallow. OCM required *ex vivo* study through the sample preparation for morphological analysis inside the sample. (B) System schematics of optical coherence microscopy. GS: galvanometer scanner, OT: objective turret, OL: objective lens, FC: fiber coupler, RM: reference mirror, C: collimator, D: diffraction grating, L: Lens, FG: frame grabber. (C) Multi-scale imaging with multiple objective lens mounted on the turret to rapidly interchange the magnification, (D) Mosaic stitched imaging in large field-of-view using X and Y linear stage.

3.1.2 System Evaluation: Label-free Visualization of Hair Follicle

Research Motivation

As alopecia has become a common disease, its diagnosis and treatment have attracted attention. Alopecia is caused by a variety of factors such as hereditary, hormonal disorders, stress, and aging. These factors affect the hair cycle, disruption of follicular stem cell activity, and decrease of hair follicle regeneration, and finally results in hair loss [44]. To evaluate alopecia, there are several methods including dermoscopy, phototrichogram, microscopy, and trichogram have been introduced [45, 46]. Although these techniques have been commonly used to examine hair shafts and skin surfaces in a minimally invasive manner, its outcome is still uncertain to confirm a diagnosis of alopecia. Till now, the most reliable and routine method to diagnose alopecia is to utilize histopathological interpretation of scalp biopsy specimens [47]. Since it enables to visualize hair follicle surrounding the root of a hair, it could deliver the accurate the diagnostic information of alopecia. However, the only portion of follicular units is generally seen in a biopsy specimen, because the conventional tissue sectioning induces the sampling error to reconstruct the entire morphology of hair follicle due to its growth at an angle. Moreover, obtaining hair follicles' quantitative data in different hair cycles is more challenges considered the labor- and time-intensive procedure of histopathology while providing limited tissue information in a narrow field of view.

Recently, various optical imaging tools are introduced to enhance the cumbersome procedure in histological analysis. New optical imaging techniques equip at least one of the advanced functionalities in terms of multi-contrast, staining-free imaging, deep penetration, and quantitative analysis. Among new optical imaging methods, OCM is considerable to visualize the hair follicle structure. OCM has utilized the endogenous back-scattering signal based on the coherent gating technique of optical interferometry. Thus, it does not require chemical labeling, staining or external contrast agents. OCM has a unique feature for deep tissue imaging, because it uses near-infrared light that reaches deeper into a biological tissue than visible light. Other than the above merits, the characteristics of OCM such as real-time and 3D imaging nature are inherently well-suited for ideal histopathologic imaging. Although these previous studies presented the feasibility and potential of OCM for the histopathology, only a few studies have demonstrated a hair follicle image. In this study, we report the first wide-field OCM for analyzing multiscale and quantitative hair follicles.

Label-free Visualization of Hair Follicle using OCM imaging modality

In this study, C57BL/6 mouse (5 weeks, male) was employed as shown in Figure 3-2. Under anesthesia, transcardial perfusion was performed using phosphate-buffered saline (PBS) solution followed by 10 % neutral buffered formalin (NBF) solution to remove the blood before harvesting tissues. All animal protocols were approved by the Animal Care and Use Committee in Ulsan National

Institute of Science and Technology (UNIST). The formalin-fixed mouse tissues were embedded in the 10% of low melting point (LMP) agarose gel. Before imaging, the agarose-embedded tissue sample was trimmed by vibratome to smooth the surface for better imaging performance. Moreover, in order to avoid the dehydration, the sample should be remained in the water.
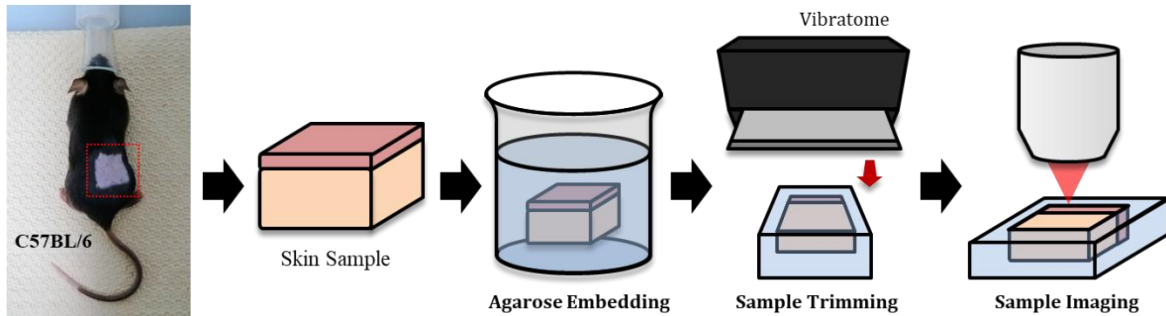
Figure 3-2. The sample preparation process for label-free visualization of a hair follicle. The skin tissue was harvested from the dorsal region of the C57BL/6 mouse under anesthesia and it embedded in agarose solution. After the agarose solidified, the embedded sample was trimmed by vibratome for the acquisition of the OCM *en-face* image.

Figure 3-3 presents a correlation between H&E (hematoxylin and eosin) stained image and OCM *en-face* image in mouse skin tissue after hair waxing. The skin tissue samples were prepared immediately after waxing for a 5 mm × 5 mm area and after growing the hair follicle for two weeks. The single OCM image has 100 μm × 100 μm area, therefore we stitched *en-face* images to acquire the image of large field-of-view using by a movement of linear stages. In the first low of Figure 3-3, we compared tissue stained image and OCM *en-face* image of skin tissue right after hair removal by waxing. Immediately after the hair removal, it was found that traces of hair follicles remained in the superficial layer of skin and we confirmed that OCM provided excellent contrast for various structures within the skin. In particular, sebaceous gland, adipose tissue, and skin muscle layers, which are difficult to clearly observe in tissue stained images, were clearly observed in OCM *en-face* images. There is a possibility to be lost the adipose tissues or fat in tissues during the dehydration process of tissue staining. Therefore, significant results have been shown by OCM images, which provide label-free imaging without any specific preparation process to the tissue. The images are shown in the second low presents the development of hair and hair follicle for two weeks after hair removal. We confirmed the hair and hair follicles that are still growing and fully matured. Also, we observed the detailed structure of hair and hair follicles in OCM *en-face* images such as hair bulb, hair root, hair papilla, and hair follicle wall consisted of the epidermal and dermal sheath.
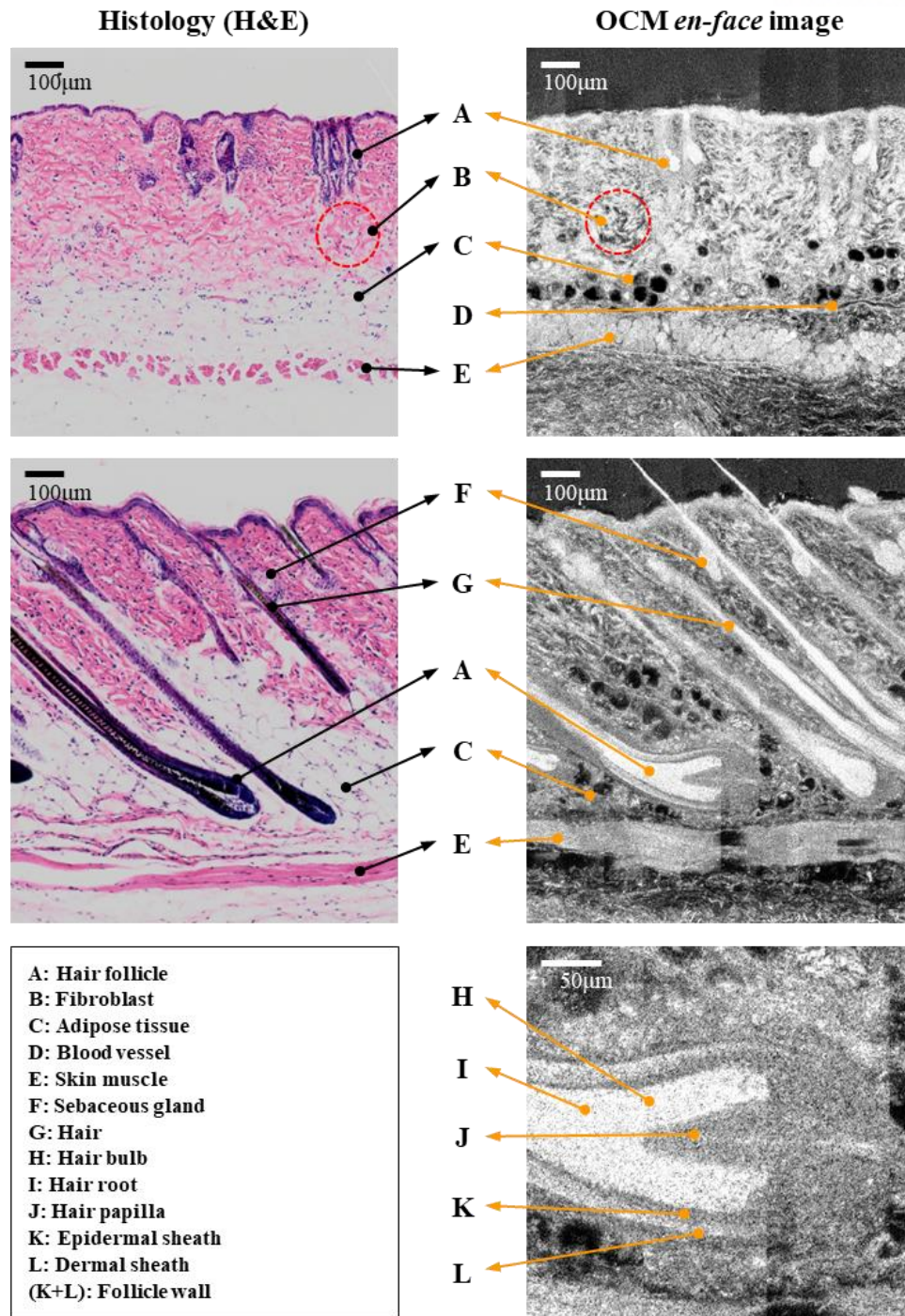
Figure 3-3. Correlation study between histological tissue staining and label-free imaging of optical coherence microscopy. OCM *en-face* images were acquired using a 40X objective lens for comparison with tissue staining images. In the OCM image, we observed detailed structures in skin tissue with high-resolution and contrast even though OCM was a label-free method without process in samples. Tissue structures of low contrast in tissue staining images such as adipose tissue and skin muscle were observed in OCM *en-face* images in detail. A: hair follicle, B: fibroblast, C: adipose tissue, D: blood vessel, E: skin muscle, F: sebaceous gland, G: hair, H: hair bulb, I: hair root, J: hair papilla, K: epidermal sheath, L: dermal sheath.
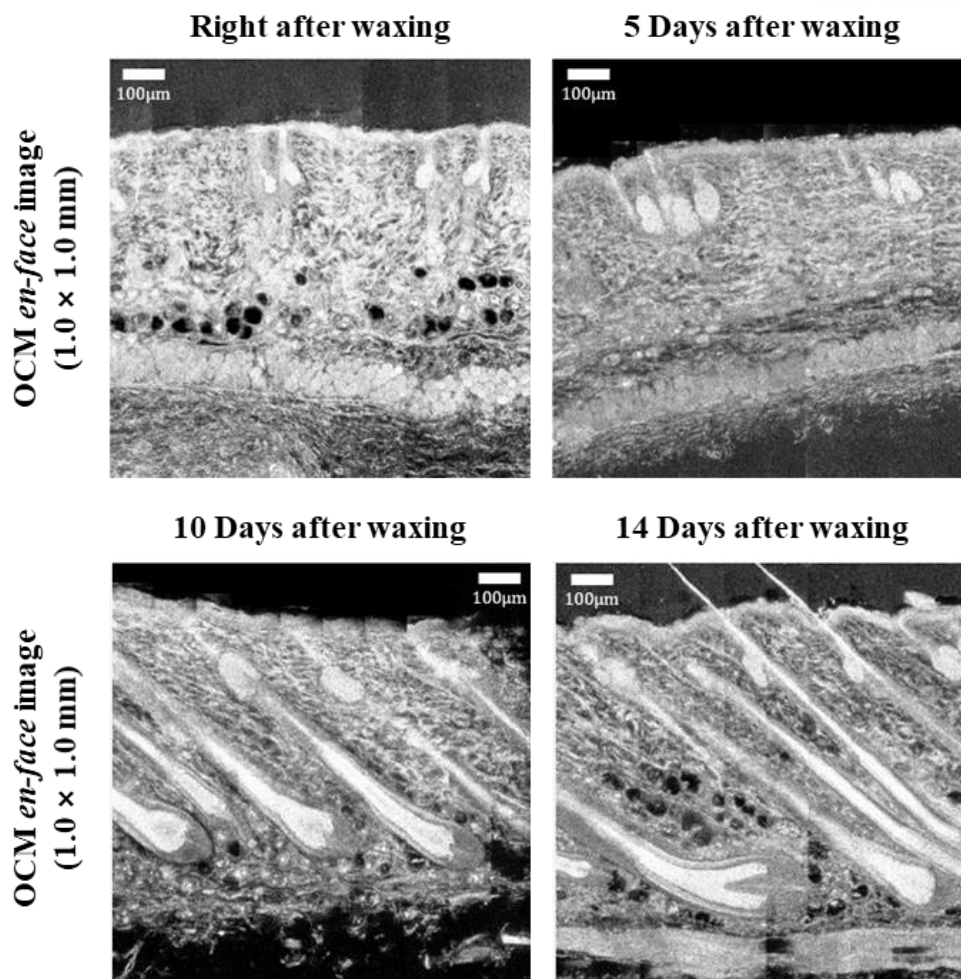
Figure 3-4. OCM *en-face* image of hair follicle development for 2 weeks after hair waxing. The growing and maturing process of hair and hair follicles was observed by the date.

In Figure 3-4, we acquired OCM *en-face* image of hair follicle development for 2 weeks after hair waxing. The growing and maturing process of hair and hair follicles were observed. The OCM image immediately after waxing showed traces of hair follicles on the superficial layer of skin. It was also clearly observed that sebaceous glands were located around the traces of the follicle. The hair follicles appeared to be gradually moving below the skin over time. The structural maturation of the hair follicles and hair was achieved, and the fully developed follicles were identified after 14 days. Here, we confirmed that OCM provided high-resolution image of morphological structures in skin tissue similar quality to tissue staining results with label-free imaging. In addition, OCM has hundreds of micrometers of presentation depth, therefore it is expected that the follicle growth process can be quantified according to volume and dimension through the three-dimensional reconstruction of the follicle structure in the future.

3.2 Depth Trajectory Tracking OCM

Optical coherence microscopy (OCM) has potential in biomedical fields that offer 3D structural, functional imaging capability and visualization of anatomic as well as subcellular features without the requirement for sample pre-processing or labeling. Nonetheless, the use of relatively high numerical aperture (NA) focusing in OCM for high transverse resolution may decrease depth-of-focus (DOF) or confocal parameter, which makes system sensitive to the angle of sample and causes dramatic signal loss at along depth away from the focus [48]. Here, we introduce a novel technique to overcome the inhomogeneous intensity of image according to DOF limitation in OCM. We employed a low NA objective and acquired a topology map of the sample through tracking the axial information while in the c-canning. The topology map was later utilized as a look-up table for the stage control in an axial direction to perform a trajectory scanning, resulting in uniform intensities across the whole area. Throughout the experiment, we have found that our innovative method is very robust, hence, applicable to any depth-resolving microscope for providing very clear and uniform images to the user.

OCM is a non-invasive imaging platform with near-infrared light, which used a high numerical NA objective lens to provide cell and tissue-level high-resolution morphological information similar to gold standard histology in tissue examination. OCM has been widely applied in the biomedical fields, because of its strong capability to provide label-free imaging of 3D tissue structure without any complicated pre-processing. Whereas OCM imaging with a high NA objective lens had limited field-of-view (FOV), thus a mosaic stitching method was required to obtain tissue information in a wide area. In particular, it was very important to retain the alignment between an image plane and a surface of a specimen, since the FOV and DOF became narrower as the NA increased. However, during image acquisition with mosaic stitching, it is difficult to determine whether the specimen was flat or tilted until the completed image was acquired. Even if the specimen had height deviation on the surface or it was tilted very slightly by a few tens or hundreds of micrometers out of the DOF, it had a sensitive and decisive influence on incorrect image acquisition such as signal loss, inhomogeneous intensity and discrete artifact between each mosaic image pieces.

Here, we introduced depth trajectory-tracking OCM to overcome and improve the problems due to DOF limitation in mosaic stitched imaging with high NA optics. We acquired a depth profile of the sample surface through the mosaic method using a 4X objective lens with relatively high DOF. After that, each time a single *en-face* image was acquired, a z-axis stage moved based on the pre-scanned depth profile so that the surface of the specimen was drawn into the DOF of the lens. As a result, we were able to acquire homogenous quality OCM images regardless of the height difference of the sample surface.

3.2.1 Principle of Depth Trajectory Tracking Technique
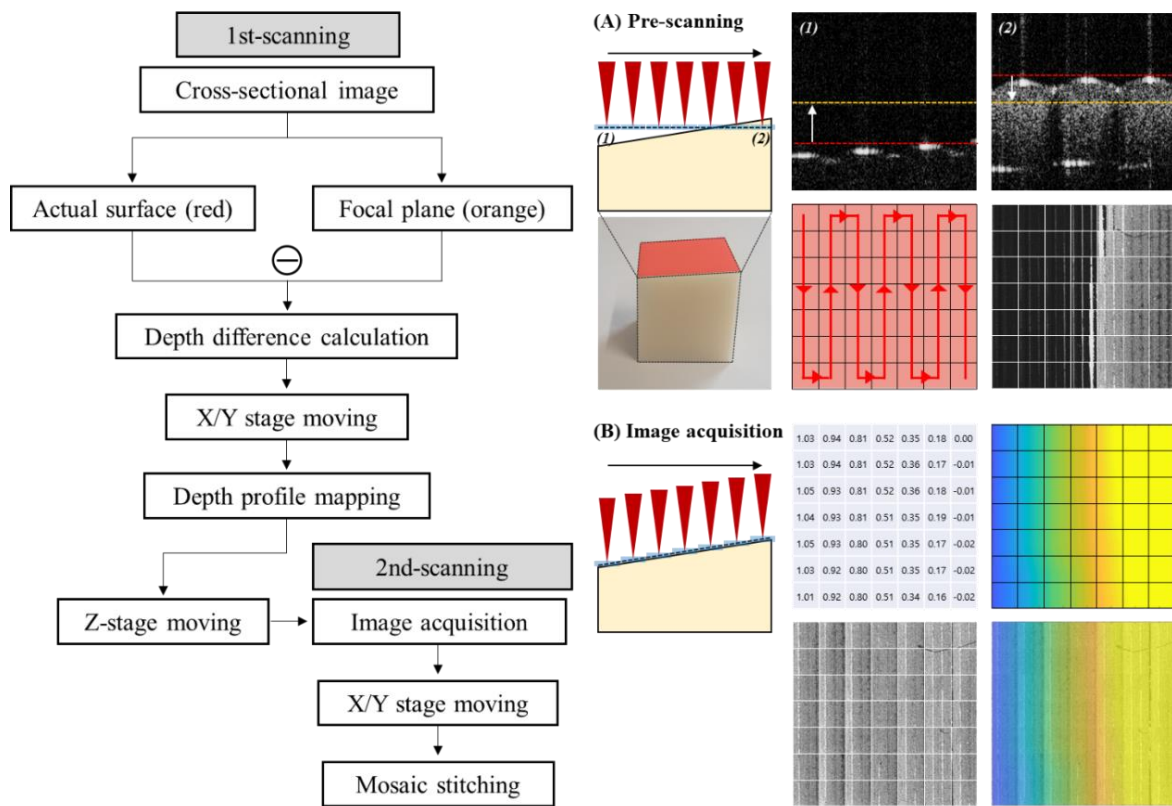
Figure 3-5. Principle and operating step of depth trajectory tracking technique in OCM *en-face* image acquisition. In the first scan by OCM, we utilized a low magnification objective lens which has large field-of-view and wide depth-of-focus to acquire height information between the surfaces of the sample. In the second scan, the OCM *en-face* image was acquired by adjusting the z-stage based on the previously acquired height information.

Figure 3-5 presents the principle and operating step of depth trajectory tracking technique to acquire fine quality images regardless of the difference in height of the sample surface. In here, 3D printed phantom with gradient slope on the top surface was utilized to evaluate the feasibility and demonstrate the algorithms. The flowchart explains the operating step including the first scan to obtain height information and the second scan to acquire images for depth trajectory tracking. At the first step, OCM scanned the sample with low magnification objective lens which has large field-of-view and wide depth-of-focus to acquire topological data and height information between the surfaces of the sample. The low magnification objective lens allowed to acquire larger cross-sectional window of the optical signals that used for finding the height changes on the sample surface. Also, low magnification is suitable for pre-scanning to acquire the height information because the wide depth-of-focus contributed to less signal reduction due to slope of tiled sample and curvature of the surface. The height information was subtracted surface line of sample (red line) from basement line (orange line).

The surface line was found by detecting the point of dramatic signal change in the axial direction of cross-sectional image. In the single *en-face* image, we acquired 250 cross-sectional images and the height information in single *en-face* image determined by averaging the height difference value of each cross-sectional image. The table of topology map obtained by previous process was plotted in Figure 3-5(B). In Figure 3-5(B) of the second scanning, the topology map obtained in the first scanning corresponds to the approximate slope over the area of interest where this is used for lookup-table for an axial position. The system used a topology map to re-scanned to capture the images which compensated the position or traced the slope of the sample. As an outcome, the gradient intensity over *en-face* image has been changed having reconstructed uniform surface intensity. While capturing the images, we performed the raster scanning to cover the whole area of interest and applied mosaic stitching to combine each *en-face* image to get wide field-of-view image.

3.2.2 High-quality Image Acquisition in Tilted and Uneven Tissue Surface
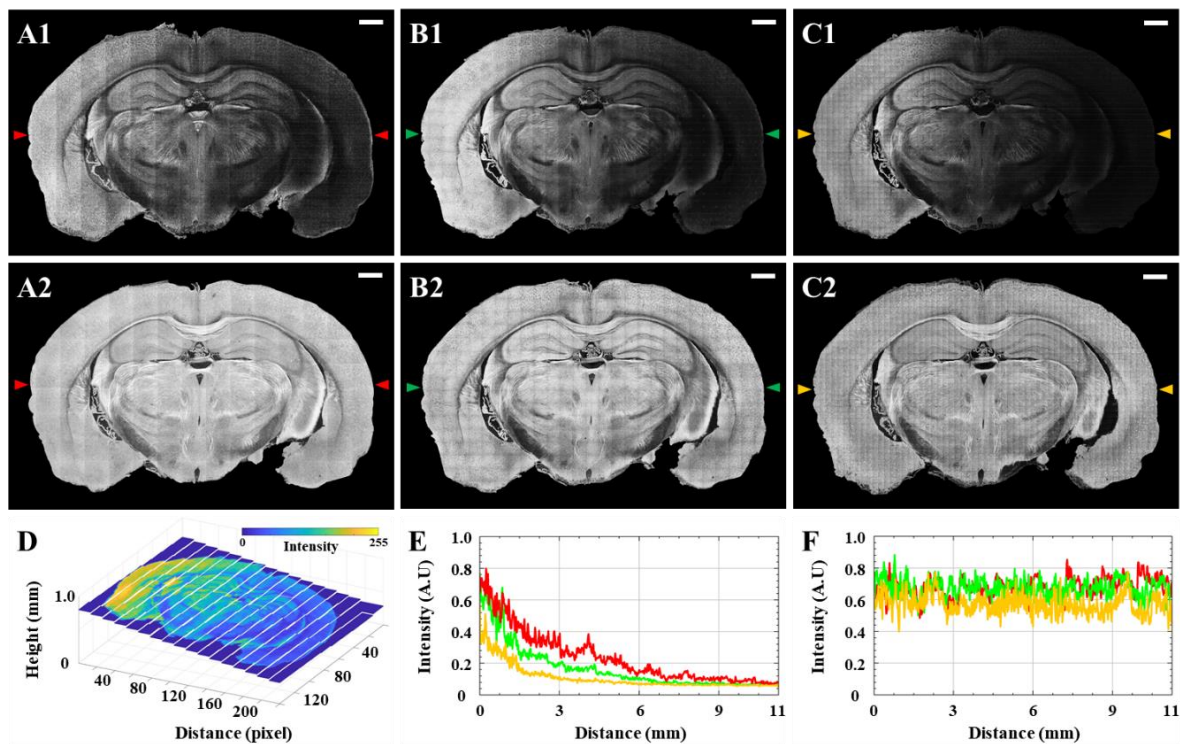
Figure 3-6. Trajectory OCM image of mouse brain following coronal section. (A1), (A2) 4X *en-face* image before and after depth trajectory-tracking technique, (B1), (B2) 10X *en-face* image, and (C1), (C2) 20X *en-face* image (scale bar: 1.0mm). (D) Depth trajectory-tracking result with image intensity in 4X magnification. (E) Image intensity graph along the horizontal line between triangle arrow in (A1), (B1) and (C1). (F) Image intensity graph in (A2), (B2), and (C2) after depth trajectory-tracking (red: 4X, green: 10X, and yellow: 20X magnification).

In Figure 3-6, we applied depth trajectory tracking technique to acquire mouse brain OCM image using multiple objective lens with 4X, 10X, and 20X magnification. For the brain imaging, 17 by 10 *en-face* images were captured using 4X objective lens. 30 by 17 image with 10X objective lens and 70 by 40 images with 20X objective lens were capture as shown in Figure 3-6(A)-(C). Figure 3-6(D) was plotted the *en-face* image shown in Figure 3-6(A1) according to each height information. In order to analyze the extent of the depth signal compensation, we derived the depth profile as shown Figure 3-6(E) and (F). Each red, green, and yellow line denotes the depth profile that is extracted from Figure 3-6(A)-(C). Since larger magnification provides shorter depth of field, Figure 3-6(C1) image shows more dramatic degradation of intensity slope than Figure 3-6(A1). On the other hand, trajectory-OCM images, shown in Figure 3-6(A2)-(C2) shows well recovered intensity information at the pixels where it had very low signal before. As shown in Figure 3-6(F), depth profiles from axial position calibrated images shows similar intensity gradient with approximately flat over the whole field-of-view. Throughout the depth information and its slope, we can evaluate the how well depth location of each *en-face* sections was calibrated.
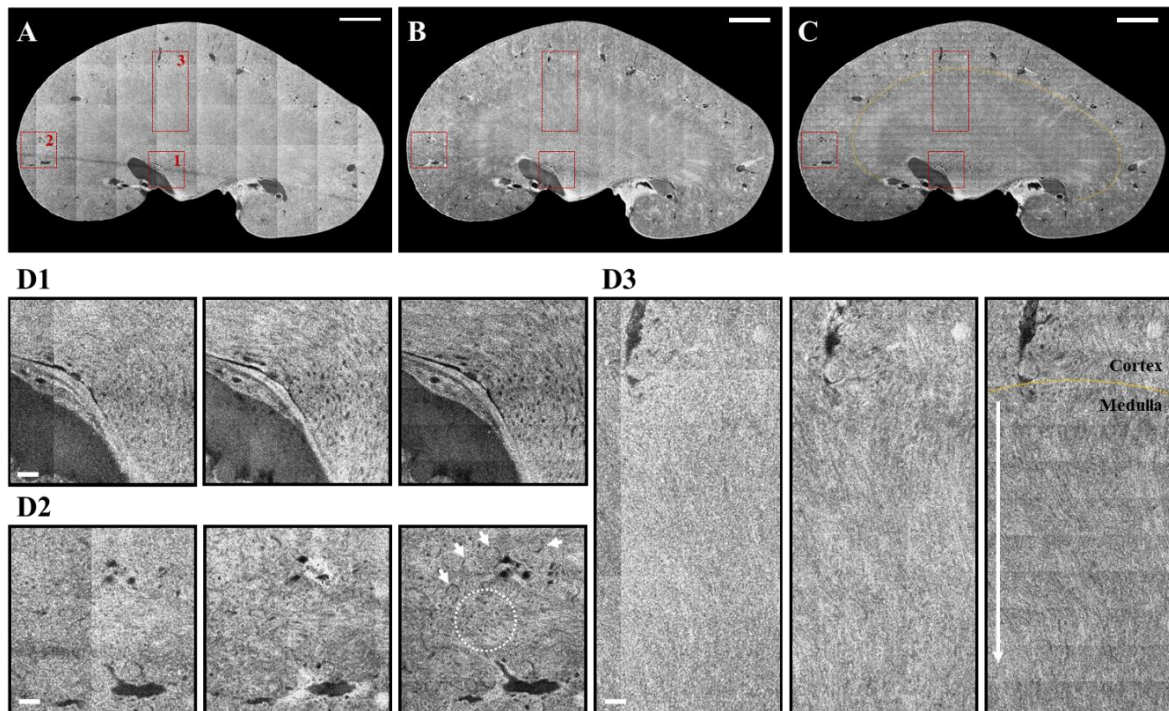
Figure 3-7. Trajectory OCM image of mouse kidney following midsagittal section. (A) 4X, (B) 10X, and (C) 20X *en-face* images (orange dot line: boundary between cortex and medulla area) (scale bar: 1.0mm). (D1) Comparison of resolution difference between each magnification from left side of 4X to right side of 20X, (D2) Magnified images of cortex area (white arrow: glomerulus, white dot circle: renal tubules), (D3) Magnified images of cortex-medulla boundary (white arrow: direction of straight tubes and collecting ducts) (scale bar: 100μm).

Furthermore, we compared the structural features of mouse kidney from the depth trajectory tracking OCM images according to different magnifications as shown in Figure 3-7. The kidney was harvested from the C57BL/6 mouse and sliced in 500 μm by vibratome. With limited transverse resolution, morphological features of the kidney were not identified in the 4X *en -face* OCM image in Figure 3-7(A). With higher magnification, the tissue structure was better visualized as shown in Figure 3-7(B) and (C). The 20X image further enhances the cell visibility which also clearly exposes glomerular in the tissue. Furthermore, images from the highest magnification showed the lowest speckle-noise due to higher sampling numbers. Higher the magnification, larger the number of *en-face* sections used to reconstruct the whole *en-face* image.

Discussions and conclusions

Compared with conventional OCM systems, the system complexity was reduced because the variation of the path length delay caused by the scanning mechanism penetrating the thick lenses could be compensated through post-processing. However, there is still a limitation found in the proposed imaging method. The surface of the sample may not be perfect due to uneven force applied while sectioning the tissue using vibratome. Thus, in some cases, tissue may be torn, or tissue could be bent. Also, non-parallel tissue positioning or misalignment of a blade in the vibratome could provide a large slope angle on the surface. This could let out of focus or depth-of-focus, which results in lacking information in the cross-sectional image while scanning with the lowest magnification. Therefore, it may be unavailable to compensate for the intensities or compute the topology map.

In summary, to evaluate the performance of the system, we applied several different NA objectives to the system and used various mouse tissues to obtain high-resolution images revealing the fascinating advantages of this method. Throughout the experiment, we have found that our innovative method is very robust, hence, applicable to any depth-resolving microscope for providing very clear and uniform images to the user.

3.3 Serial Block-face OCM for High-resolution Whole Tissue Imaging

The volumetric visualization of biological tissues is very important to identify morphological changes and tissue abnormality for medical and biological applications. Despite the clear needs for high-resolution and deep-tissue imaging, it has restrictions to enhance the light penetration into the tissue. There have been few studies to obtain the three-dimensional whole tissue structure, such as tissue clearing technique and physical serial sectioning method [49-53]. However, the problem was remained such as change and damage of tissue structure, complex procedure with time-consuming, as well as labor-intensive issues. Here, we suggest an automated serial block-face optical coherence microscopy (SB-OCM) system that combined a block-face imaging technique and optical coherence microscopy for label-free whole tissue imaging. The SB-OCM system was developed to perform automatically physical tissue sectioning and optical imaging without intervention by an operator. To evaluate the whole tissue imaging capability, we visualized various mouse tissues and confirmed that SB-OCM has merits in terms of resolution, throughput, field-of-view and penetration imaging depth. Since SB-OCM provides label-free imaging, it has a potential for application in histopathological studies. Besides, it would be a useful platform to provide fast feedback of volumetric tissue nature when the staining or labeling is difficult to access.

Visualization of three-dimensional (3D) morphological structure of tissues is very critical to quantitatively analyze the tissue abnormality in various medical or biological applications. Even though there are clear needs for high-resolution and deep tissue imaging capability in optical microscopy, it has inherent restrictions to enhance the light penetration into the tissue due to the high scattering of turbid biological specimens. To overcome this, we need to take new technology which provides either transparency of tissue or deeper light propagation using a longer wavelength of light. For this reason, several tissue clearing methods have been applied for deep tissue imaging through the elimination of major scattering components such as a lipid [54, 55]. Although it presents enhanced imaging depth in optical microscopic research, it is not still enough to visualize the various thick tissues while preserving the original structure as well as size. In another way, to acquire 3D tissue information, the biological tissue physically sectioned and reconstructed by stacking the microscopic images in an axial direction [56]. If this method is fully automated, it would be a very useful and efficient tool toward deep tissue imaging over labor-intensive conventional manual sectioning and imaging way [57].

Here, we demonstrated a user-friendly deep tissue imaging apparatus based on a block-face imaging technique and optical coherence microscopy. The serial block-face optical coherence microscopy (SB-OCM) system was made in the automated system performing a large field-of-view optical imaging and physical tissue sectioning of the agarose-embedded tissue. Our home-built SB-OCM allows high-

speed *en-face* scanning in the wide-area operating by the motorized stage and mosaic method. To evaluate the deep tissue imaging capability, we tried to image various mouse organs including the brain, liver, kidney, and heart.

3.3.1 Serial Block-face Imaging Technique: Whole Kidney Imaging with Vessel Segmentation

The principle of serial block-face imaging is the method of obtaining three-dimensional information of a biological tissues or specimens by repeating imaging and tissue sectioning [58]. The part of the tissue was imaged using the optical imaging device, and the imaged part or layer of sample was cut by vibratome to expose the new tissue layer which was not acquired.
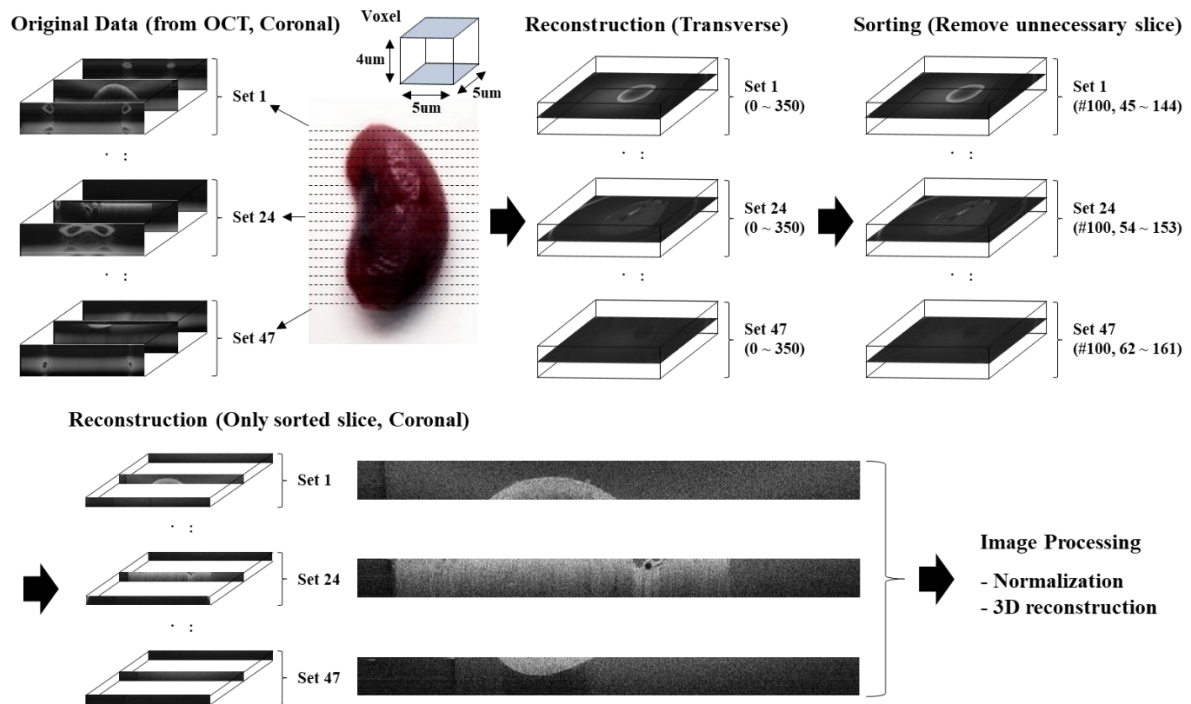
Figure 3-8. Steps of image acquisition, sorting and reconstruction for serial block-face imaging technique.

Figure 3-8 presents the steps of image acquisition, sorting, and reconstruction in serial block-face imaging for whole tissue imaging. The serial block-face OCT is a technique for acquiring three-dimensional images of morphological information in the biological specimens by reconstructing data sets acquired repeatedly by tissue sectioning and OCT image acquisition. OCT provides structural and morphological information of the biological tissues in deep penetration depth, enabling high-throughput whole tissue imaging through integration with serial block-face technique. We utilized the agarose embedded mouse kidney harvested from C57BL/6 (5 weeks, male) under the anesthesia to acquire 3D whole kidney structure using serial block-face OCT system and the thickness of each

sections was determined to 200 μm which was optimized by the depth of focus and penetration depth of the OCT system.
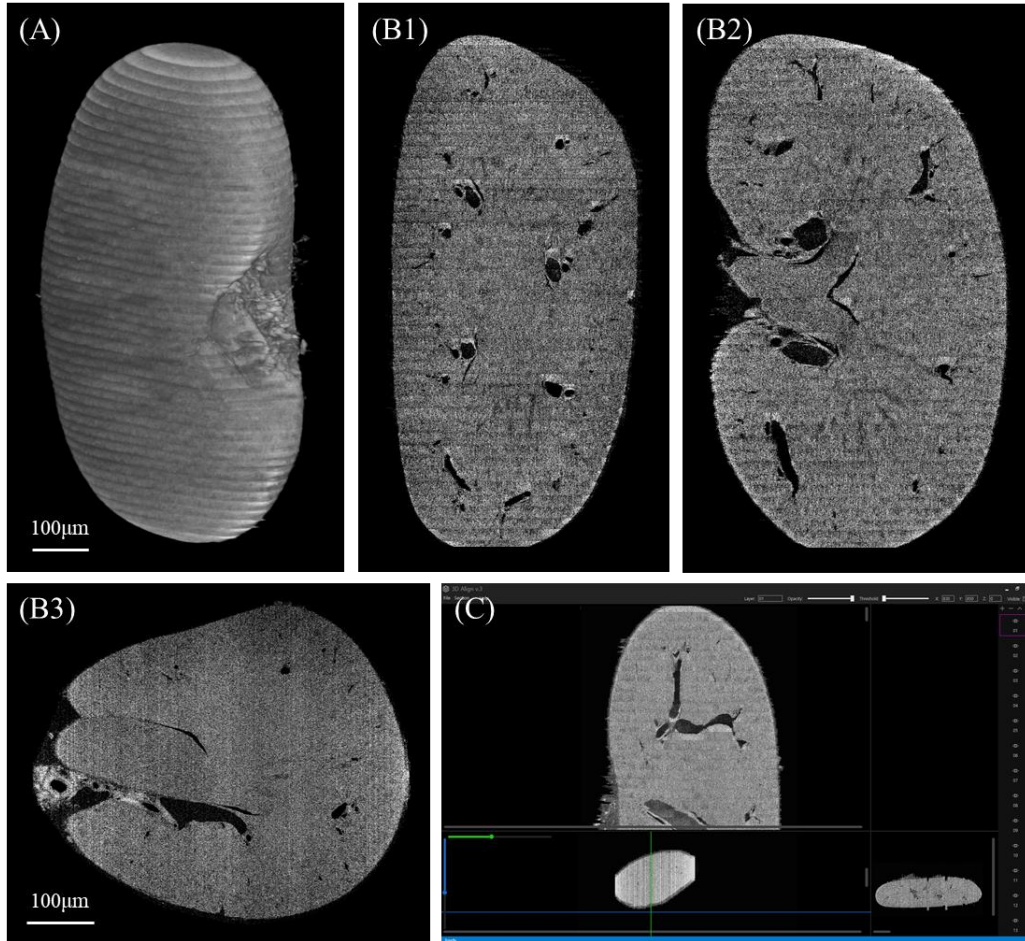
Figure 3-9. Whole tissue imaging of mouse kidney using OCT imaging with serial block-face technique. We acquired a total of 47 blocks of 3D OCT images from the agarose embedded kidney sample by the repetition of OCT imaging and tissue sectioning of vibratome. (A) 3D structure of mouse kidney acquired from serial block-face OCT, (B) Sagittal, coronal, and transverse plane of 3D kidney image, (C) Home-built software for stitching and alignment of multiple image blocks.

Figure 3-9 shows a three-dimensional reconstruction of the mouse kidney using the serial block-face OCT imaging described earlier. We acquired a total of 47 blocks of 3D OCT images from the agarose embedded kidney sample by the repetition of OCT imaging and tissue sectioning of vibratome. In the coronal and transverse section, we observed the various structures in the mouse kidney as well as the renal blood vessels. We utilized home-built software to confirm and adjust the position during an image stitching process on three different axes simultaneously for correct connection of 47 blocks.
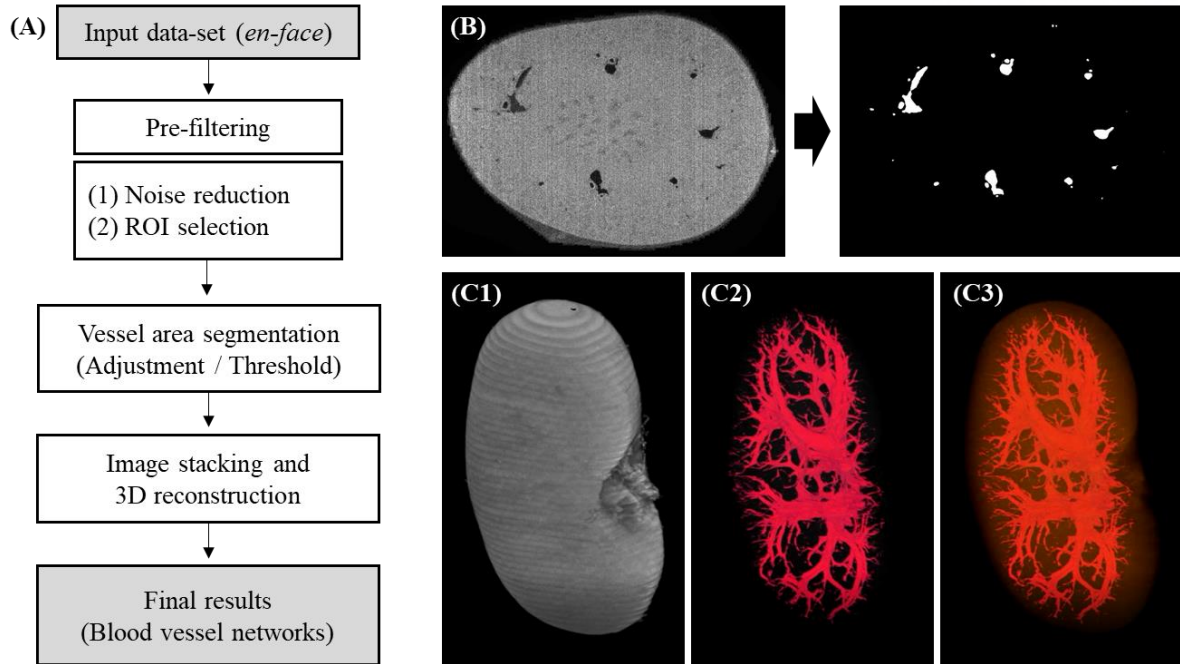
Figure 3-10. (A) Segmentation process of blood vessel networks in mouse kidney, (B) Vessel segmentation based on adjustment and threshold, (C) 3D reconstructed mouse kidney and blood vessel networks with merged image.

In Figure 3-10, we performed the segmentation of renal vessel structure for quantitative analysis in whole kidney structures acquired using serial block-face OCT. As shown in Figure 3-10(B), the structure of renal blood vessels was observed concerning the surrounding renal tissues. Therefore, we segmented the renal vessel networks through the adjustment of the image intensity and the threshold parameters. We stacked and reconstructed the segmented vessel structures to visualize the three-dimensional vessel networks within the mouse kidney. Also, we observed the structure of micro-vessels that reached the superficial layers in outer part of the kidney. Here, we utilized tissue sectioning using vibratome and deep-tissue imaging of OCT modality to validate three-dimensional whole tissue imaging based on serial block-face technique. However, the automated systems are still required because it takes a lot of time and labor to work repeatedly with tissue sectioning and optical imaging. Also, the automation of serial block-face imaging facilitates three-dimensional imaging of large volume of tissues and it allows high NA lens to acquire three-dimensional tissue images with higher resolution, despite the decrease in the number of tissue sections due to the reduction of the presentation imaging depth.

3.3.2 Hardware Configuration and Specification of SB-OCM system
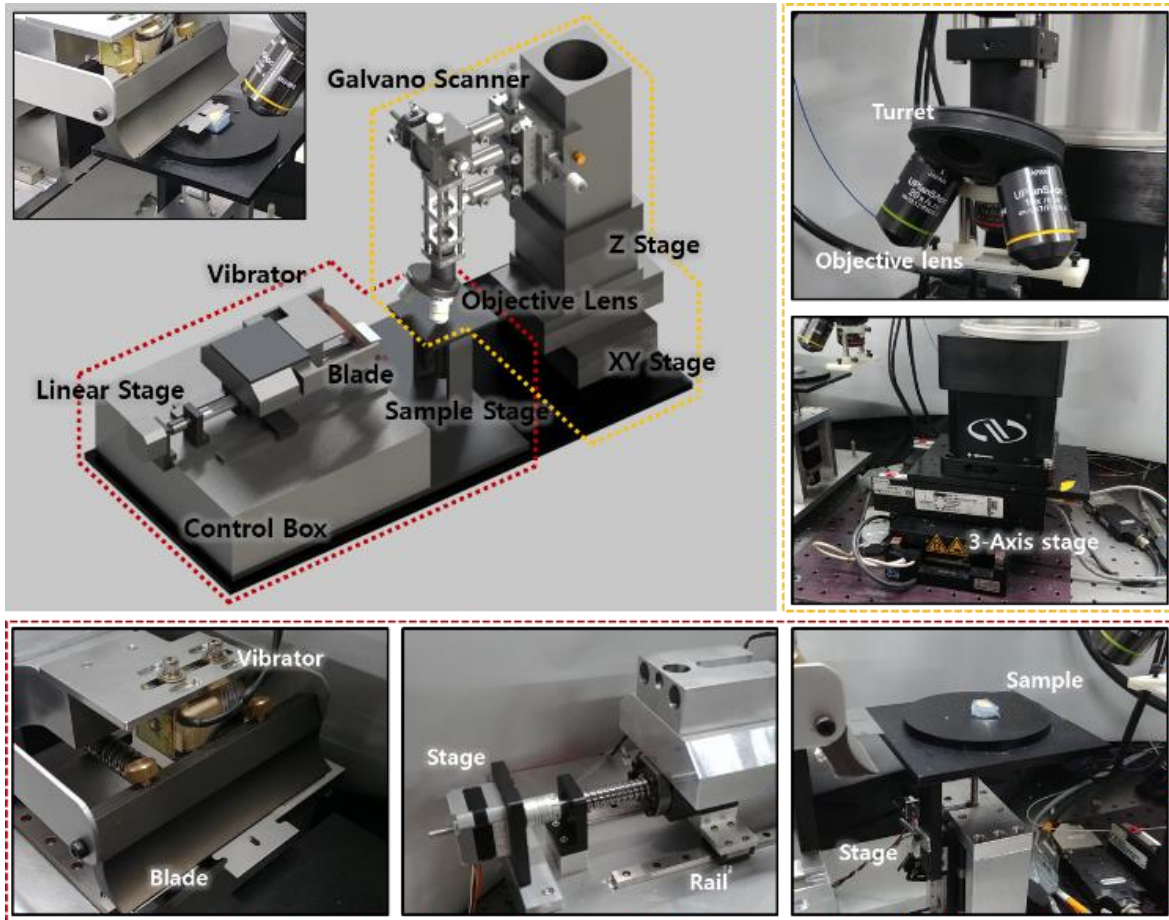
Figure 3-11. System schematics of the serial block-face optical coherence microscopy (SB-OCM). The customized vibratome controlled vibration intensity, frequency, and sectioning velocity through RS232 communication. A various magnification can be offered by integrating microscope turret with 4X, 10X, and 20X. We implement the highly precise linear stage to get high-resolution tissue image in the wide field-of-view.

We developed a swept-source based SB-OCM system to obtain high-resolution 3D tissue image as shown in Figure 3-11. Our system was designed and fabricated as an automated apparatus in imaging and sectioning protocols. The swept-source laser was operated at a 1310 nm central wavelength with a 110 nm tuning bandwidth at a rate of 100kHz, which provided ~7 µm axial resolution in air. The emitted light from the swept laser is divided into two optical paths at the fiber coupler and each light delivered to the sample and the reference arm through an optical circulator. The sample arm consisted of a collimator and a galvanometer scanner. Also, a telescope was employed in the sample arm in our system to enlarge the beam diameter. At the end of the sample arm, we used 4X, 10X, and 20X objective lens offering a lateral resolution of ~2.7, ~1.6 and ~0.6 µm in air, respectively. Two reflected lights returned from the sample and the reference arm are interfered with by Mach-Zehnder

interferometry, which was converted to an electrical signal by a balanced photo-detector. At the very end of the detector, we utilized a digitizer to acquire an intensity-based profile that indicates depth information (A-line). To visualize the 2D or 3D images, we accumulated the A-line profiles according to X and Y directions by using a two-axis galvanometer scanner.

SB-OCM comprises three-axis (XYZ) motorized stages with a programmable image mosaic technique to achieve wide-field OCM images. Following the acquisition of a single OCM volumetric data, the X and Y axis motorized stages moved the sample to the next position to capture adjacent OCM volumetric data. This process continues until OCM images cover an entire tissue surface. After capturing the entire imaging section, the system automatically moves the sample in front of the vibratome using a linear motorized stage to remove the upper part of the sample where was acquired to acquire the next imaging section. Then, the sample was returned to the original position to carry out the next imaging process. All process with three-axis stages was fully automated and controlled by LabVIEW software using RS232 serial communication protocol. The acquisition time for the single mosaic volume was ~ the 30 s and it enabled imaging the entire mouse brain within 8 hours.
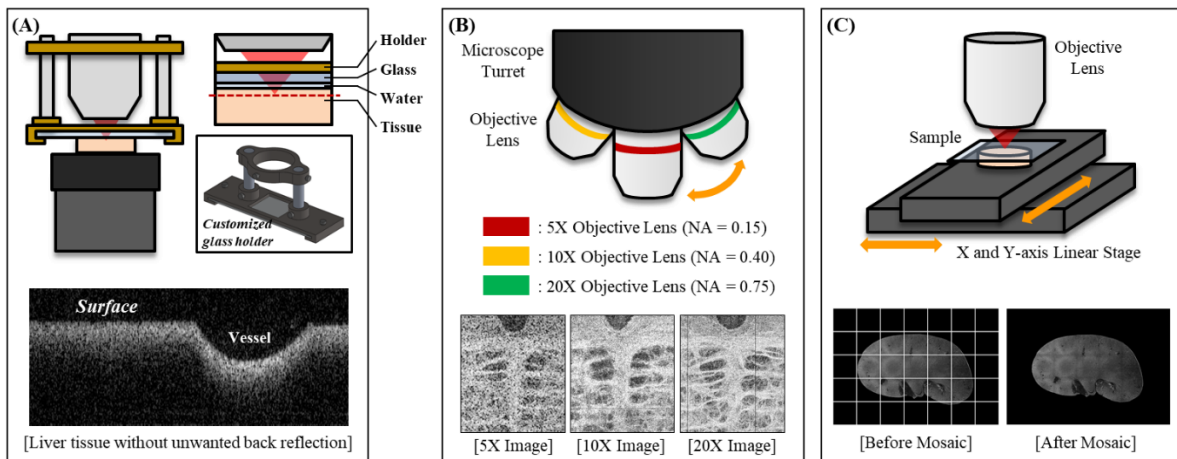
Figure 3-12. Major specification of SB-OCM system for automated whole tissue imaging. (A) Design of the 3D printed holder to suppress the unwanted back reflection from the sample surface. (B) Microscope turret integrated with multiple objective lens for various magnification in OCM imaging. (C) Precise linear stage for acquisition of high-resolution tissue image in the wide field-of-view.

In Figure 3-12, we put some effort to obtain fine quality image by reducing unwanted back reflection from the sample surface. In order to do this, we used 3D printer and made a holder to place a glass plate between sample and objective lens. As you can see in the figure, we designed to provide a space of few microns between glass plate and sample, so we can put a water on there for reducing the reflection. Another feature is that various magnification can be offered by integrating microscope turret. We mainly used 5X objective lens which have 0.15 numerical aperture, however a 10X or 20X

magnification image can be provided at specific regions. Moreover, we implement the highly precise linear stage to get high-resolution tissue image in the wide field-of-view. Single OCM image, captured by 5X objective, only has 2 by 2 mm field-of-view, but after mosaic stitching, we can obtain the image in 14 by 10 mm area as you can see in this figure.

For the validation study, a four-week-old C57BL/6 mouse was employed. Under anesthesia, transcardial perfusion was performed using phosphate-buffered saline (PBS) solution followed by 10 % neutral buffered formalin (PBS) solution to remove the blood before harvesting tissues. All animal protocols were approved by the Animal Care and Use Committee in Ulsan National Institute of Science and Technology (UNIST). The formalin-fixed mouse tissues were embedded in the 10 % of low melting point (LMP) agarose gel. Before imaging, the agarose-embedded tissue sample was trimmed by vibratome to smooth the surface for better imaging performance. Moreover, in order to avoid the dehydration, the sample should be remained in the water.

3.3.3 Protocol for Fully Automated Whole Tissue Imaging
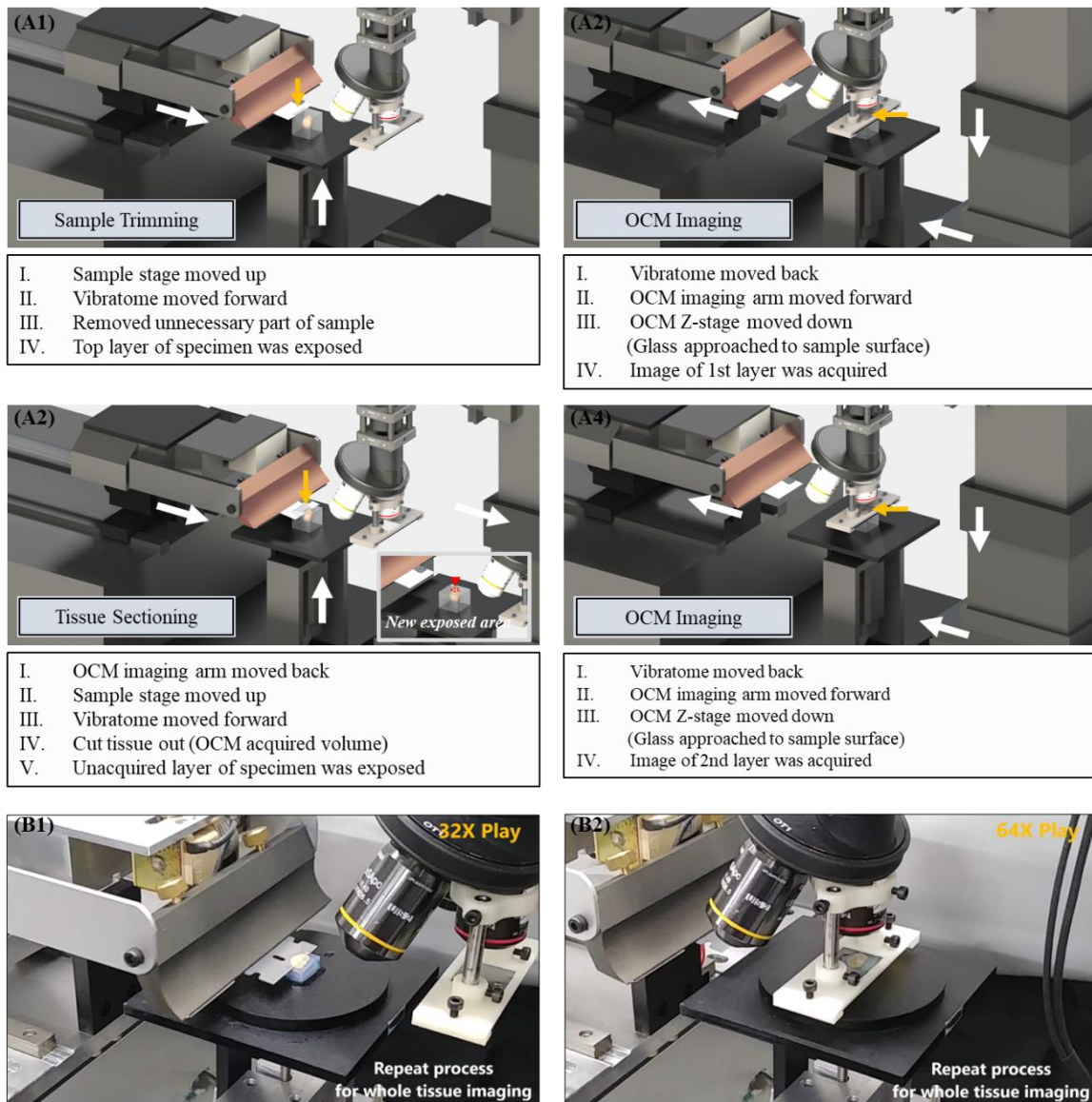
Figure 3-13. The automated operation step of serial block-face OCM system. (A1) trimmed the unnecessary part of the agarose embedded sample, (A2) obtained OCM image from the top layer of sample, (A3) sectioned the tissue about 100um thickness, (A4) acquired the image in second layer. Actual operation of (B1) tissue sectioning by vibratome, (B2) imaging acquisition by OCM system.

The automated operation of serial block-face OCM system consisted of three steps; (1) system initialization and sample trimming, (2) OCM imaging acquisition, and (3) tissue sectioning by vibratome as shown in Figure 3-13. Before the starting of image acquisition, we set the vibratome and image acquisition part of OCM at the initial position. The vibratome head moved along the rail suing linear stage toward the sample and the imaging arm moved to acquire the image after the sectioning process was finished. After each device moved to its initial position, we trimmed the unnecessary part

of the agarose embedded sample. For more details, the sample attached stage raised and trimmed the sample until upper layer of tissue was exposed. After the trimming process, the vibratome head moved back to the initial position and the imaging arm of OCM moved forward to assigned position with z-axis stage moving down to the sample for the focal position. In the next step, OCM *en-face* image obtained in the top layer of the sample. The sample arm automatically captured the image within the certain region by performing the mosaic stitching. After the image was obtained from first layer, the imaging arm of OCM moved back to initial position and the sample was raised 100 μm up to slice the previous capture layer. The vibratome head moved toward the sample and sectioned the tissue to a 100 μm thickness. This process made to expose a new layer of the tissue. In the final step, the vibratome also returned back after sectioning, imaging arm moved to acquire the image in second layer. We acquired a three-dimensional image of the whole tissue by repeating tissue sectioning and OCM imaging.
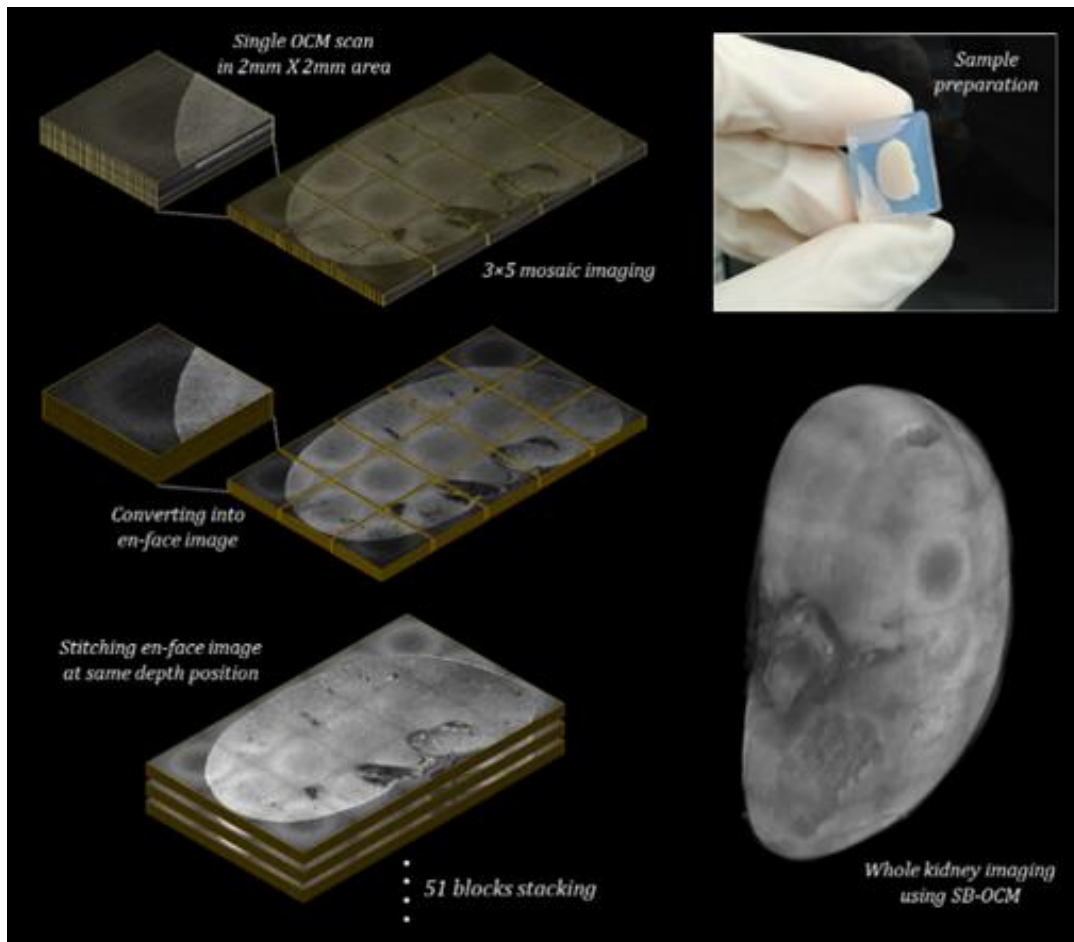
Figure 3-14. Image reconstruction process for whole tissue imaging. Moved the linear stage to perform mosaic imaging. Cross-sectional image converted into *en-face* image. Stitched *en-face* images at the same depth position. Reconstructed the 3D image blocks obtained by repeating sectioning and imaging.

Figure 3-14 presents the processing of image reconstruction for whole tissue imaging. First, the single OCM data-set was acquired and it consisted of 250 cross-sectional images in 2 mm × 2 mm area. We acquired multiple OCM data-set to reconstruct a single block for the entire area of the sample using a mosaic imaging method. The single block of mouse kidney consisted of 15 OCM data-set of 3 × 5 by the mosaic method and each OCM data-set converted to 100 *en-face* images. The *en-face* images located at the same depth position in each OCM data-set were stitched to generate a single large en-face image. We acquired a total of 51 blocks based on previous processing for 3D reconstruction of mouse kidney by repeating physical tissue sectioning and OCM image acquisition. The whole kidney structure was reconstructed by stacking all of the en-face images.

3.3.4 High Throughput Whole Tissue Imaging for Histopathological Study
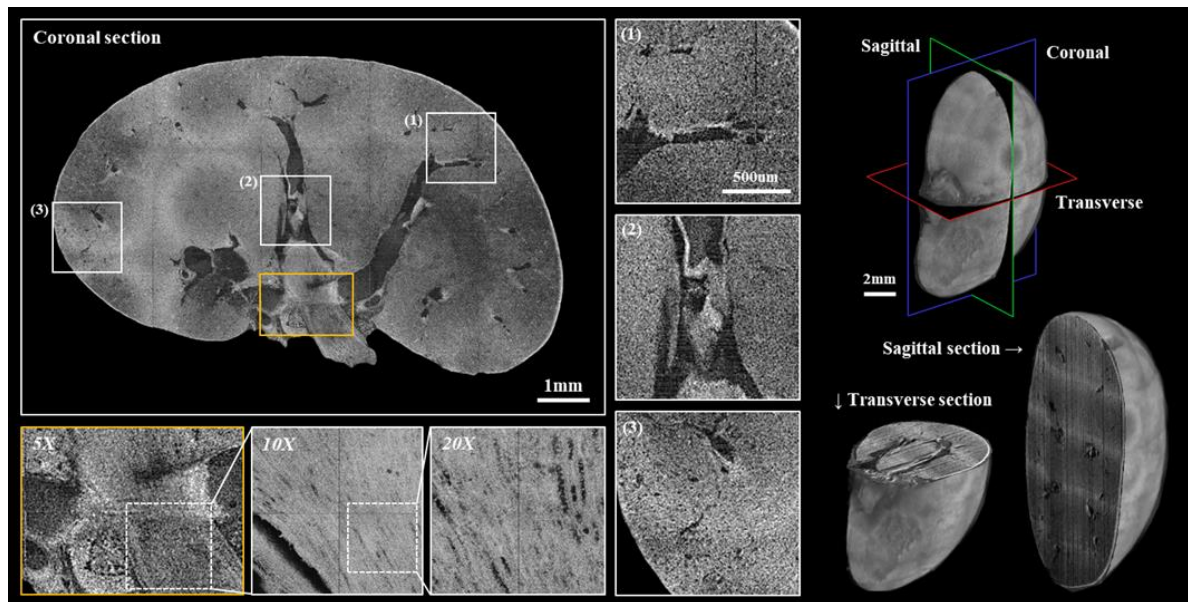
Figure 3-15. Whole tissue imaging of mouse kidney using SB-OCM system. Whole kidney structure was reconstructed by stacking a total of 51 image blocks. In the coronal section, we confirmed clear morphological structures of kidney tissue. SB-OCM provides a high-magnification image in specific region-of-interest (ROI) where we selected during the image acquisition process. The 3D reconstructed whole kidney presented sagittal and transverse section as well as the coronal section of mouse kidney with high-resolution histopathological information.

We acquired high-resolution three-dimensional kidney images through the automated whole tissue image acquisition of SB-OCM. The three-dimensional kidney image in Figure 3-15 was obtained by repeating a total of 51 tissue sections and OCM imaging. In the coronal section, we can see the details of the mouse kidney structure. We observed the morphology of the components in detail that consist of the kidney tissue structure as well as the clear form of blood vessels in the kidney tissue. We also

confirm the kidney structure in the transverse and sagittal sections. In addition, if we set the specific region where we have an interest, we can acquire a 10X or 20X high magnified image during the automated SB-OCM process. In the results of the multi-scale image, we identified the clear structure of the interior wall of the ureter with a sub-cellular level. The biggest advantage of whole tissue imaging using SB-OCM is that researchers can observe the three-dimensional morphologies and structures of the tissue at the desired location and direction. We were able to identify the internal structure of the kidney in various directions using whole tissue imaging of the mouse kidney.
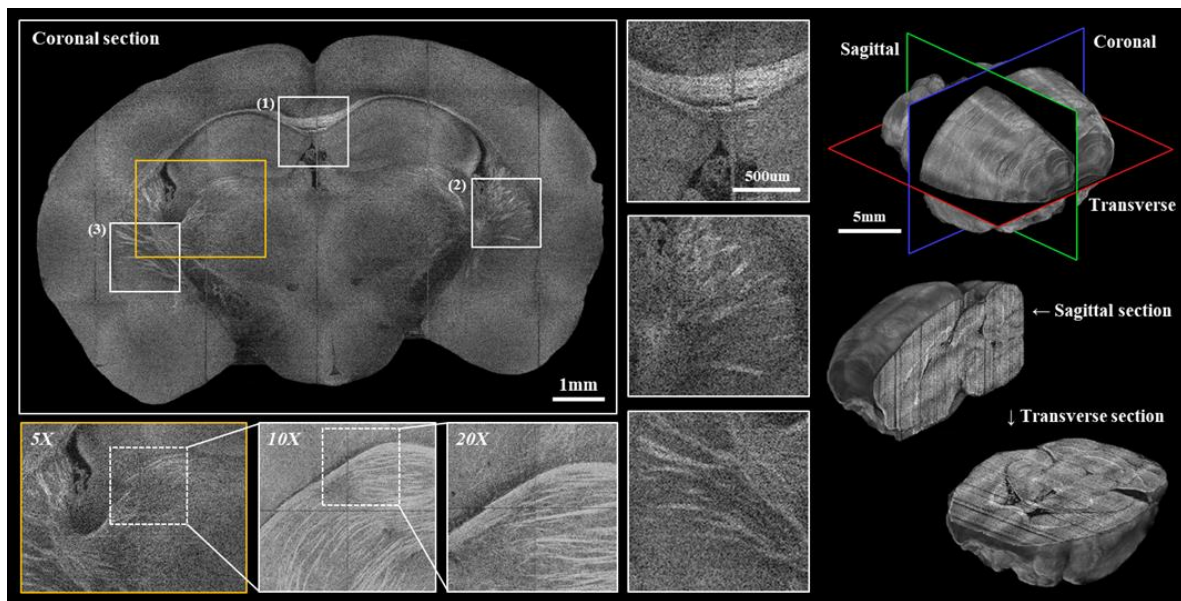
Figure 3-16. Whole tissue imaging of mouse brain using SB-OCM system. Whole brain structure was reconstructed by stacking a total of 121 image blocks. In the coronal section, we confirmed clear morphological structures of brain tissue. The sharp contrast of the neural fibers was observed in the image. SB-OCM provides an analytical level of information about the orientation and alignment of neural fiber in the whole brain structure.

We also acquired high-resolution three-dimensional brain images using the automated whole tissue imaging of SB-OCM. Figure 3-16 shows three-dimensional high-resolution brain images acquired from SB-OCM in different sections. The three-dimensional brain images consist of 121 image blocks and were reconstructed into three-dimensional images using home-built software for the alignment of image blocks. In the coronal section, we identified various structures of brain tissue with high-quality images. In particular, the neural fiber was observed as high contrast, which allows an analysis of the orientation and distribution of the neural fiber. Also, the structure of the natural fiber was clearly observed after taking high-resolution images of 10X and 20X in the area where the neural fiber was assembled. It is expected that these analyses will be used in future studies to analyze neural fiber networks in the whole brain. In addition, we identified the internal structure of the brain in the sagittal

and transverse sections. Through this study, we obtained high-resolution three-dimensional images of the mouse brain and confirmed that whole tissue imaging of SB-OCM provides high-quality internal structural information of the brain. We are going to conduct an application study on future brain-related diseases and structural changes in the brain depending on the environment.
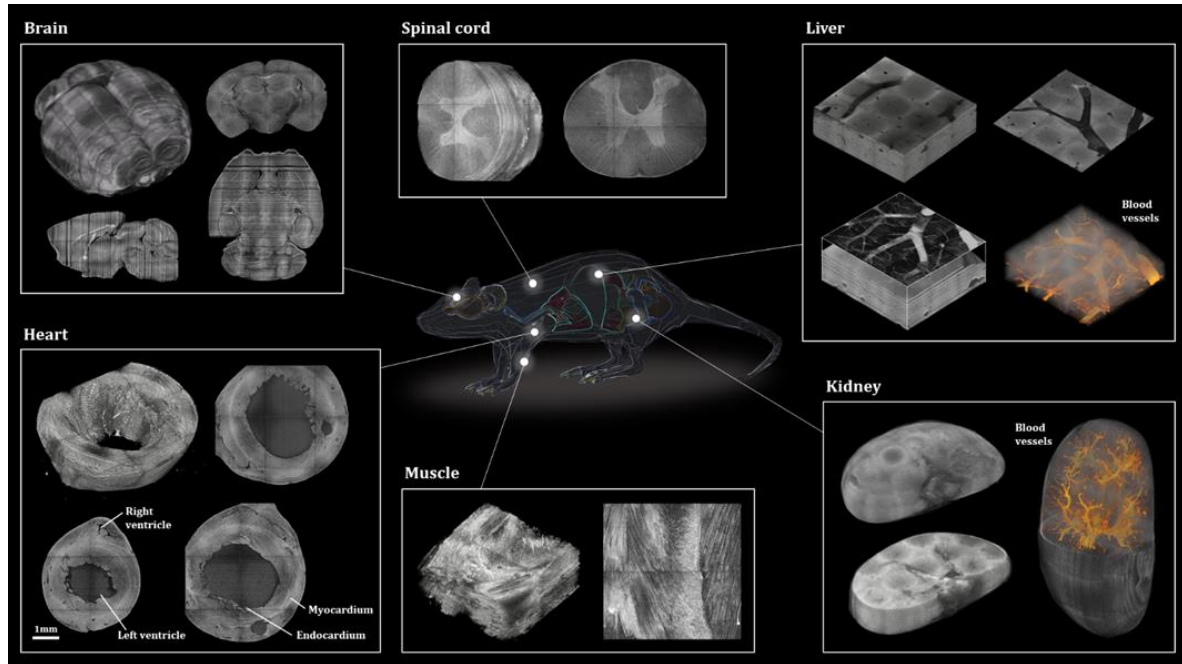
Figure 3-17. Mouse three-dimensional atlas from whole tissue imaging by SB-OCM system. Three-dimensional reconstruction and visualization of various mouse tissues presented as the mouse organ atlas. The 3D reconstructed the heart, liver, spinal cord, and muscle as well as the brain and kidney presented in the atlas map of mouse organs. SB-OCM is a promising platform to provide 3D histopathological information using its capabilities in terms of high-resolution, high-throughput, and the automated image acquisition process.

We obtained high-resolution whole volume images of various tissues such as the brain, heart, and kidney using by the SB-OCM system. Figure 3-17 shows a representative data which is a label-free three-dimensional tissue image in each specific region with high-resolution.

In the whole tissue imaging of the brain in Figure 3-17, we identified a clear tissue structure of high resolution in each coronal, sagittal, and transverse direction of the three-dimensional brain image. In the case of discrete noise in images due to physical tissue sectioning, it can be solved by system optimization and optics alignment. The three-dimensional spinal image shows the clear structure and orientation of the neural fiber. The network of the neural fiber can be segmented through image processing and it applied to research of spinal cord nerves. In the three-dimensional reconstructed heart image, we confirmed the clear structure of the heart as well as tissue morphologies such as

ventricles, myocardium, and endocardium. These high-resolution three-dimensional heart images can be used in the study of diseases or genetic disorders that affect the formation of the heart. We also observed the clear structure and orientation of muscle fibers in three-dimensional muscle tissue. Since muscle tissue is difficult to analyze by the tissue staining method, it is expected that a variety of studies can be conducted using SB-OCM. In the three-dimensional liver image, we observed the structure of numerous existing blood vessels. Since the shape of the vessels is clearly distinguished in OCM images, we extracted only the vessel segment through image processing. Projection images and three-dimensional vessel images of vessels in the liver tissue are acquired, enabling quantitative analysis of the vessels. The various structures and orientations of the vessels, as well as the order of the vessels, can be clearly observed, so it can be applied to the study of various diseases related to the vessels. We also observed the distribution of blood vessels in the kidney by segmenting the vessels in the previously acquired three-dimensional high-resolution kidney images. As a result, we were able to observe the microscopic capillaries that extended to the outside of the kidney. It is expected that this method of vascular quantification will allow the observation of morphological changes in blood vessels in kidney diseases which causes destruction of vascular structure and provide quantitative indicators for diagnosis.

Discussions and conclusions

Here, we introduce the automated SB-OCM system which combined wide-range optical imaging and physical tissue sectioning. Through our preliminary study, we successfully visualized various mouse organs and confirmed that it has many advantages in terms of field-of-view, resolution, throughput, and penetration imaging depth. We focused on system automation in this time to acquire the entire volumetric image of the tissue while repeating imaging and sectioning. It is necessary to improve in optical alignment and software modification for system optimization and further applications. Also, we are studying advanced high-throughput imaging based on SB-OCM by applying tissue clearing technique and DOF enhanced optics. Since our system is based on label-free imaging, it would have the potential for various histopathology studies. It would be a very useful tool when fast feedback of 3D tissue nature is required and staining or labeling is difficult to access.

CHAPTER 4. Hand-held Probe based Portable OCT System for Human Target Study

4.1 Hand-held Probe based portable OCT System

In this chapter, we introduce the hand-held probe based portable OCT system for human target pre-clinical and clinical studies. In addition to the studies described early chapters, most optical imaging devices, particularly in *ex vivo* and *in vitro* studies, are utilized in the form of bench-top system in the laboratory. However, the bench-top type imaging equipment has difficulty to access image acquisition in the human target study, also it has an inconvenience when working in different positions or when moving outward. We developed a hand-held probe with portable OCT imaging system to overcome these problems. The hand-held probe can be conveniently accessed by users, and image acquisition is possible regardless of the shape or position of the target. Also, we integrated the OCT system into the medical cart to implement the portable OCT system that allows convenience image acquisition in any positions and locations.

4.1.1 Development of Hand-held Probe
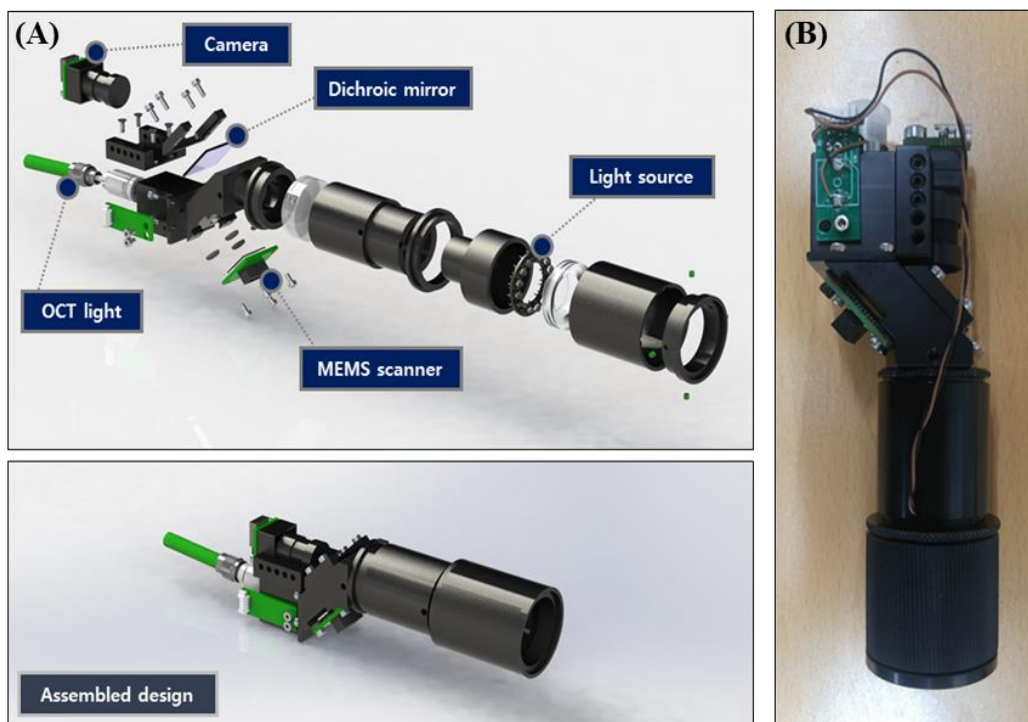
Figure 4-1. (A) Schematic diagram of optics for hand-held probe before and after assembly, (B) Final assembled optical part of hand-held probe for easy approach to human skin study.

For the development of the hand-held probe, it is very important to miniaturize the size of hand-held probes while maintaining the same performance of the bench-top type image acquisition arm. As shown in Figure 4-1, the optical systems of hand-held probe consisted of optical fiber connector capable of delivering the OCT light source, miniature camera for imaging of target surface, dichroic mirror to separate the visible light and near-infrared light, the small LED module for surface photography of the camera, and the MEMS scanner for three-dimensional tomographic imaging. The grip type hand-held probe, which will be used as a sample arm for acquiring OCT images, was manufactured by adopting a MEMS scanner in place of the galvanometer scanner of the existing OCT imaging system for miniaturization. Here, we have integrated a miniature camera module for the acquisition of surface images of the skin as well as OCT images.
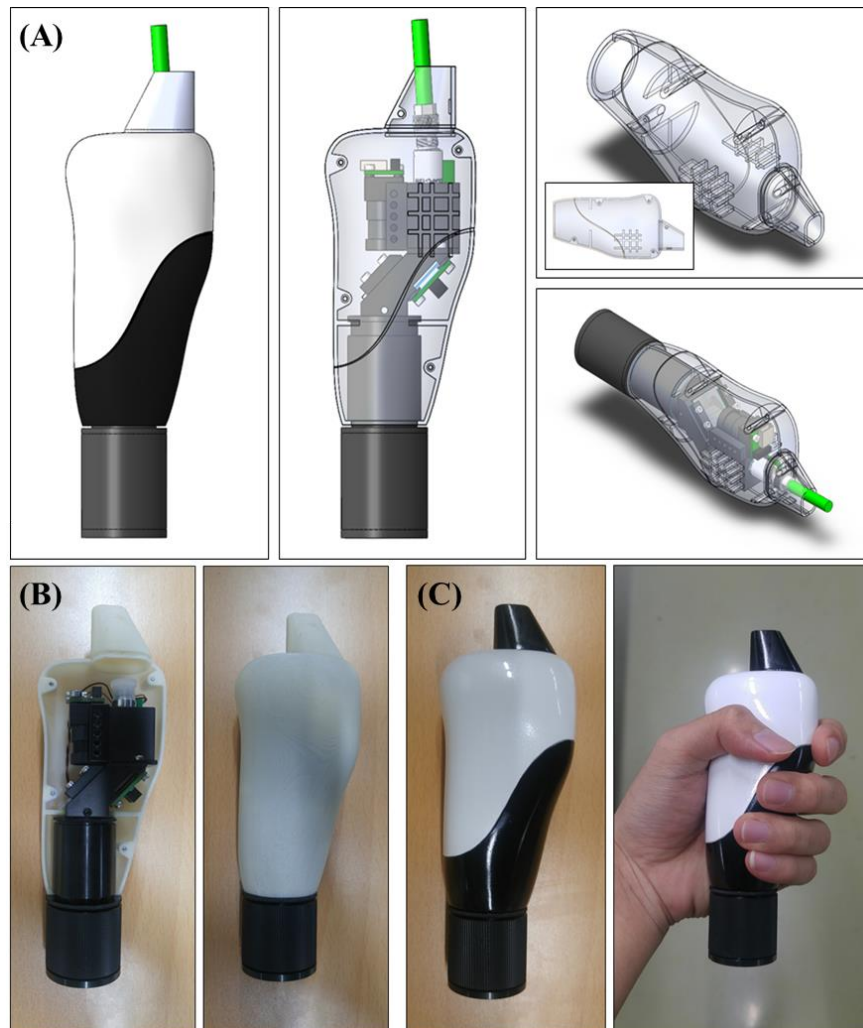
Figure 4-2. (A) 3D CAD design for manufacturing grip type hand-held probe. The grip type hand-held probe was designed enable to stable and comfortable image acquisition when the user was approaching a target using a probe, (B) Prototype hand-held probe with 3D printing, (C) Final assembled grip type hand-held probe.

In Figure 4-2, the probe case was designed with ergonomic design and weight for ease of use by the user for extended periods of time. We designed the probe conceptually using Solidworks software, which is a 3D rendering tool and produced a prototype using a 3D printer (Fortus 250mc, Stratasys Ltd.). to test the actual operation of the user. And then, we gathered the user's opinions and modified the design to produce the final product of the grip type hand-held probe. Improved accessibility of grip type hand-held probe will enable stable tomographic imaging in curved skin or the region, which is difficult to access, and various surface image analysis is expected through integrated camera modules.

4.1.2 Portable OCT System with Hand-held Probe
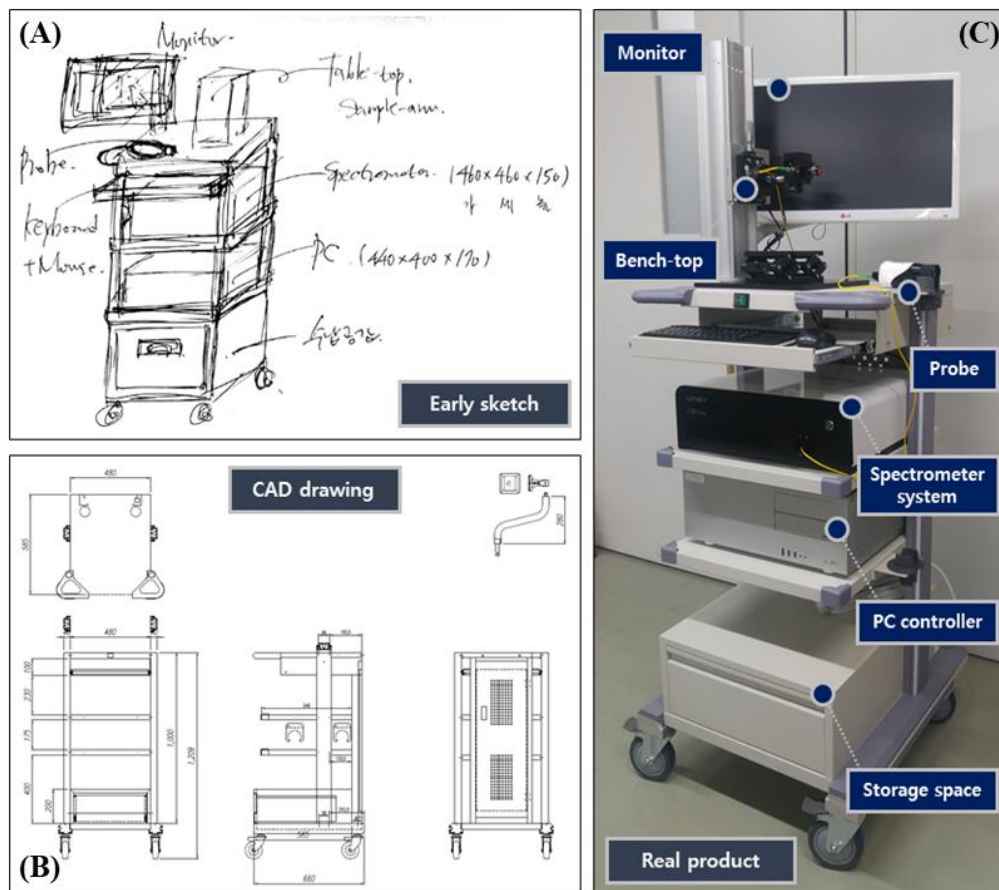
Figure 4-3. (A), (B) Sketch and 3D CAD drawing of the early concepts of portable OCT system with hand-held probe. (C) Portable OCT system after the completed manufacturing for human target researches.

To promote convenience in skin clinical research, we miniaturized and integrated OCT system and installed it in cart to establish portable OCT imaging system. Figure 4-3 presents the portable OCT imaging system which had 120 cm height and it was designed to provide comfortable standing work

for adults and consisted of an OCT system, computer as a control box, hand-held probe, bench-top imaging arm, and other delivery space for storing the necessary stuffs for clinical research. As a result, a variety of human studies were conducted, such as measurement of skin condition and quantitative indicator analysis of skin wrinkles in the human skin using the portable OCT system.
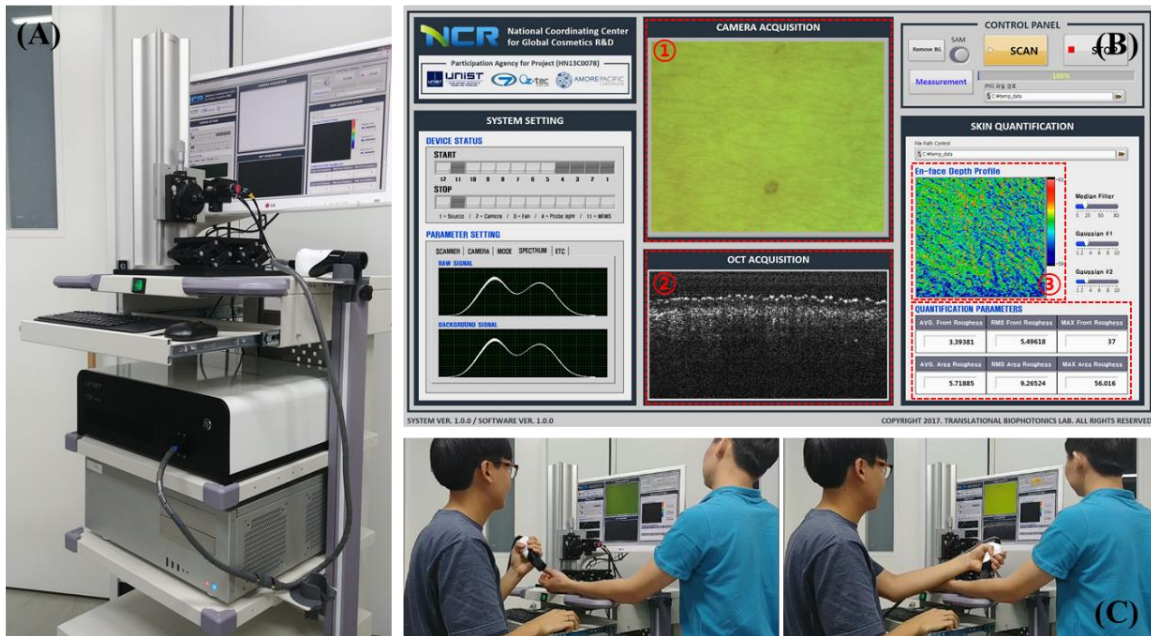
Figure 4-4. (A) Portable OCT system during the running of image acquisition, (B) Software window consisted of microscopic view, OCT cross-sectional image, and quantitative parameters of human skin conditions.

We developed a LabVIEW-based software for the operation of the hand-held based portable OCT system. The driving software provided both microscopic views using the miniaturized camera and cross-sectional image of OCT and we obtained quantitative parameters that the user desired for the human skin after the end of the three-dimensional image acquisition for the specified area. The operation process in detail consisted of 4 steps: (1) ROI searching with camera interface, (2) OCT image recording, (3) 3D data reconstruction, and (4) Quantitative analysis of skin conditions. We conducted clinical studies on the human body using a complete hand-held probe based portable OCT system and performed various quantitative analyses especially on the human skin.

4.2 Dynamic Monitoring and Quantification of Human Skin Conditions

4.2.1 Applications for Human Skin Monitoring

Here, we conducted various studies on human skin using the hand-held probe based portable OCT system. First, the 2D and 3D morphological information of human skin was acquired by the OCT imaging system and the skin layer segmentation algorithm was developed to analyze tissue structure quantitatively based on the cross-sectional skin images. We also measured the volume and depth of wrinkles based on OCT images to quantitatively analyze wrinkles in human skin. Furthermore, for comparison with the existing wrinkle analysis method, the skin roughness parameters were measured and the results of measurement under various conditions were analyzed with PROMOS which is a typical crease analysis device.

Feasibility study for measurement of skin condition
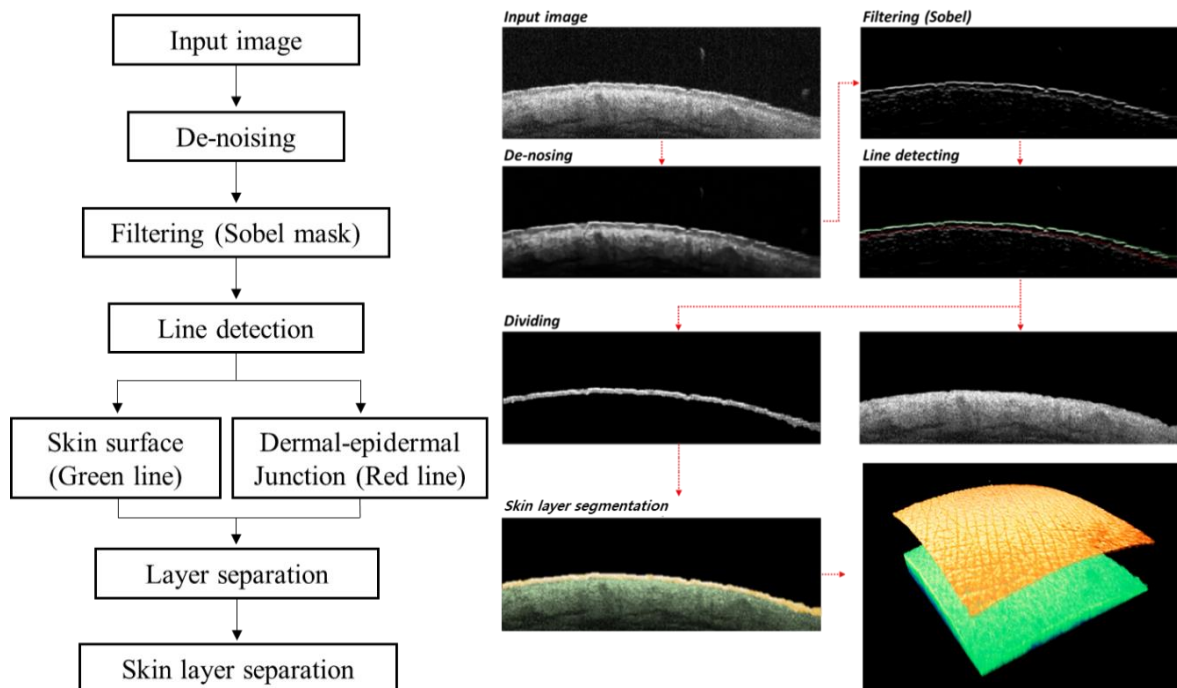
Figure 4-5. Image processing algorithm for layer segmentation of human skin based on OCT cross-sectional image. The green line indicates skin surface and the red line indicates the dermal-epidermal junction which is a boundary between an epidermal and dermal layer.

Figure 4-5 presents the image processing algorithm for skin layer segmentation based on the OCT cross-sectional image. First, the de-noising process was carried out through Gaussian filtering and intensity adjustment for accurate image processing. Then, we applied the Sobel mask and adjust the

parameters to detect the skin surface line and the dermal-epidermal junction line between the epidermal and the dermal layer. In Figure 4-5, the skin surface line was green, and the dermal-epidermal junction line was marked red. We segmented the dermal layer below the dermal-epidermal junction line and the space between the skin surface line and the dermal-epidermal junction line segmented into the epidermal layer. OCT images separated by the epidermis and dermis layers can be used for structural quantification, and three-dimensional reconstructed images found in Figure 4-5.
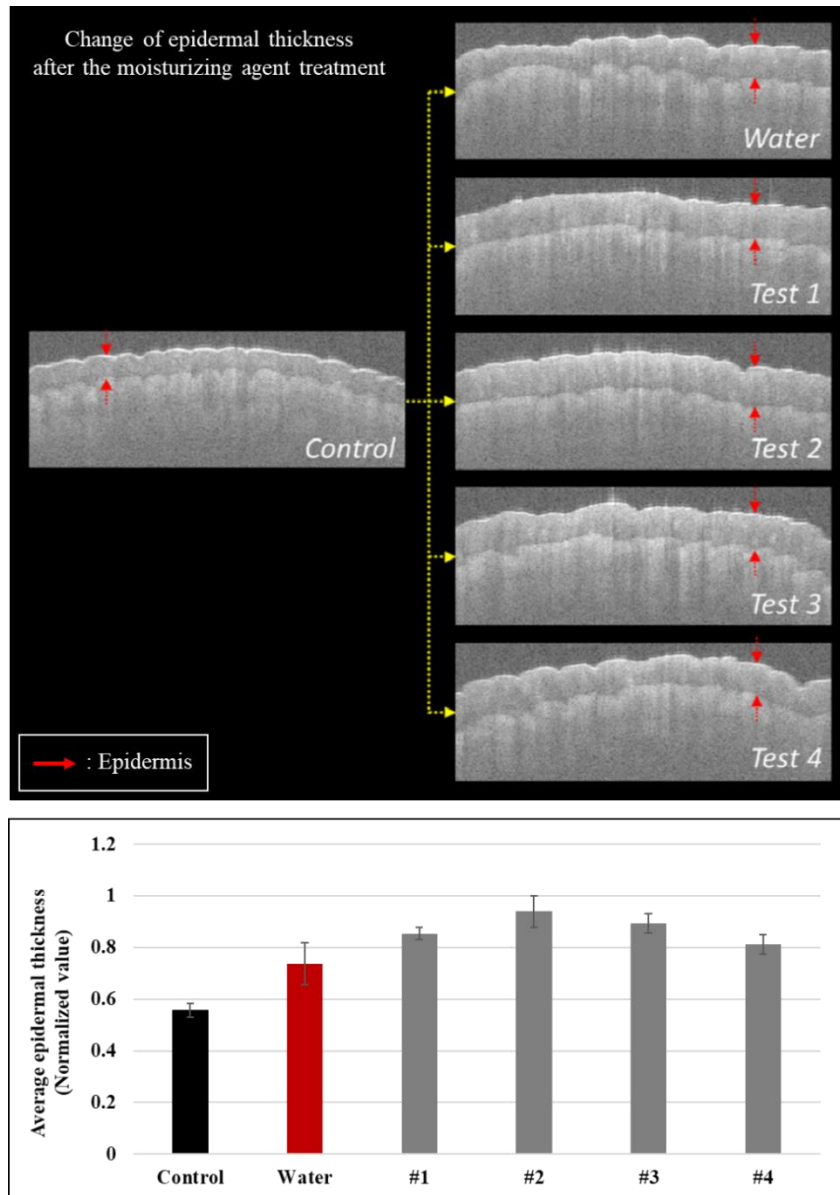
Figure 4-6. Quantitative measurement of the epidermal thickness changes on human skin after the treatment of moisturizing agents using the skin layer segmentation.

In Figure 4-6, we measured the epidermal thickness based on the layer segmentation algorithm to analyze how moisturizes affect structurally to the skin tissue on human skin. The volunteers washed

their palms clean and stood by at room temperature to prevent experimental errors from external factors. We acquired OCT images from the palm of volunteers with a control group that had no treatment, a water treatment group, and an experimental group that was treated by four different types of moisturizers. We measured the thickness of the skin epidermis for each group by using a layer segmentation algorithm to evaluate quantitatively the skin moisturizing ability and capability of the moisturizer. As a result, most moisturizers showed significant figures compared to control groups. For certain moisturizers, a change in the thickness of the epidermis was observed by nearly twice as much as the control. Based on these results, it is expected that it can be used as an indicator to assess the persistence of moisturizers by utilizing research to quantitatively observe and analyze the changes of epidermal thickness on the skin over time.
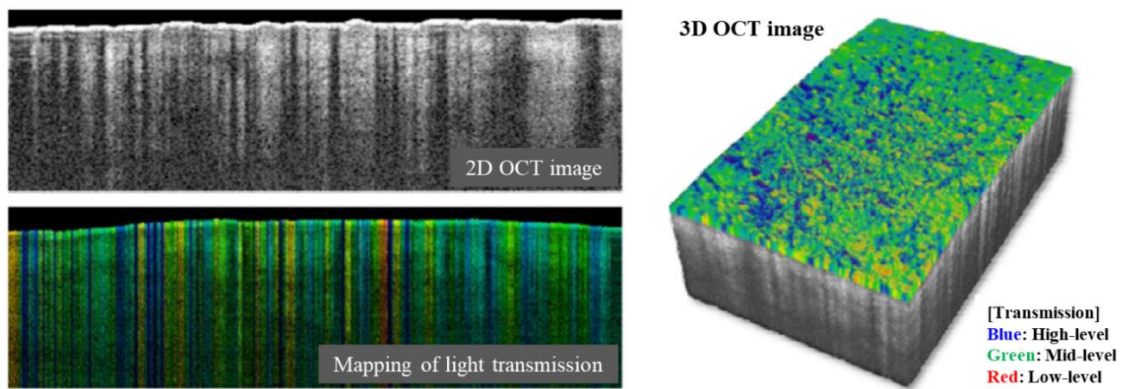
Figure 4-7. Quantitative analysis of the light transmission into the human skin after the treatment of powder-type cosmetics.

Figure 4-7 shows the quantitative analysis results of the light transmission into the human skin after treatment of powder-type cosmetics. OCT collected the returning light from the tissue to acquire the images which were transformed from interfered signals, so if a substance with different optical properties exists on the sample surface, it was obstructed by the transmission of light. In Figure 4-7, we used an obstruction with light transmission as an important information and used it as an indicator to evaluate the spread ability of cosmetics processed on the skin. Depending on the degree of transmission to the light in the longitudinal direction, color mapping can be used to check if the cosmetics are applied evenly. It is expected that it will be able to analyze quantitatively the permeability of light that changes according to the treatment of cosmetics or drugs and use it as a diverse indicator for further studies.

Quantitative analysis of volumetric information in human skin wrinkle

With the development of dermatological treatment and anti-aging process such as reducing wrinkles have attracted worldwide attention [59, 60]. Thus, skin care industry has dramatically grown up, and various anti-winkle treatment or products are available in the market. However, there has been no automatic platform for detecting and visualizing the wrinkles quantitatively. Prior work to approach skin study has been processed mainly by optical microscopy which is impossible to acquire three-dimensional skin geometry as well as three-dimensional structure of the wrinkle. Here, we utilized OCT imaging technique, which can visualize the 3D structure in a non-invasive manner with high-resolution. Also, we suggested a novel algorithm for automated quantification of skin wrinkles and delivered quantitative information of winkles in terms of depth and volume.
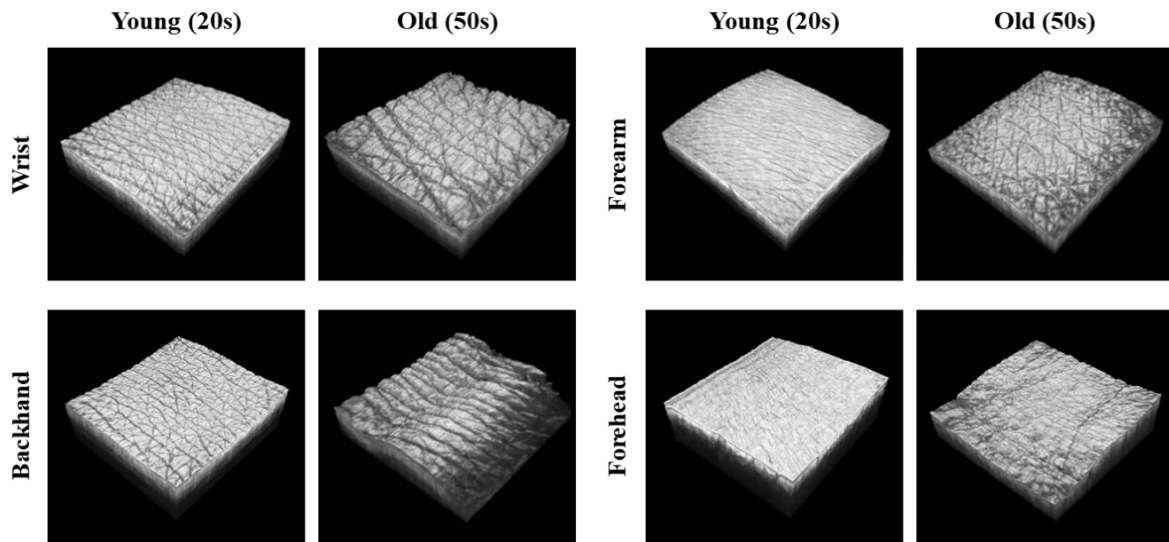
Figure 4-8. The image of human skin with wrinkles in 20s and 50s by different region acquired by OCT system. The skin image of 50s has clear shaped and deep wrinkle in comparison with skin image of 20s.

In Figure 4-8, we obtained OCT images from four different regions such as wrist, forearm, backhand, and forehead in the 20s and 50s for analysis of wrinkles by age and skin region. The volunteers cleaned each area of the skin with a cleanser and then shaved hairs in the area of 10 mm × 10 mm to acquire accurate quantitative results without hair artifacts that obstruct with precise OCT image acquisition. As shown in the 3D reconstructed OCT image, there was a noticeable difference in skin wrinkles between the 20s and 50s. We conducted a quantitative analysis of the depth and volume of skin wrinkles based on these image data-set.
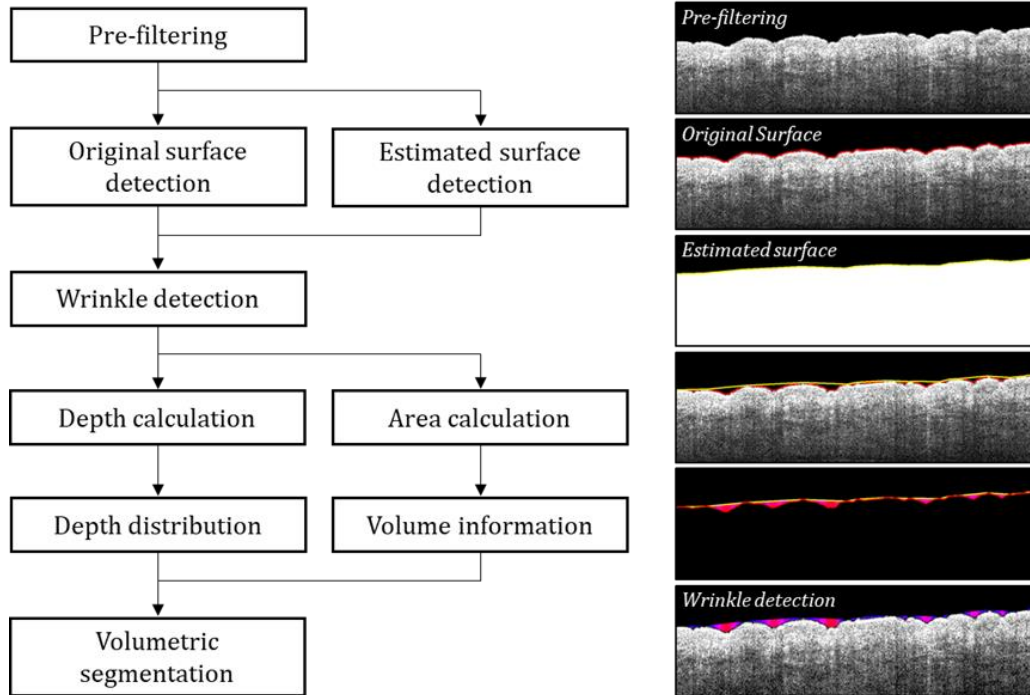
Figure 4-9. Image processing algorithm for automated quantification of human skin wrinkles. The algorithm quantified wrinkles by finding the original skin surface line with skin wrinkles and the estimated surface line that shows the tendency of the skin surface without skin wrinkles.

Figure 4-9 shows the image processing algorithm for automated quantification of human skin wrinkles. In the pre-filtering step, we removed a noise in a cross-sectional image and the image adjusted the intensity for clear and improved image quality. Here, we found the original 'skin surface line' (red line) with skin wrinkles and the 'estimated surface line' (yellow line) that shows the tendency of the skin curvature without skin wrinkles. We defined the area as the skin wrinkle between the two local maximal points on the surface line. This area is the space between the skin surface line and the estimated surface line, using the difference between these two lines to segment the winkle area. First, we acquired the skin surface line by detecting the dramatic change of signal intensity for all OCT A-lines in cross-sectional image. To find the estimated surface line, we found the local maximum points in the skin surface line and connected these points. Then, the area between the skin surface line and the estimated surface line was extracted and the wrinkle depth and volume of the human skin were calculated using this area. For the winkle depth, the number of pixels corresponding to the segmented winkle area was divided by the number of horizontal pixels in the cross-sectional OCT image and calculated by calibration of the actual size of longitudinal pixels. The average wrinkle depth within the 10 × 10 mm area was obtained by applying to a total of 500 cross-sectional images comprising the volumetric 3D skin data. The volume of wrinkles was calculated by voxel calibration for the horizontal, vertical, and height after obtaining all the number of pixels corresponding to the segmented winkle area in 500 cross-sectional images.

64
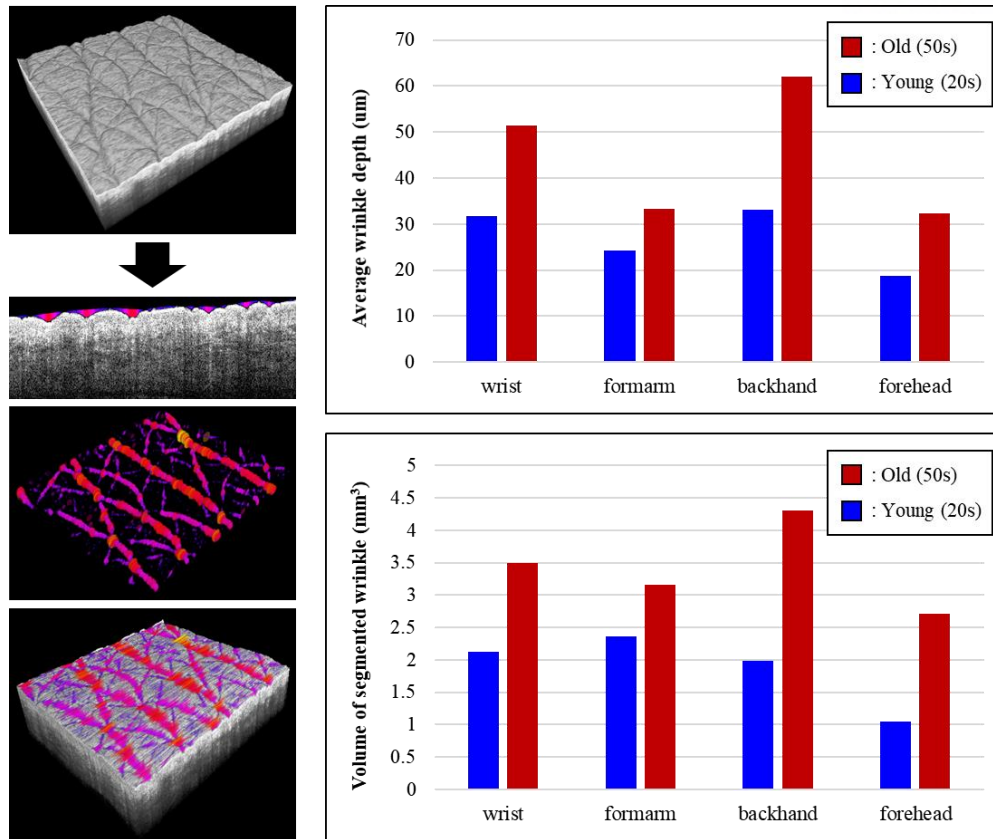
Figure 4-10. The results of quantitative analysis in human skin winkle with different age and skin regions. The depth and volume of wrinkles appeared to be high in the 50s in all skin regions, especially in the back of the hand and forehead. The result shows that the more exposed the skin region to the outside has a faster aging progress.

Figure 4-10 presents the results of the wrinkle depth and volume quantification by skin region in their 20s and 50s using the automated wrinkle quantification algorithm. The shape and pattern of segmented wrinkles extracted from cross-sectional OCT images was identified in three dimensions through image reconstruction. Also, the 3D reconstructed skin winkles were confirmed the correlation with 3D OCT image of the skin. As shown in the graph, the depth and volume of wrinkles appeared to be high in the 50s in all skin regions. In particular, the results of the back of the hand and forehead showed a significant difference in both the depth and volume of wrinkles compared to 20s. For the back of the hand and forehead, it is likely to be affected by external stimuli because of the longer exposure time of the skin area. These results supported previous research that shows that aging of skin, which is highly exposed to the external environment, progresses rapidly.

The OCT is powerful tool to be used in skin assessment capable of detecting and visualizing skin wrinkles. Also, our newly developed algorithm enabled to do quantification of targeted skin wrinkles in automatic way. It is expected that our study will play important role in performance test of anti-wrinkle products and dermatology-related study

4.2.2 Quantitative Evaluation of Human Skin Wrinkle Roughness

Research Motivation

The quantitative monitoring of skin topography is important in the field of cosmetics and dermatology. In particular, the in vivo and quantitative observation of skin is required for an accurate assessment of the effectiveness of an anti-aging product. To date, various techniques have been applied to monitor the morphological change in the skin. The use of skin replica or reprints with optical profilometry is the most common and simple way to observe skin topology [61, 62]. However, this method is inadequate when in vivo and fast feedback is required, because it is an indirect measurement and its outcome can be affected by air-bubbles [63]. Recently, advanced optical imaging modalities, such as reflectance confocal microscopy, fluorescence, and second-harmonic microscopy, were suggested to be promising tools for skin tissue analysis [64, 65]. In each of these techniques, pathologic changes in cellular, nuclear morphology, and melanin content were observed. Even though they provide high-contrast and cellular resolution imaging, the limitation in the field of view (FOV) remains a critical restriction for wrinkle investigation. One of the most commonly used imaging systems for skin measurement, PRIMOS (Canfield, US), was proposed as an objective tool in the cosmetics industry for studying skin topography and the volume of wrinkles. PRIMOS is a non-invasive, fast and direct measurement of the skin surface with high precision [66]. It has been successfully tested in scar assessment applications [66, 67]. However, PRIMOS has difficulty in providing accurate and reliable skin analysis because its results can vary according to orientation, motion artifacts, as well as a backscattering of the subject [67].

In this study, we demonstrate the potential of OCT for providing reliable and quantitative skin surface roughness. OCT has emerged as an appropriate tool for skin analysis with various advantages including cross-sectional, high-resolution, and real-time tissue imaging. The technical performance of OCT, such as volumetric and deep imaging capability, could avoid the critical drawback of PRIMOS such as the dependency of wrinkle orientation. To evaluate the performance of OCT for skin surface analysis, different types of skin phantoms were fabricated and measured. We utilized OCT to identify the effect of cosmetics as well as human skin topology for various aging groups and different skin regions. Skin surface roughness parameters were then derived from home-built image processing software and compared with one acquired from PRIMOS. Our results showed that skin surface geometry acquired from 3D OCT images was well quantified to complex wrinkle structure and robust to the angle of the subject. Since OCT enables to present quantitative skin topology and volumetric skin anatomy simultaneously, it would be a useful tool to deliver comprehensive and intuitive information in dynamic skin observations.

Roughness measurement method for quantitative analysis
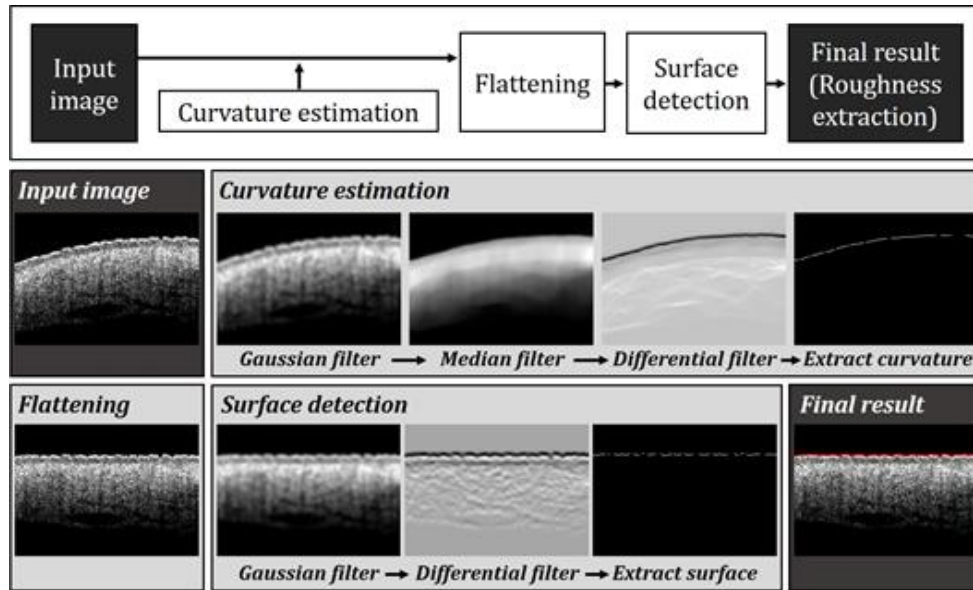
Figure 4-11. Procedure of automatic skin surface detection algorithm for quantitative analysis of skin roughness. The process includes 'Curvature estimation' and 'Surface detection after flattening'.

We developed an automatic segmentation algorithm to detect skin surface using MATLAB, as illustrated in Figure 4-11. The overall process of detecting the surface consists of two steps: (1) Curvature estimation and (2) Surface detection. In the curvature estimation step, we initially perform Gaussian filtering to diminish the effect of speckle-noise inherently present in optical coherence tomography systems. Next, using a median filter, a smoothed image with a diminished effect from noise is obtained while preserving the edges of the original image. We further apply a differential filter to emphasize the ideal surface boundary. As the final procedure in the curvature estimation step, the ideal surface is detected by finding the minimal intensity values from the results of the differential filter procedure. The determined ideal line serves as a reference for the second stage.

In the first step of the surface detection stage, we combine the result of reference ideal line and the coordinates of the original image to obtain normalized skin surface. The output is illustrated in the lower row of Figure 4-11 and labeled as flattening. Later, applying a Gaussian filter is necessary to acquire a noise-reduced image. Similarly, the real skin surface could be highlighted with a differential filter procedure. Finally, the expected skin surface is the result of local minimum operations for each pixel column. The last subfigure in the lower row presents the performance of the algorithm by overlaying the detected real surface onto the original normalized image. The reported computation technique was carefully examined on the image dataset consisting of more than 15,000 images and its acceptable efficiency to robustly identify the skin surface was confirmed on every input image.

Correlation study of skin wrinkle roughness
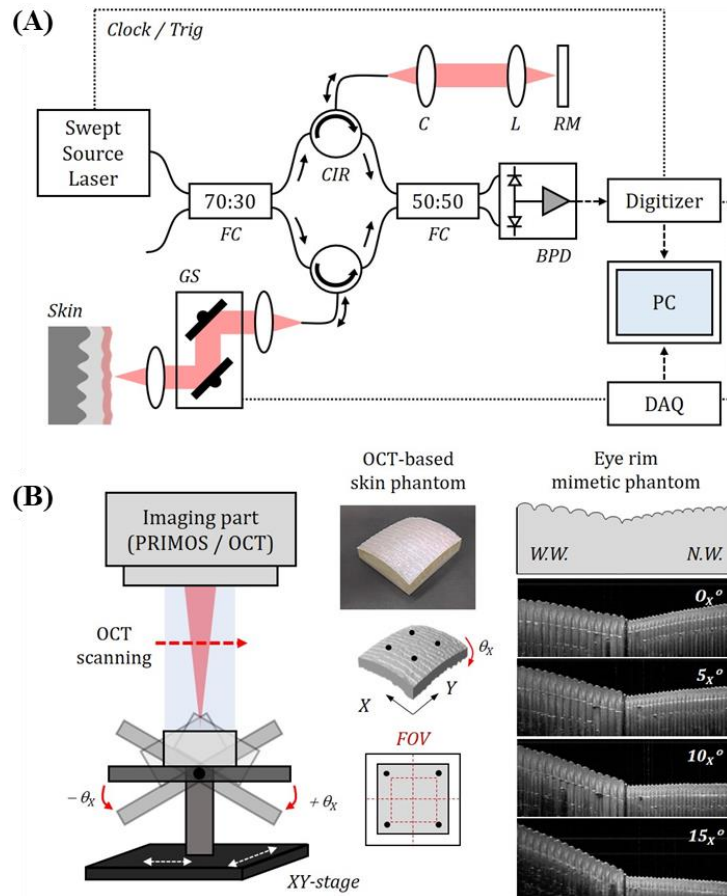
Figure 4-12. (A) Schematic diagram of the SS-OCT system used for scanning skin wrinkle. FC: fiber coupler, CIR: circulator, GS: galvanometer scanner, C: collimator, L: lens, RM: reference mirror, BPD: balanced photodetector; (B) Method for image acquisition by PRIMOS and OCT at different angular position using 3D printed skin phantoms.

The roughness analysis of phantom at a different angular position and skin structure was executed by using OCT and PRIMOS (GFM GmbH, Germany) [68]. To compare the feasibility between PRIMOS (GFM GmbH, Germany) and OCT, we used two kinds of skin phantoms, which were produced by a commercial 3D printer (Fortus 250mc, Stratasys Ltd.). The first phantom was fabricated for mimicking the eye rim structure which has different intervals of wrinkle patterns and surface curvatures; narrow winkle (N.W.), wide winkle (W.W.), as shown in Figure 4-12. Another phantom was made for implementing the real human skin structure. It was based on *in vivo* 3D OCT image of human skin which was converted to a stereo-lithography file for enabling 3D printing. The wrinkle morphology of constructed skin phantoms was confirmed and compared by the OCT and PRIMOS with angular variations. All the research procedures using human participants were carried out at Amorepacific Corp. R&D center in tight accordance with the Institutional Review Board for

Protection of Human Subjects in Research (IRB) approval (2017-1CR-N029S). Before the samples were examined by PRIMOS and OCT, the region of interest of the skin was washed by cleansing cream and exposed to a constant temperature and humidity in order to stabilize the experimental conditions. Human subjects for the skin test were divided into two groups. In the first group, 10 people were selected without considering the age or sex (35.3 ± 8.5 years old) and were imaged by SS-OCT according to a routine skin examination to investigate the changes of any wrinkles before and after applying the anti-aging cream (Figure 4-15). In the second group, we recruited a total of 10 human participants, who were then divided into two different groups by age. 5 people in a young age group (27.2 ± 1.2 years old) and 5 people in an old age group (55.4 ± 6.9 years old) were separately examined to analyze the changes of any wrinkles (Figure 4-16).

A1

	PRIMOS		OCT	
$0°$	1		1	
$\pm 10°$	1.040	0.950	1.006	0.981
$\pm 15°$	1.125	0.935	1.082	0.996
$\pm 20°$	1.120	0.953	1.084	0.995

A2

	PRIMOS		OCT	
$0°$	1		1	
$\pm 10°$	1.059	1.002	1.006	0.996
$\pm 15°$	1.116	1.026	1.078	1.015
$\pm 20°$	1.213	1.047	1.078	1.014

A3

	PRIMOS		OCT	
$0°$	1		1	
$\pm 10°$	1.194	0.979	1.004	1.014
$\pm 15°$	1.616	1.001	1.046	1.035
$\pm 20°$	1.372	1.049	1.056	1.040

B1

	PRIMOS		OCT	
$0°$	1		1	
$\pm 10°$	1.000	0.953	0.939	0.903
$\pm 15°$	1.064	0.851	0.972	0.882
$\pm 20°$	1.040	0.891	0.902	0.909

B2

	PRIMOS		OCT	
$0°$	1		1	
$\pm 10°$	1.042	0.971	0.954	0.910
$\pm 15°$	1.073	0.853	0.960	0.897
$\pm 20°$	1.067	0.894	0.916	0.906

B3

	PRIMOS		OCT	
$0°$	1		1	
$\pm 10°$	0.887	0.872	0.921	0.905
$\pm 15°$	1.238	0.728	0.995	0.931
$\pm 20°$	0.894	0.746	0.942	0.929

Figure 4-13. Comparison study of normalized roughness values between PRIMOS and OCT at varied angular positions -20°, -15°, -10°, 0°, +10°, +15°, +20° for (A) OCT-based skin phantom and (B) Eye rim mimetic phantom. (C) Surface topology of skin phantom achieved by PRIMOS and OCT.

OCT and PRIMOS devices were compared regarding imaging capability in terms of delivering consistency [68]. Specifically, an investigation into the ability to stay unaffected during sample fluctuation was conducted. We observed the presence of change in skin roughness results during the imaging angle variation for both devices. This evaluation is critical to perform since the experiment outcome should be consistent under different experimental circumstances. Moreover, subjects can accidentally twitch their skin region during examination, which is undesirable for acquiring quantitative results. In order to verify it, two kinds of 3D printed phantom fragments were created.

First phantom was fabricated to describe the real human skin structure which was based on in vivo 3D OCT image. The size of phantom was magnified having 4 cm × 4 cm, which formed large-scale of wrinkle over real dimension. We imaged this phantom using OCT and PRIMOS varying the angular positions from - 20° to 20°. The values of skin roughness were then extracted by home-built software using surface flattening and software included in the PRIMOS package, respectively. Figure 4-13(A) presents results of comparison study at 7 different angle positions for OCT-based skin phantom. As can observe from Figure 4-13, the standard deviations at the left column of PRIMOS was higher than one in the right column of OCT. This outcome indicates that skin surface analysis with OCT offers more consistent performance despite the angle variation of subject. This is because that OCT measurement includes the surface tracking and flattening algorithm which is based on natural curvature extracting from volumetric and deep skin OCT imaging. On the other hands, PRIMOS uses only shallow surface profile which may induce erroneous results. This is the reason why PRIMOS results has more fluctuation at higher angle, 20° over 0° position.

Another phantom was artificially designed and constructed as mimic of eye rim structure having narrow and wide wrinkle patterns within tight intervals. Eye rim mimicking phantom was imaged by OCT and PRIMOS in same condition and procedure as described above, and its outcome was shown as Figure 4-13(B). Similar to the results of previous phantom study, OCT measurement has more reliability over one acquired from PRIMOS. In order to observe the compact and periodic structure of wrinkle, imaging device requires high resolution which was evaluated as presented in Figure 4-13(C). Topologic image of OCT is well defined periodic structures in two different wrinkle structures. On the contrary, topology achieved by PRIMOS visualizes unclear distinction and irregular pattern of surface which is more severe in high frequency wrinkle network. Through experiments with two phantoms we identified that OCT is not only a feasible device for investigating skin surface, but could also exceed PRIMOS in terms of resolution, accuracy and consistency under position variable conditions of subjects.

Quantitative analysis and evaluation of skin wrinkle roughness

Previously, we utilized the 3D printed skin phantom to validate the wrinkle analysis capability of OCT in comparison with PRIMOS about skin roughness parameters. Here, we analyzed the wrinkle roughness on the human skin using OCT based on previous results. Figure 4-14 presents the comparison of correlation between PRIOMS and OCT imaging in the young and old age groups at the different skin regions.
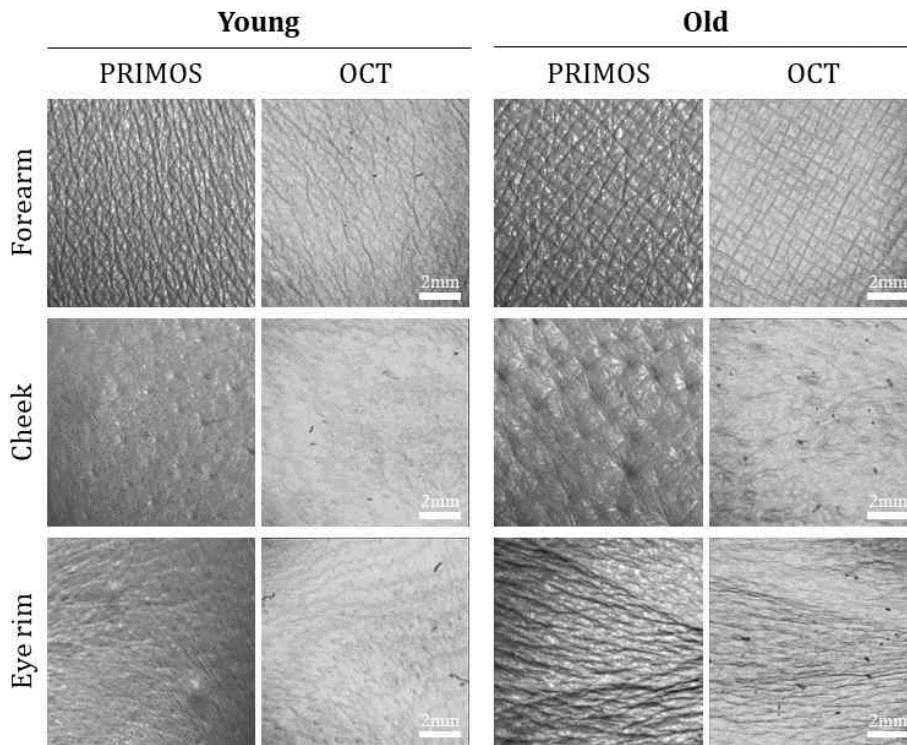
Figure 4-14. Correlation between PRIMOS and OCT imaging of the young and old age groups in a different skin regions.

The influence of cosmetic products on changes in skin surface roughness was evaluated using OCT. Through this experiment, we demonstrate that the effectiveness of optimal care anti-aging ointments and various skincare treatment methods can be assessed. OCT could also become an additional tool to monitor and quantitatively compare the effectiveness of different treatment techniques. It is expected that our quantitative outcome from the proposed algorithm will provide users with useful information with regards to determining the most effective cosmetic products and identifying appropriate customized skin treatment for each customer.
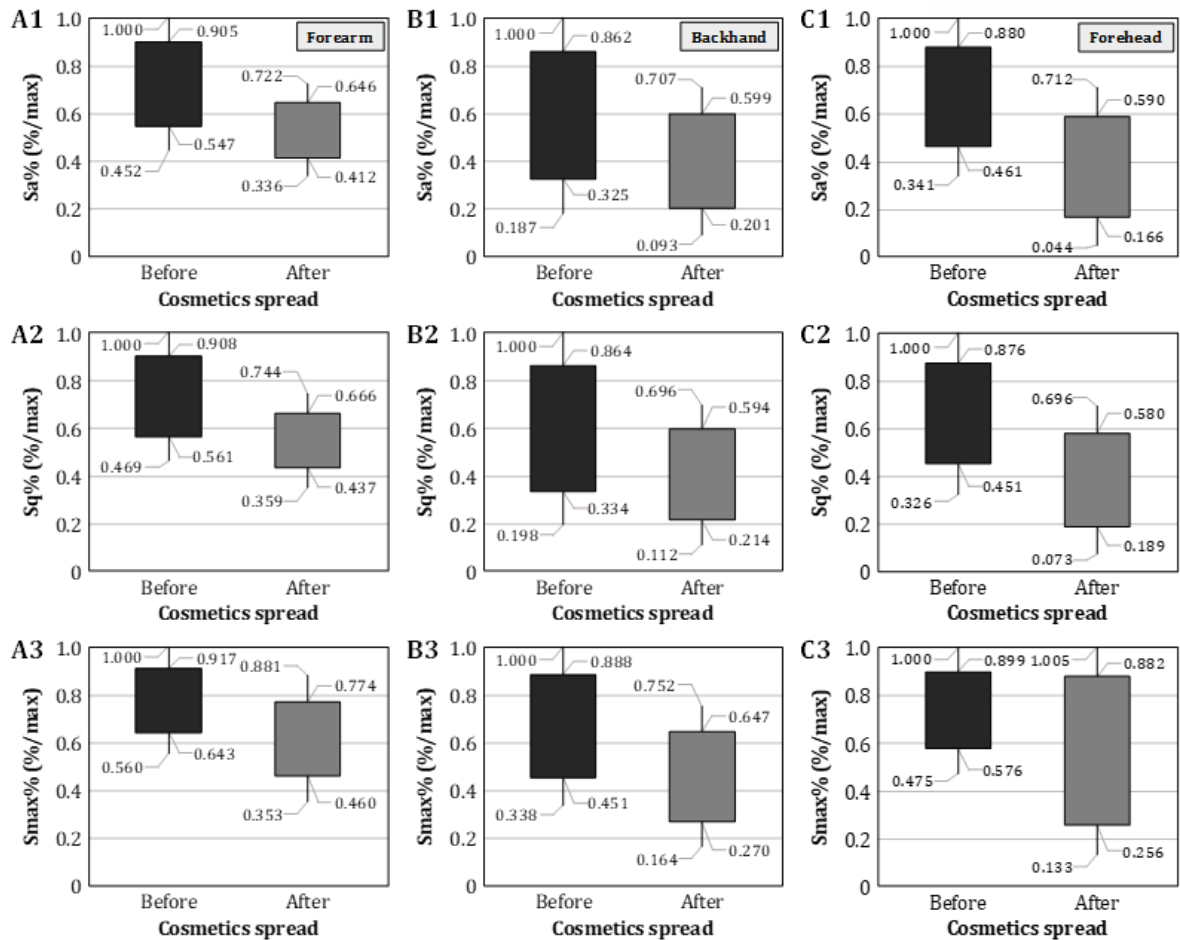
Figure 4-15. Skin surface roughness changes before and after applying cosmetics for (A) forearm, (B) backhand, and (C) forehead accordingly.

In this experiment, ten subjects of mixed age groups were engaged. For each subject, different regions of the body such as the forehead, forearm, and backhand were determined as our region of interest (ROI). We closely investigated skin surface roughness parameters before and after each application of an anti-aging product. Our hypothesis was that the subject's skin should get smoother after treatment, showing a decrease in roughness values. The numerical values of the conducted experiment are gathered in Figure 4-15. In Figure 4-15, each of the three columns represents roughness parameters. We examined the average, RMS and total profile skin roughness. The rows in the figures represent the skin region of interest: forehead, forearm, and backhand accordingly. The values are normalized based on the initial skin roughness state before treatment, depicted with black vertical bar graphs on the left. In contrast, the gray bar to the right represents the roughness values after the specified treatment application. From Figure 4-15, the gray bars are lower than those in black. The effect implies that after applying cosmetics there is a tendency for the skin roughness value to decline. This validates our hypothesis and characterizes OCT as viable skin analysis and treatment monitoring tool.

Table 4-1. Roughness values for young and old age groups

Age group	Skin region	Average	RMS	Maximal
Young	Forearm	0.49 ± 0.22	0.98 ± 0.30	5.70 ± 0.43
	Cheek	1.02 ± 0.23	2.08 ± 0.40	10.10 ± 2.33
	Eye rim	1.22 ± 0.17	2.34 ± 0.34	10.82 ± 2.27
Old	Forearm	0.78 ± 0.28	1.58 ± 0.67	8.05 ± 2.66
	Cheek	2.10 ± 1.07	4.23 ± 1.94	13.33 ± 3.08
	Eye rim	2.71 ± 0.82	5.22 ± 1.53	14.94 ± 1.32
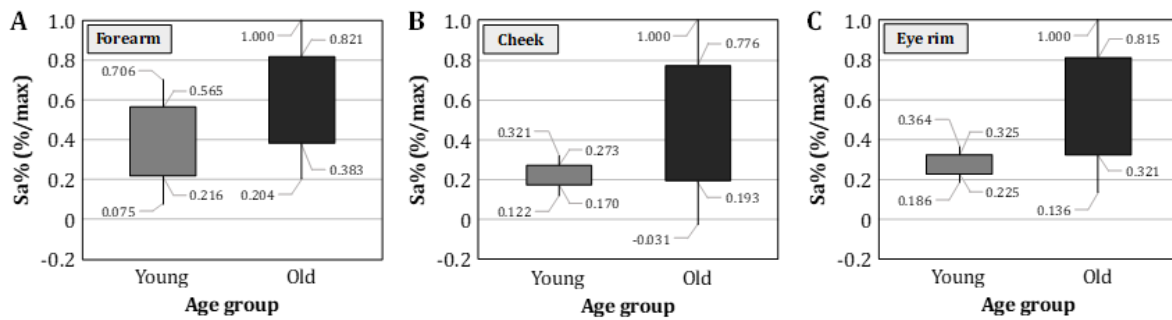
Figure 4-16. Distribution of average roughness values in young and old age group subjects for three skin regions, (A) Forearm, (B) Cheek, and (C) Eye rim.

In the previous experiment, the application of SS-OCT in skin treatment monitoring was demonstrated. It found that the results corresponded well with our initial hypothesis. In this setup, we investigated the influence of the aging process on skin surfaces. The change in roughness values and their correlation with subject age was investigated. Similar studies may be helpful to understand the aging process and the various parameters affecting it. 10 human subjects of two age groups were involved. The first five subjects representing the younger generation (mean age: 27) and the other five subjects for the older generation (mean age: 55) were considered. The three-dimensional OCT images acquired in three different skin regions. The same imaging procedure and experiment protocol were repeated for the cheek, eye rim and forearm skin regions.

Table 4-1 represents the numerical values of the average, RMS and maximal profile roughness parameters. They are grouped according to their age group and the skin region being investigated. The numerical results from Table 4-1 suggest there are higher values in older subjects. In contrast, the younger representatives have reduced numbers for the same parameters. The outcome states the presence of a positive correlation between subject age and roughness parameters. Through this experiment, the influence of the aging process on skin surface roughness values was confirmed.

Moreover, roughness values among various skin regions were compared. Based on the collected results, we present our findings in Figure 4-16. It suggests that there is the least notable difference between young and old age groups in the bar chart which corresponds to the forearm. On the other hand, looking at the cheek and eye rim there is the greatest difference in the value of the surface roughness distribution. This effect indicates that the forearm is influenced least, while cheek and eye rim are highly affected by aging out of three investigated skin regions.

Discussions and conclusions

PRIMOS is a powerful device capable of performing noninvasive, fast and direct measurement of the skin surface, and rich functionality included in its software package. However, it has a restriction to acquire information while preserving both high resolution and reliability despite its popularity. In this study, we investigated the potential of OCT for quantitative monitoring of skin surface roughness and presented a comparison of measurements with the PRIMOS [68]. OCT visualized morphologic variation of the skin surface in a three-dimensional and high-resolution approach. We found that OCT combined with flattening image processing was robust to evaluate quantitative skin roughness while reducing image artifacts such as dependence onto wrinkle orientation or motion artifacts. Through our experiments, we also confirmed that OCT could deliver comprehensive and intuitive information of morphologic changes in the skin and roughness parameters for monitoring skin treatment and the influence of the further skin aging study.

In this manuscript, we mainly focused on quantitative estimations of actual roughness parameter values from detected surface topography. Advances in technology such as cubic meter volume OCT would make it possible to improve the image quality as well as applicability [69]. The implementation of better OCT contrast and imaging depth would help to accurately quantify the epidermal thickness properties as well. When the epidermal layer is observed, a new algorithm needs to be proposed for the quantification of the roughness parameters in the dermal-epidermal junction [70]. The correlation of the dermal-epidermal junction roughness with the aging process is a relevant subject since inner layers are less affected by the extrinsic environmental factor. Finally, the integration of high-speed OCT could make the procedure more time-efficient, opening new opportunities to study skin in real-time [71].

We demonstrated the potential of OCT-based on flattening image processing for monitoring quantitative skin roughness. Experimental results of the phantom study showed that OCT is reliable to the angle of the subject and compact wrinkle structure compared to one acquired from PRIMOS. We also investigated that OCT is adequate for monitoring wrinkle morphology changes in vivo. Through our results, we found that OCT would be a useful tool to deliver comprehensive and intuitive information in dynamic skin observations since OCT enables observing quantitative skin topology

and volumetric skin anatomy simultaneously. The integration of our tool with advanced OCT technology, which includes a hand-held probe and volumetric OCT system would create an ideal opportunity to serve the routine process in real-world dermatology or to enter the cosmetics market.

CHAPTER 5. Imaging Guided Three-dimensional Modeling for Tissue Fabrication

In this chapter, we applied previous results to the tissue fabrication process based on the observation and quantitative analysis studies of biological tissues using the optical imaging modality. We performed a pilot study to fabricate an engineered tissue which is mimicked human tissue or imitative of native tissue structure based on the structural and morphological information of the tissue obtained from the OCT imaging. It is very important to fabricate the engineered skin close to the various properties of native tissue for obtaining outcomes similar to clinical trials as well as fast and stable adaptation in the future transplant process.

5.1 Wrinkle Mimicked Engineered Skin Model

For the study of skin anti-aging with high clinical efficacy, it is important to develop a new model of engineered skin with a form of wrinkles and curvature similar to actual skin, not the current flat and simple dermal-epidermal structure. In this study, we observed and analyzed human skin using OCT, and based on these data, we conducted to develop the wrinkled engineered skin by fabrication of a wrinkle patterned mold with a 3D printing technique. The wrinkle mimicked engineered skin was fabricated by forming collagen with winkle patterned mold and going through the formation of epidermal layers. Observing the completely cultured winkle mimicked engineered skin through OCT and tissue staining, we confirmed that a pattern similar to the shape of the wrinkle was forming stably on the surface of engineered skin. In addition, for verification of human correlations of manufactured wrinkled engineered skin, we observed that the form of wrinkles or curvature became improved after a treatment of retinoic acids on the engineered skin. In this study, we have established a basic technology for the manufacture of new engineered skin models with a desired shape of wrinkles and curvature. It is expected that if the model is verified and established through further studies in the future, it will play an important role as a new model for skin anti-aging studies.

5.1.1 Fabrication Protocol for Winkle Mimicked Engineered Skin
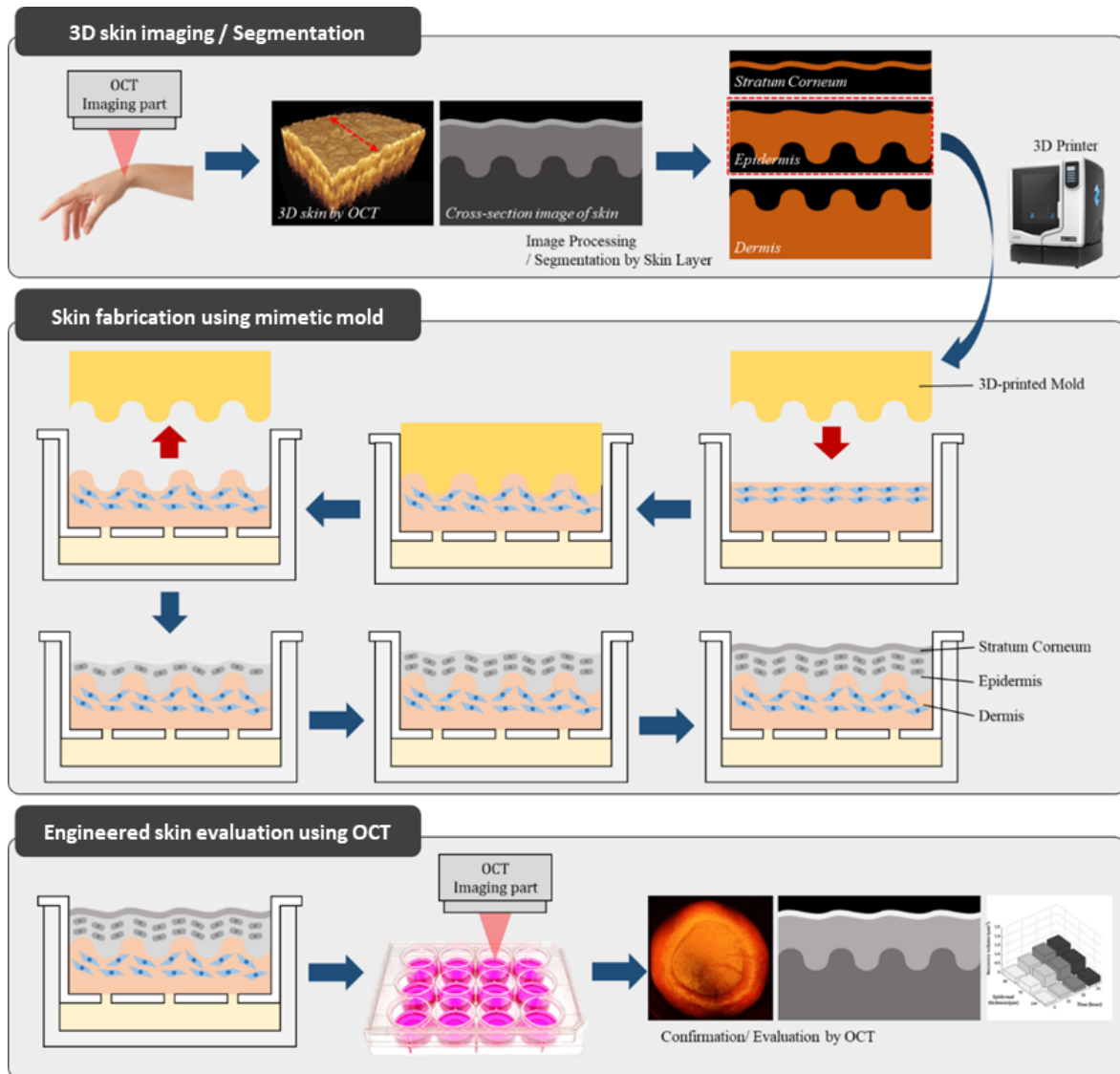
Figure 5-1. Fabrication protocol for winkle mimicked engineered skin for the study of skin anti-aging with high clinical efficacy. We aimed to utilize the 3D printer to fabricate molds with wrinkles patterns and it applied to the cultivation process of engineered skin to create winkle mimicked engineered skin with winkled and curved surface.

   Figure 5-1 presents the fabrication protocol of the engineered skin that mimicked the winkle on the native human skin. The concept of this study was to create the wrinkle mimicked engineered skin by shaping a dermal layer using a 3D printed mold mimicked skin wrinkle or curvature. Then, the keratinocyte was seeded and cultivated on the dermis layer where the wrinkle pattern was formed to obtain the completed engineered skin.

5.1.2 Evaluation of Wrinkled Engineered Skin Model
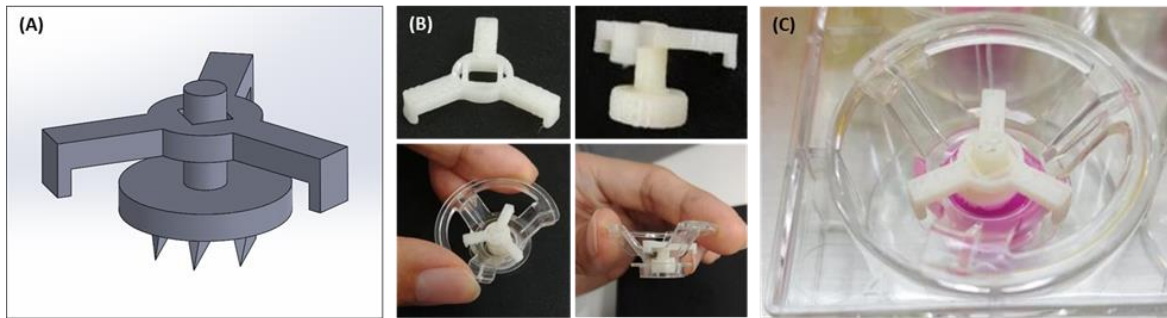
Figure 5-2. Feature of the wrinkle patterned mold fabricated by 3D printing technique. (A) 3D design of the mold with winkle pattern, (B) 3D printed mold and holder for winkle forming on the collagen based dermal layer, (C) Winkle forming during a formation process of dermis layer.

In Figure 5-2, we fabricated the wrinkle patterned mold to develop the wrinkle mimicked engineered skin model using a 3D printing technique. The winkle patterned mold was made of ABS (Acrylonitrile butadiene styrene polymer) which is one of biomaterial materials using the 3D printer (Fortus 250mc, Stratasys, Ltd.), and the mold consisted of wrinkle patterned body with different gap and size of patterns for shaping the dermis layer of the engineered skin and a cradle for standing in the transwell (Transwell®, Corning, Inc.) during the cultivation of engineered skin. In the early stages of the study, the wrinkle patterned mold was constructed with a minute pattern measuring several hundred micrometers, however the shape was improved to a copy with a certain interval of triangular structure for simulation close to the actual human skin wrinkle.
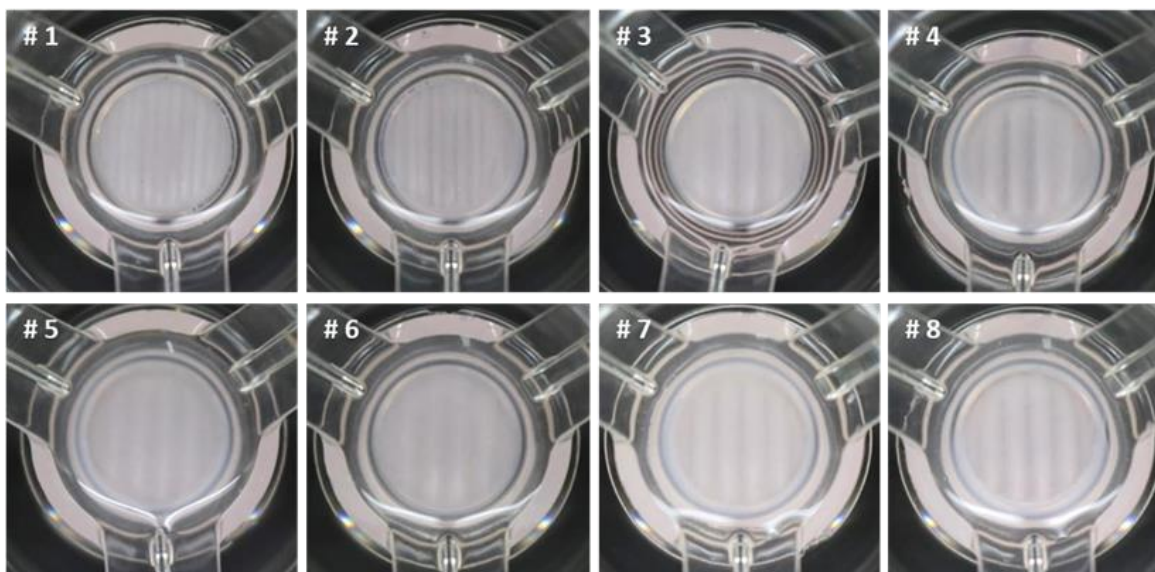
Figure 5-3. Wrinkle forming results on collagen based dermal layer by 3D printed winkle patterned mold with various size and gap of the winkle patterns.

In Figure 5-3, we confirmed the dermal layer was shaped into desired winkled pattern during the incubation of engineered skin by applying the wrinkle mimicked mold to the mixture of collagen and fibroblast cells. We confirmed that the wrinkle forming on dermis layer is possible according to the size and gap of patterns we have adjusted.
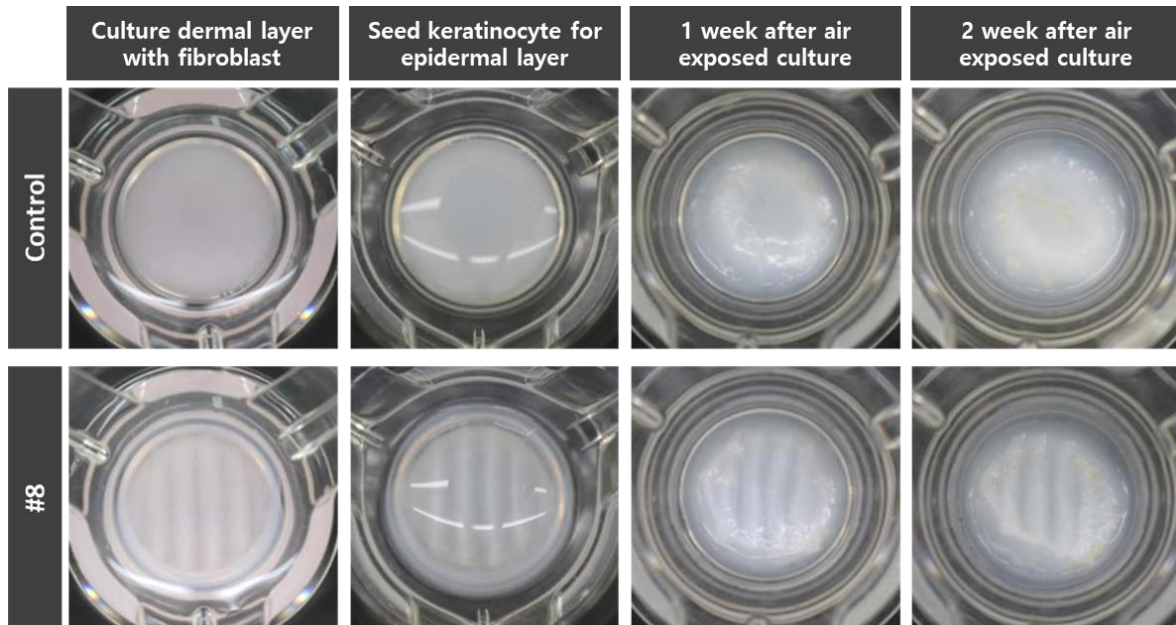
Figure 5-4. The tissue culturing process of engineered skin fabricated by traditional method as a control and winkle mimicked engineered skin using winkle patterned mold.

Figure 5-4 presents incubation process of engineered skin fabricated by traditional methods as a control group and wrinkle mimicked engineered skin with wrinkles pattern. The fabrication process of the wrinkled engineered skin was carried out in the order of (1) wrinkle pattern formation on the dermal layer, (2) dermal layer cultivation, and (3) epidermis layer cultivation. A mixture of collagen (Nutragen, Advanced Biomatrix, Inc.) and fibroblast cells (HDFn, Thermo Fisher Scientific Korea, Ltd.) was immersed in the transwell and a wrinkle patterned mold was cradled to the transwell to form the desired form of wrinkle pattern at the top of the dermal layer. For wrinkle formation on the dermis, the mixture was solidified in the incubator for about two hours and the wrinkle patterned mold was removed. The keratinocyte cells (HEKn, Thermo Fisher Scientific Korea, Ltd.) were seeded on stabilized dermis layer by adding fibroblast culture media and cultivated in the keratinocyte culture medium. Then, the wrinkle mimicked engineered skin was created by forming epidermal layers by incubating it in the air exposure for 14 days. We could visually observe the wrinkle pattern made by the 3D printed mold in the completely fabricated engineered skin.

Microscopic image	3D OCT image	Projection OCT image	2D OCT image
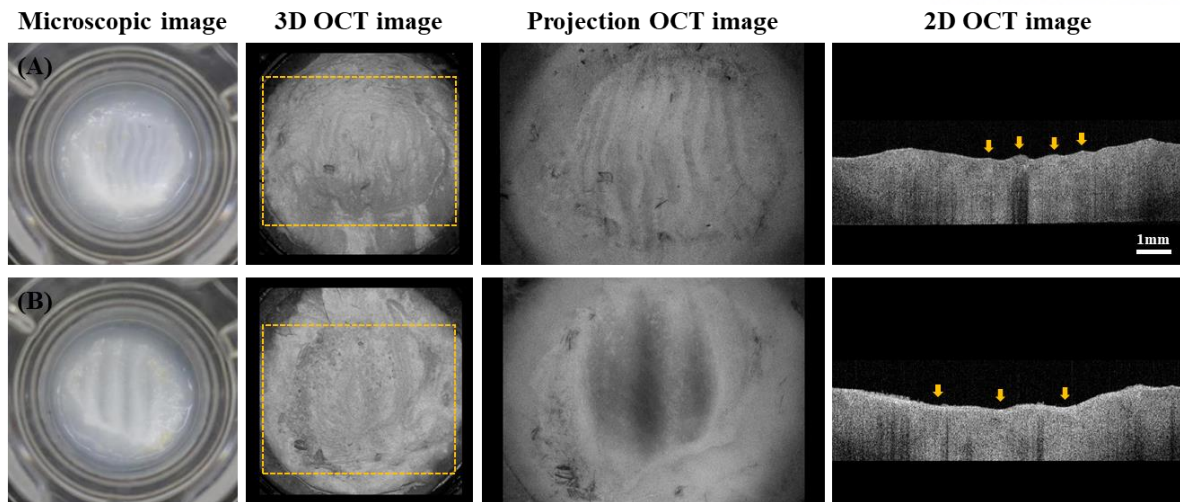
Figure 5-5. Completely cultured wrinkle mimicked engineered skin fabricated by different gap of winkle patterns in winkle patterned mold manufactured by 3D printer.
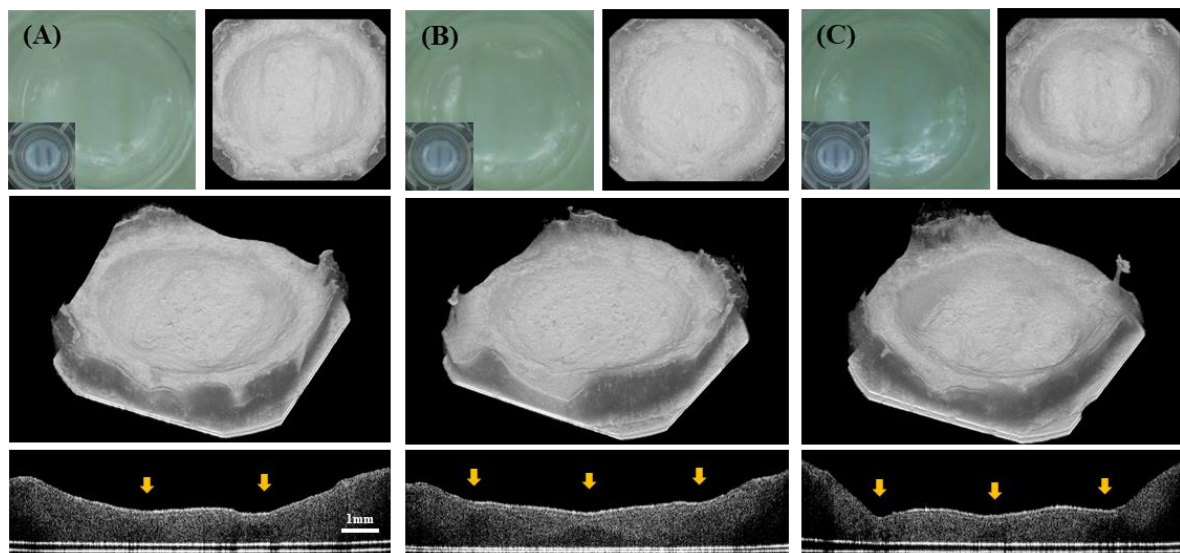
Figure 5-6. Evaluation of the winkle mimicked engineered skin using the OCT imaging modality.

In Figure 5-5 and Figure 5-6, the results of wrinkle formation according to the pattern of the wrinkle patterned 3D printed mold are verified using OCT imaging modality for evaluation of the developed wrinkle mimicked engineered skin. OCT provides non-invasive high-resolution cross-sectional and volumetric images of tissue morphologies in real-time using the near-infrared light source and it is suitable for continuous monitoring and evaluation of engineered skin. As shown in Figure 5-6, the wrinkled engineered skins were imaged in 2D and 3D images using OCT and the wrinkle formation on the engineered skin was evaluated. Through repeated experiments, we were able to form wrinkles stably on the engineered skin, and the structural verification using OCT provided more intuitive and quantitative information than conventional histopathological methods or other imaging devices.

However, as an engineered skin culture progressed, it was confirmed that the contraction of tissue and the influence of keratinocyte on the epidermis caused morphological and structural changes in the wrinkle pattern made in the dermis layer.
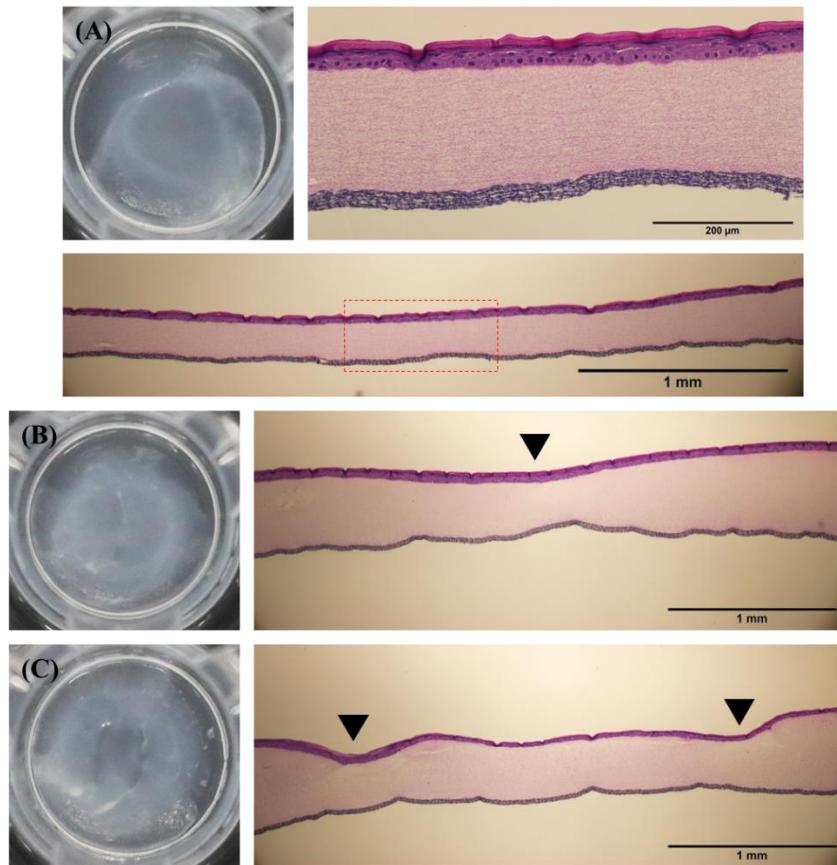
Figure 5-7. Evaluation of the winkle mimicked engineered skin using the H&E staining in comparison with the native engineered skin without the shaping of winkle patterns. (A) Native engineered skin which has epidermal and dermal layer without winkle patterns. (B, C) Wrinkle mimicked engineered skin applied by 3D printed mold which has (B) a single triangular edge and (C) two triangular edges.

In Figure 5-7, we applied the H&E tissue staining technique which is most commonly used for the analysis of biological tissues to verify winkles or curvature patterns shaped on the winkle mimicked engineered skin. We confirmed that the native engineered skin, which has no pattern forming on the dermal layer, had a flat surface in tissue staining images under the microscope.

Figure 5-8 shows the effects after a treatment of the retinoic acid, known as antioxidants, to verify the human correlations of the developed wrinkled engineered skin using OCT imaging. The wrinkle mimicked engineered skin immediately after incubation had clear curvature on the surface, whereas in the case of wrinkled engineered skin treated with retinoic acid, the flexion tendency on the surface has been observed. Through these results, we confirmed that the fabrication technique of wrinkled

engineered skin and verification protocol of this study can be used in the various tissue engineering studies such as screening of anti-aging materials as well as the optimization of the engineered skin of the wrinkles in the future.
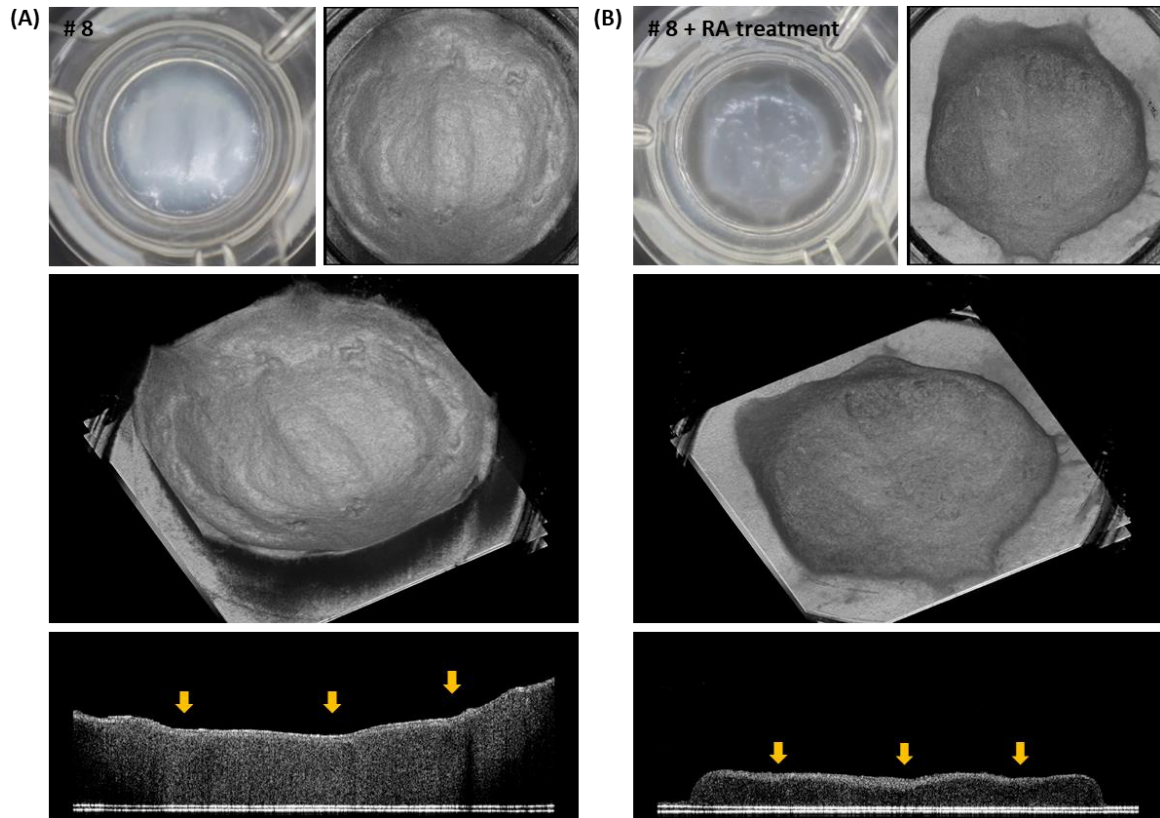
Figure 5-8. The winkle mimicked engineered skin before and after treatment of retinoic acid (RA) for verifying a correlation with human skin.

In this study, we could observe the possibility of mimicking wrinkles or curvature on the engineered skin with dermal layer shaping techniques using 3D printed patterned molds. However, most of the processes from the shape of mold pattern to engineered skin culture were related to the formation of wrinkles and curvature, which required very careful adjustment. First, we tried to create wrinkles and curvature on the engineered skin based on information of wrinkle segmentation results from OCT image, however, we had difficulty in forming wrinkles on engineered skin with tiny wrinkle patterns. Therefore, we manufactured various sizes of serrated molds for the formation of wrinkle patterns on the engineered skin. We established experimental conditions in which a certain type of wrinkle can be formed through multiple iterations, and we intend to establish and utilize the desired form and the model of wrinkles with repeatability and reproducibility through further studies. Since there are no skin equivalent models to study wrinkles at the cell level to date, we expect that the future optimization and verification will play a very important role in skin anti-aging research and development.

5.2 OCT Imaging Guided Engineered Cornea Fabrication

Cornea is a significant organ to provide eyesight whose function directly connected to life and it is difficult to replace when it has critical damage such as scar or opacity. The clear needs for engineered cornea had emerged because of the lack of donated cornea for transplantation, however, there are still a lot of hurdles to fabricate engineered cornea which mimics the native cornea structurally and functionally [72, 73]. For the engineered cornea, there are needs for further investigation to delineate structural characteristics, because it is important issue to mimic native tissue. We designed the protocol for personalized engineered cornea from imaging to fabrication using the optical coherence tomography (OCT) and a 3D printing technique.

Here, we introduced novel tissue fabrication protocol for personalized engineered cornea using optical coherence tomography (OCT) with 3D printed mold mimicked the native cornea structure. First, OCT scanned anterior segment of porcine eyes to acquire three-dimensional information of the whole cornea structure. We designed operation area for the cornea transplantation with measurement of personalized factors such as diameter, thickness, and curvature on OCT images. The surgical area to be removed by lamellar keratoplasty segmented using image processing and it converted to 3D modeling data for building a mold. The 3D modeled cornea utilized for reverse-designing to create 3D printed mold which can print out engineered cornea. We tried to fabricate engineered cornea using various biocompatible materials to mimic the physical and optical characteristics of the native cornea as well as its structure. It is expected that the new fabrication platform based on OCT imaging and 3D printing would be promising tool to provide not only engineered cornea, but also various personalized tissues.

5.2.1 Fabrication Protocol for Personalized Engineered Cornea
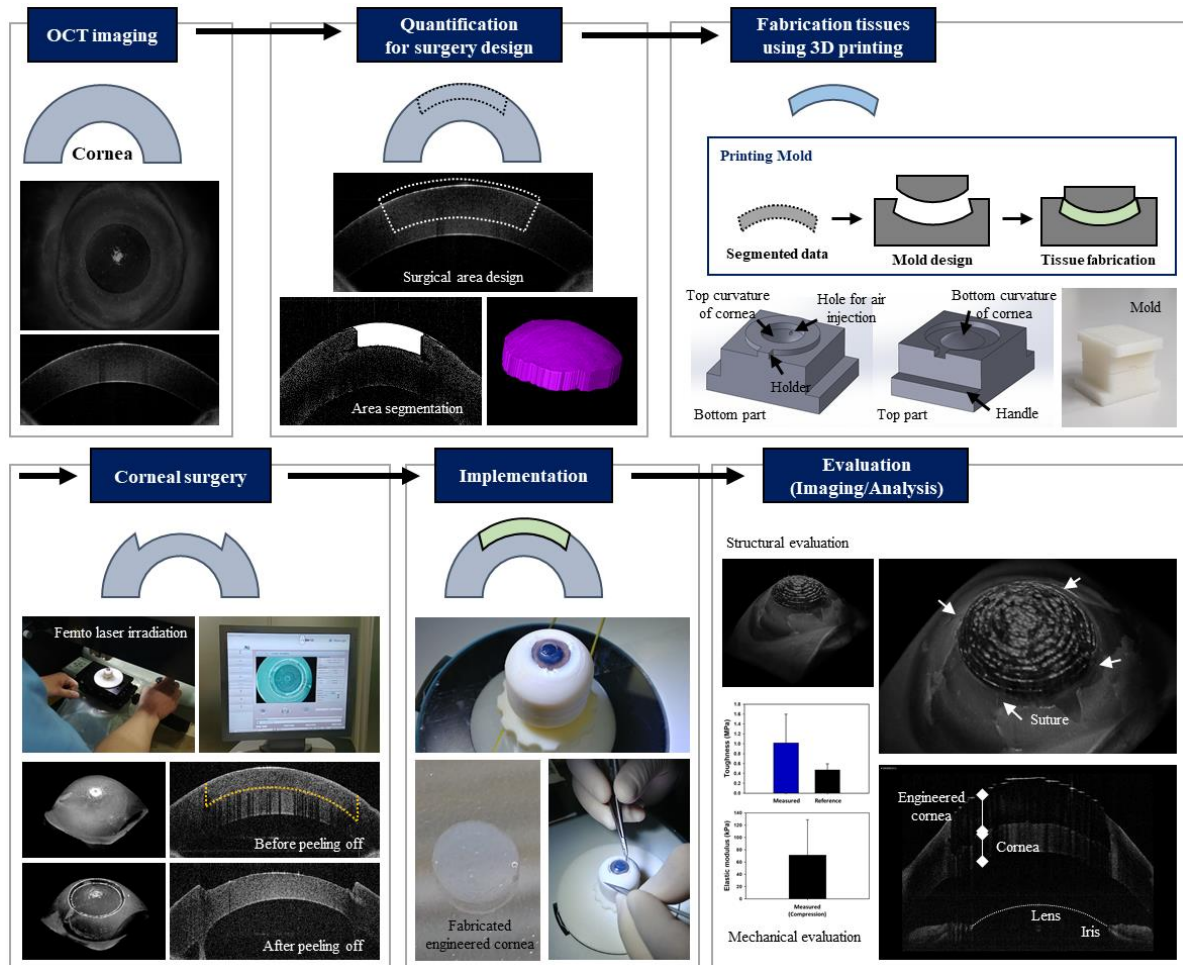
Figure 5-9. Fabrication protocol for the personalized engineered cornea for the pilot study of corneal transplantation.

Figure 5-9 presents the concept of fabrication protocol for personalized engineered cornea for corneal transplantation. We acquired a three-dimensional OCT image of whole cornea structure in the porcine eye and set the surgical area for the cornea transplantation with measurement of diameter and thickness around the center point. We reconstructed the 3D structure of the surgical area to be peeled using the image processing based on previously acquired information. The 3D structural information was reverse-engineered to create a 3D printed mold for the fabrication of engineered cornea. Engineered cornea was fabricated with various kinds of materials that has similar mechanical and optical properties to the native cornea. It is conducting the feasibility studies to find candidate materials that are most suitable for fabrication of engineered cornea.

5.2.2 Personalized Engineered Cornea for Corneal Transplantation
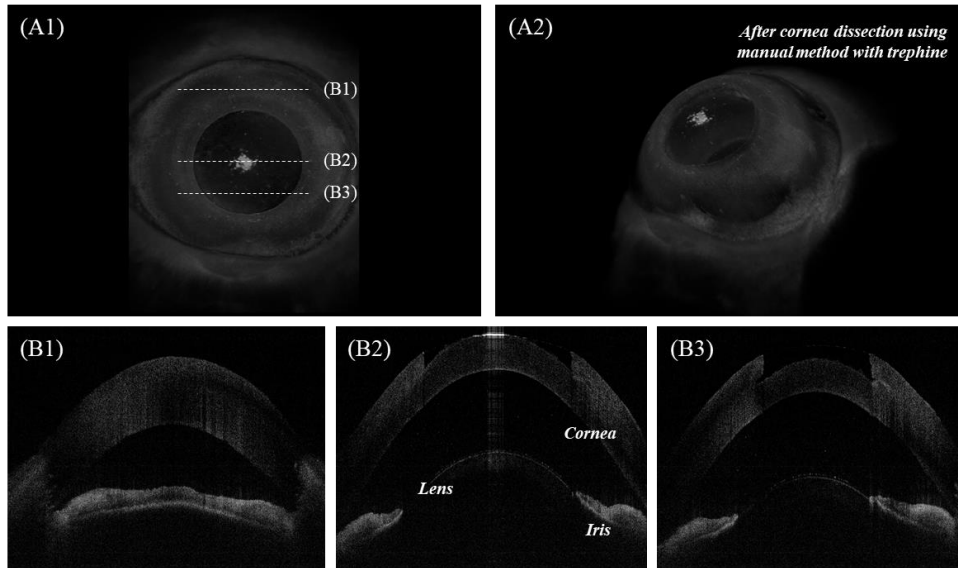
Figure 5-10. OCT image acquisition of 3D cornea structure after the cornea dissection using a manual method with trephine.
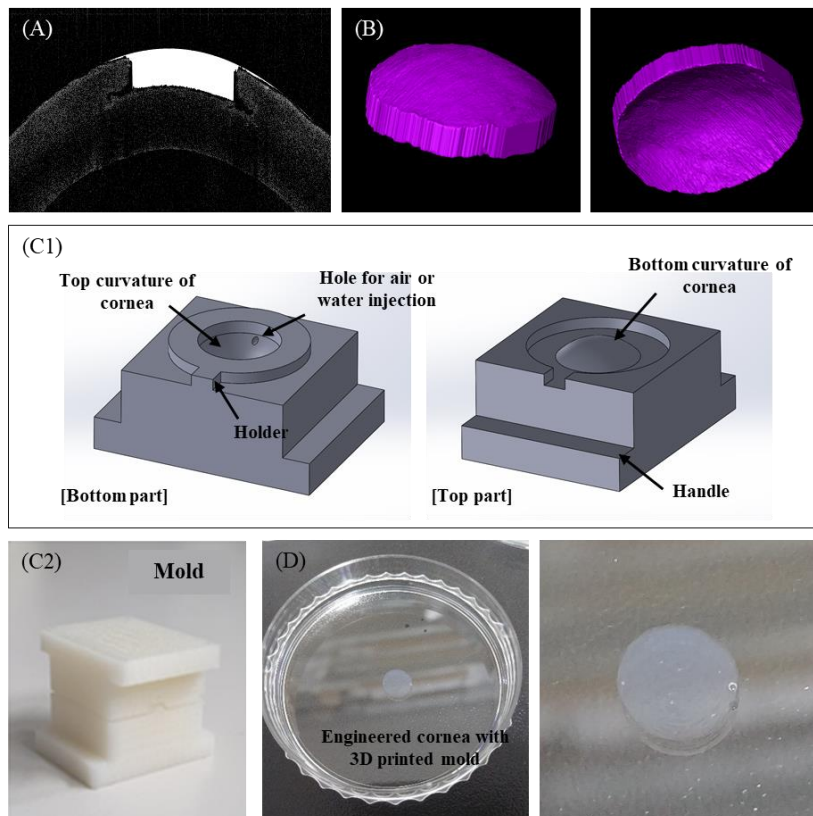
Figure 5-11. (A) Area segmentation results for the regions to be replaced by the engineered cornea, (B) 3D reconstructed cornea structure based on area segmentation, (C1), (C2) Reverse designed mold for engineered cornea fabrication, (D) Fabricated engineered cornea using the 3D printed mold.

Figure 5-10 shows the 3D OCT image of a porcine cornea structure after the corneal dissection using a manual method with a trephine. We acquired a three-dimensional OCT image of the whole cornea structure in the porcine eye and set the surgical area for the cornea transplantation with measurement of diameter and thickness around the center point. In Figure 5-11, we reconstructed the 3D structure based on area segmentation results for the regions to be replaced by the engineered cornea. The 3D structural information was reverse-engineered to create a 3D printed mold using a 3D printer for the fabrication of engineered cornea. In Figure 5-11(C), we designed the mold for engineered cornea fabrication using Solidworks software, and the mold has two different part which has the same curvature of top and bottom surface of the native cornea structure. We perform the process of solidifying and extracting materials between the top and bottom parts of the cornea mold. The engineered cornea fabricated with various material candidates that have similar mechanical and optical properties to the native cornea.
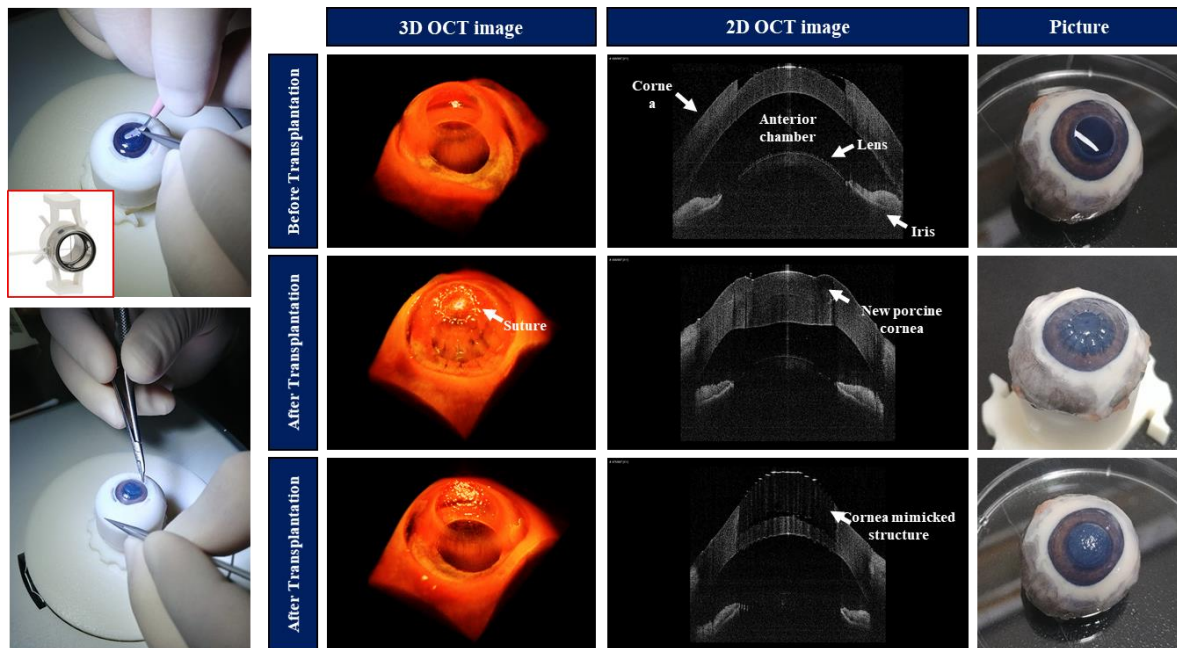
Figure 5-12. Feasibility studies about before and after transplantation with donated porcine cornea and engineered cornea under the 2D and 3D OCT monitoring.

Figure 5-12 presents the OCT monitoring results about before and after transplantation with the donated porcine cornea and engineered cornea. We incised the cornea using the trephine used in corneal surgery and conducted the lamellar keratoplasty on the donate porcine cornea and engineered cornea. The cornea donated by another porcine eye was confirmed in OCT images that there was a deformation after corneal implantation. These problems supported the needs for the personalized engineered cornea that mimicked the native cornea in the issues of vision recovery and the corneal regeneration.

Table 5-1. Evaluation of candidate materials for personalized engineered cornea

Sample	Acrylamide alginate + Acrylate	Acrylamide + Bis-acrylamide	Acrylamide + Bis-acrylamide (high concentration)	PEGDA 400
Evaluation after surgery	- Very weak structure - Broken right into surgical forceps.	- Possible to suture loosely, not tightly - The internal structure is very transparent in OCT, but the surface is well identified	- Structure and transparency are fine - Very weak structure - The internal structure has a contrast in OCT	- Not transparent - Rigid structure: possible to deal with surgical forceps - Broken easily in suture process

Acrylamide + Bis-acrylamide
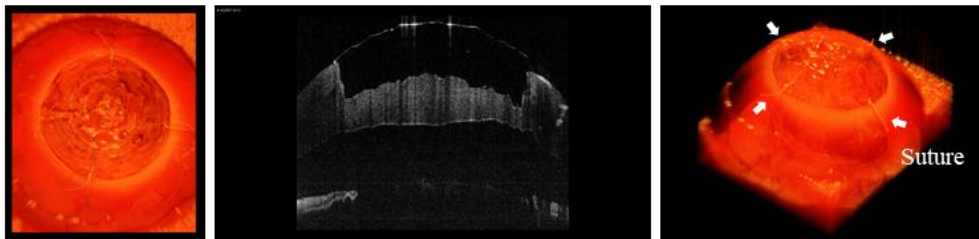
Acrylamide + Bis-acrylamide (high concentration)
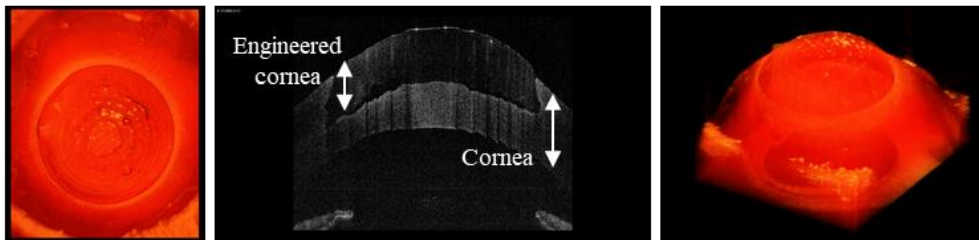
Figure 5-13. Evaluation of candidate materials for personalized engineered cornea in corneal transplantation using the 2D and 3D OCT images.

Table 5-1 and Figure 5-13 present our first pilot study to evaluate candidate materials for personalized engineered cornea. We tried to fabricate the engineered cornea using four different materials as shown in Table 5-1. The group of acrylamide alginate with acrylate and PEGDA (Polyethylene glycol diacrylate) had a difficulty to perform corneal transplantation due to its physical properties. In the group of acrylamide with bis-acrylamide, the engineered cornea was successfully transplanted and the suture was also possible. After the transplantation, we evaluated the completeness of cornea transplantation by scanning the whole corneal tissue in the anterior segment with OCT modality.

Here, we suggested imaging-guided tissue fabrication protocol for personalized engineered cornea which mimicked structural properties of the native cornea. The 3D printed mold was designed for the fabrication of engineered cornea based on personalized factors such as thickness and curvature.

Several candidate materials were used to fabricate the engineered corneas and to assess their suitability for corneal transplantation. The material to be used in the manufacture of the engineered cornea has physical and optical properties and biocompatibility similar to the native cornea. We are currently evaluating the suitability of the development of personalized artificial cornea using a variety of biocompatible materials. It is expected that our pilot study will be applied to fabricate other engineered tissues which are closely mimicked native tissues.

CHAPTER 6. Discussions and Conclusions

6.1 Discussions and Conclusions

In the tissue engineering fields, the need for versatile optical imaging techniques has emerged for the expansion of the research into new applications in a variety of experimental environments. The most important and essential factors for the effective use of optical imaging modality in tissue engineering are continuous monitoring and quantitative analysis of the structural and morphological changes in biological tissues with a volumetric assessment. In this study, we have identified the availability of optical imaging technology in tissue engineering not only for observation of biological tissues, but also for various application studies such as quantitative analysis of tissue regeneration and manipulation as well as tissue fabrication in *ex vivo*, *in vitro*, and *in vivo*.

Optical coherence tomography (OCT) has emerged as the most appropriate candidate for studying skin morphology dynamically and quantitatively. OCT equips optimal imaging characteristics for dynamic skin monitoring because it offers cross-sectional, high-resolution, real-time tissue imaging in a non-invasive manner. Unlike most optical imaging techniques, OCT does not require any contrast agent or labeling process even it provides a deep penetration depth of about 2 mm in the tissue. We utilized 3D OCT imaging to observe the tissue regeneration after laser irradiation, epidermal biopsy, and skin incision in *in vitro* and *in vivo* skin model. First, we have demonstrated quantitative OCT in a laser wound recovery study. Experimental results showed that the wound healing process is active in the vertical direction, and recovery time varies by the tissue structure as well as the irradiation condition. Also, we presented a quantitative evaluation of drug efficiency that affect the wound recovery on the engineered skin model after epidermal biopsy using the OCT imaging modality. We evaluated the wound regeneration according to the concentration of madecassoside and chondroitin sulfate in epidermal biopsied engineered skin. It was also confirmed that the same substance may interfere with the recovery of the wound depending on the concentration. OCT modality can provide the optimum conditions such as concentration and treated time for most effective wound regeneration in efficacy assessment and evaluation of engineered skin. Then, we analyzed quantitatively the effects of tissue adhesive on the wound recovery of skin incised rat model using chitosan-based tissue adhesive and OCT imaging system. We monitored how the chitosan-based tissue adhesive affected wound regeneration compared with fibrin which is one of the conventional tissue adhesives and a suture used for stitching up the wound as a control group. We confirmed that the tissue adhesive treated group enclosed the wound in the early stage, and it accelerated faster wound regeneration than the untreated group. Also, we demonstrated the wound recovery tendency of chitosan-based adhesive relative to suture or fibrin.

In order to observe the changes in sub-cellular level, which is difficult to observe with OCT imaging, we observed and quantitatively analyzed the morphological changes of biological tissue using optical coherence microscopy (OCM) imaging modality. For evaluation of the histopathological analysis using OCM, we observed the development of hair follicles and conducted a comparison study with the tissue staining method. We confirmed that OCM provided excellent contrast for various structures within the skin. Also, we observed the detailed structure of hair and hair follicles in OCM *en-face* images such as hair bulb, hair root, hair papilla, and hair follicle wall consisted of the epidermal and dermal sheath. Even if the specimen had height deviation on the surface or it was tilted very slightly by a few tens or hundreds of micrometers out of the depth-of-focus, it had a sensitive and decisive influence on incorrect image acquisition such as signal loss, inhomogeneous intensity and discrete artifact between each mosaic image pieces. Therefore, we introduced depth trajectory-tracking technique to acquire homogenous quality OCM images regardless of the height difference of the sample surface. In the next step, we developed the serial block-face OCM (SB-OCM) system for obtaining high-resolution three-dimensional tissue images by applying the serial block-face technology to the mosaic based large field-of-view OCM. The SB-OCM system was made in the automated system performing a large field-of-view optical imaging and physical tissue sectioning of the agarose-embedded tissue. To evaluate the deep tissue imaging capability, we tried to image various mouse organs including the brain, liver, kidney, and heart. We confirmed morphological structures in various tissues, for example, fiber networks in the brain, micro-vessels in kidney and liver, and fibrous tissue in heart and muscle. The SB-OCM shows only two simple processes; imaging and slicing, but it has great advantages such as different image contrast, large field of view, and deep penetration imaging depth compared with existing methods.

A hand-held probe-based portable OCT system was developed for use in human target study away from the bench-top system in the laboratory. The bench-top type imaging equipment has difficulty to access image acquisition in the human target study. We developed a hand-held probe to overcome these problems. The hand-held probe can be conveniently accessed by users, and image acquisition is possible regardless of the shape or position of the target. Here, we monitored and quantitatively analyzed various changes in the human skin using the hand-held probe based portable OCT system. First, we studied quantitative analysis of volumetric information in human skin wrinkle. With the development of dermatological treatment and anti-aging process such as reducing wrinkles have attracted worldwide attention. However, there has been no automatic platform for detecting and visualizing the wrinkles quantitatively. We suggested a novel algorithm for automated quantification of skin wrinkles and delivered quantitative information of winkles in terms of depth and volume. Also, we quantified the roughness of skin wrinkles using OCT for comparison with PRIMOS, a traditional crease analysis method. We demonstrated the potential of OCT based on flattening image processing for monitoring quantitative skin roughness. Experimental results of phantom study showed that OCT

is reliable to the angle of the subject and compact wrinkle structure compared to one acquired from PRIMOS. We also investigated that OCT is adequate for monitoring wrinkle morphology changes *in vivo*. Through our results, we found that OCT would be a useful tool to deliver comprehensive and intuitive information in dynamic skin observations, since OCT enables observing quantitative skin topology and volumetric skin anatomy simultaneously.

We conducted the experiment to fabricate the engineered tissue based on two- and three-dimensional information of optical imaging in previously acquired in biological tissues. Here, we suggested a fabrication of wrinkle mimicked engineered skin for anti-aging assessment and a protocol of imaging guided personalized engineered cornea for cornea transplantation. For the study of skin anti-aging with high clinical effects, it is important to develop a new model of engineering skin that has the form of wrinkles and curvature, not the current flat and simple layered structure. We could observe the possibility of mimicking wrinkles or curvature on the engineered skin with dermal layer shaping techniques using 3D printed patterned molds. However, most of the processes from the shape of the mold pattern to engineered skin culture were related to the formation of wrinkles and curvature, which required very careful adjustment. We established experimental conditions in which a certain type of wrinkle can be formed through multiple iterations, and we intend to establish and utilize the desired form and the model of wrinkles with repeatability and reproducibility through further studies. Since there are no skin equivalent models to study wrinkles at the cell level to date, we expect that future optimization and verification will play a very important role in skin anti-aging research and development. We also tried to fabricate engineered cornea to mimic the structural, physical and optical characteristics of the native cornea as well as its structure. First, we acquired a three-dimensional OCT image of whole cornea structure in the porcine eye and set the surgical area for the cornea transplantation with measurement of diameter and thickness around the center point. We reconstructed the 3D structure of the surgical area to be peeled using the image processing based on previously acquired information. The 3D structural information was reverse-engineered to create a 3D printed mold for the fabrication of engineered cornea. It is expected that the new fabrication platform based on OCT imaging and 3D printing would be promising tool to provide not only engineered cornea, but also various personalized tissues.

6.2 Future Perspectives

Here, we utilized optical imaging techniques to carry out application research ranging from the observation of biological tissues, dynamic monitoring, and quantitative analysis, as well as fabrication of image-based engineered tissue. In particular, we were able to obtain various quantitative information from the biological tissues by utilizing the advantages of OCT imaging technology such

as high-resolution, non-invasive, label-free, deep penetration depth with real-time imaging. These characteristics of OCT imaging enables the quantitative analysis of tissue recovery and replacement in tissue engineering studies or the role of a guide in tissue manipulation. As we mentioned in the last chapter, the development of engineered tissues in tissue engineering research is very important and at the same time, many studies are actively conducted. However, not many studies have been conducted on the development of engineered tissues that mimic the architectural or physical characteristics of native tissues. The image information of medical devices such as CT and MRI is already used in the manufacture of artificial skeletons, and if the engineered tissue is developed based on optical imaging information such as OCT, many advances and research achievements are expected in terms of the efficacy evaluation in the engineered tissues and reproducibility of experiments.

REFERENCES

1. Appel, A.A., et al., *Imaging challenges in biomaterials and tissue engineering.* Biomaterials, 2013. **34**(28): p. 6615-6630.

2. Sun, Y., et al., *Imaging tissue engineering scaffolds using multiphoton microscopy.* Microscopy research and technique, 2008. **71**(2): p. 140-145.

3. Zhang, Y.S. and J. Yao, *Imaging Biomaterial–Tissue Interactions.* Trends in biotechnology, 2018. **36**(4): p. 403-414.

4. Gil, C.J., et al., *In Vivo Tracking of Tissue Engineered Constructs.* Micromachines, 2019. **10**(7): p. 474.

5. Nam, S.Y., et al., *Imaging strategies for tissue engineering applications.* Tissue Engineering Part B: Reviews, 2014. **21**(1): p. 88-102.

6. Dhawan, A.P., B. D'Alessandro, and X. Fu, *Optical imaging modalities for biomedical applications.* IEEE reviews in biomedical engineering, 2010. **3**: p. 69-92.

7. Wilson, B.C., M. Jermyn, and F. Leblond, *Challenges and opportunities in clinical translation of biomedical optical spectroscopy and imaging.* Journal of biomedical optics, 2018. **23**(3): p. 030901.

8. Teodori, L., et al., *Three-dimensional imaging technologies: a priority for the advancement of tissue engineering and a challenge for the imaging community.* Journal of biophotonics, 2017. **10**(1): p. 24-45.

9. Dunkers, J.P., M.T. Cicerone, and N. Washburn, *Collinear optical coherence and confocal fluorescence microscopies for tissue engineering.* Optics Express, 2003. **11**(23): p. 3074-3079.

10. Sands, G.B., et al., *Automated imaging of extended tissue volumes using confocal microscopy.* Microscopy research and technique, 2005. **67**(5): p. 227-239.

11. Lin, S.-J., et al., *Evaluating cutaneous photoaging by use of multiphoton fluorescence and second-harmonic generation microscopy.* Optics letters, 2005. **30**(17): p. 2275-2277.

12. Coulman, S.A., et al., *In vivo, in situ imaging of microneedle insertion into the skin of human volunteers using optical coherence tomography.* Pharmaceutical research, 2011. **28**(1): p. 66-81.

13. Fujimoto, J.G., *Optical coherence tomography for ultrahigh resolution in vivo imaging.* Nature biotechnology, 2003. **21**(11): p. 1361.

14. Ahn, Y., et al., *Quantitative monitoring of laser-treated engineered skin using optical coherence tomography.* Biomedical optics express, 2016. **7**(3): p. 1030-1041.

15. Kim, M., et al., *In situ facile-forming chitosan hydrogels with tunable physicomechanical and tissue adhesive properties by polymer graft architecture.* Carbohydrate Polymers, 2019: p. 115538.

16.   Huang, D., et al., *Optical coherence tomography.* science, 1991. **254**(5035): p. 1178-1181.

17.   Welzel, J., et al., *Optical coherence tomography of the human skin.* Journal of the American Academy of Dermatology, 1997. **37**(6): p. 958-963.

18.   Gangatirkar, P., et al., *Establishment of 3D organotypic cultures using human neonatal epidermal cells.* Nature protocols, 2007. **2**(1): p. 178.

19.   Schmitt, R., et al. *Optical coherence tomography investigation of growth cycles of engineered skin tissue*. in *Optics in Tissue Engineering and Regenerative Medicine IV*. 2010. International Society for Optics and Photonics.

20.   Jung, W., et al., *Optical coherence tomography for in vitro monitoring of wound healing after laser irradiation.* IEEE Journal of selected topics in quantum electronics, 2003. **9**(2): p. 222-226.

21.   Yeh, A.T., et al., *Imaging wound healing using optical coherence tomography and multiphoton microscopy in an in vitro skin-equivalent tissue model.* Journal of biomedical optics, 2004. **9**(2): p. 248-253.

22.   Bernstein, L.J., et al., *The short-and long-term side effects of carbon dioxide laser resurfacing.* Dermatologic Surgery, 1997. **23**(7): p. 519-525.

23.   Graber, E.M., E.L. Tanzi, and T.S. Alster, *Side effects and complications of fractional laser photothermolysis: experience with 961 treatments.* Dermatologic Surgery, 2008. **34**(3): p. 301-307.

24.   Brown, E., et al., *Dynamic imaging of collagen and its modulation in tumors in vivo using second-harmonic generation.* Nature medicine, 2003. **9**(6): p. 796.

25.   Calzavara-Pinton, P., et al., *Reflectance confocal microscopy for in vivo skin imaging.* Photochemistry and photobiology, 2008. **84**(6): p. 1421-1430.

26.   Petroll, W.M., H.D. Cavanagh, and J.V. Jester, *Dynamic three-dimensional visualization of collagen matrix remodeling and cytoskeletal organization in living corneal fibroblasts.* Scanning: The Journal of Scanning Microscopies, 2004. **26**(1): p. 1-10.

27.   Matsui, T. and M. Amagai, *Dissecting the formation, structure and barrier function of the stratum corneum.* International immunology, 2015. **27**(6): p. 269-280.

28.   Tsai, M.-T., et al., *Monitoring of wound healing process of human skin after fractional laser treatments with optical coherence tomography.* Biomedical optics express, 2013. **4**(11): p. 2362-2375.

29.   Sattler, E.C.E., et al., *Confocal laser scanning microscopy and optical coherence tomography for the evaluation of the kinetics and quantification of wound healing after fractional laser therapy.* Journal of the American Academy of Dermatology, 2013. **69**(4): p. e165-e173.

30.   Banzhaf, C.A., et al., *Spatiotemporal closure of fractional laser-ablated channels imaged by optical coherence tomography and reflectance confocal microscopy.* Lasers in surgery and

medicine, 2016. **48**(2): p. 157-165.

31. Varkey, M., J. Ding, and E.E. Tredget, *Superficial dermal fibroblasts enhance basement membrane and epidermal barrier formation in tissue-engineered skin: implications for treatment of skin basement membrane disorders.* Tissue Engineering Part A, 2013. **20**(3-4): p. 540-552.

32. Catalano, E., et al., *Tissue-engineered skin substitutes: an overview.* Journal of Artificial Organs, 2013. **16**(4): p. 397-403.

33. Doke, S.K. and S.C. Dhawale, *Alternatives to animal testing: A review.* Saudi Pharmaceutical Journal, 2015. **23**(3): p. 223-229.

34. Sherwin, C.M., et al., *Guidelines for the ethical use of animals in applied ethology studies.* Applied Animal Behaviour Science, 2003. **81**(3): p. 291-305.

35. Ahn, S., et al., *Designed three-dimensional collagen scaffolds for skin tissue regeneration.* Tissue Engineering Part C: Methods, 2009. **16**(5): p. 813-820.

36. Zhang, Z. and B.B. Michniak-Kohn, *Tissue engineered human skin equivalents.* Pharmaceutics, 2012. **4**(1): p. 26-41.

37. Li, Z., et al., *Increased cutaneous wound healing effect of biodegradable liposomes containing madecassoside: preparation optimization, in vitro dermal permeation, and in vivo bioevaluation.* International journal of nanomedicine, 2016. **11**: p. 2995.

38. Liu, M., et al., *Anti-rheumatoid arthritic effect of madecassoside on type II collagen-induced arthritis in mice.* International Immunopharmacology, 2008. **8**(11): p. 1561-1566.

39. Im, A.-R., et al., *Wound healing and antibacterial activities of chondroitin sulfate-and acharan sulfate-reduced silver nanoparticles.* Nanotechnology, 2013. **24**(39): p. 395102.

40. Ghatak, S., et al., *Roles of proteoglycans and glycosaminoglycans in wound healing and fibrosis.* International journal of cell biology, 2015. **2015**.

41. Han, H.H. and J.W. Rhie, *Surgical sealants, glues and adhesive agents in the medical market.* Journal of the Korean Medical Association, 2014. **57**(7): p. 609-613.

42. Izatt, J.A., et al., *Optical coherence microscopy in scattering media.* Optics letters, 1994. **19**(8): p. 590-592.

43. Min, E., et al., *Wide-field optical coherence microscopy of the mouse brain slice.* Optics letters, 2015. **40**(19): p. 4420-4423.

44. Rompolas, P., et al., *Live imaging of stem cell and progeny behaviour in physiological hair-follicle regeneration.* Nature, 2012. **487**(7408): p. 496.

45. Blume-Peytavi, U., K. Hillmann, and M. Guarrera, *Hair growth assessment techniques*, in *Hair growth and disorders*. 2008, Springer. p. 125-157.

46. Chamberlain, A.J. and R.P. Dawber, *Methods of evaluating hair growth.* Australasian journal of dermatology, 2003. **44**(1): p. 10-18.

47. Prost-Squarcioni, C., *Histology of skin and hair follicle.* Medecine sciences: M/S, 2006. **22**(2): p. 131-137.

48. Zhang, K., et al., *A surface topology and motion compensation system for microsurgery guidance and intervention based on common-path optical coherence tomography.* IEEE Transactions on Biomedical Engineering, 2009. **56**(9): p. 2318-2321.

49. Ragan, T., et al., *High-resolution whole organ imaging using two-photon tissue cytometry.* Journal of biomedical optics, 2007. **12**(1): p. 014015.

50. Ragan, T., et al., *Serial two-photon tomography for automated ex vivo mouse brain imaging.* Nature methods, 2012. **9**(3): p. 255.

51. Rylander, C.G., et al., *Dehydration mechanism of optical clearing in tissue.* Journal of biomedical optics, 2006. **11**(4): p. 041117.

52. Costantini, I., et al., *In-vivo and ex-vivo optical clearing methods for biological tissues.* Biomedical optics express, 2019. **10**(10): p. 5251-5267.

53. Wong, T.T., et al., *Label-free automated three-dimensional imaging of whole organs by microtomy-assisted photoacoustic microscopy.* Nature communications, 2017. **8**(1): p. 1386.

54. Chung, K. and K. Deisseroth, *CLARITY for mapping the nervous system.* Nature methods, 2013. **10**(6): p. 508.

55. Richardson, D.S. and J.W. Lichtman, *Clarifying tissue clearing.* Cell, 2015. **162**(2): p. 246-257.

56. Amunts, K., et al., *BigBrain: an ultrahigh-resolution 3D human brain model.* Science, 2013. **340**(6139): p. 1472-1475.

57. Geyer, S.H., et al., *High-Resolution Episcopic Microscopy (HREM)-simple and robust protocols for processing and visualizing organic materials.* JoVE (Journal of Visualized Experiments), 2017(125): p. e56071.

58. Ramirez, D.M., et al., *Serial multiphoton tomography and analysis of volumetric images of the mouse brain*, in *Multiphoton Microscopy*. 2019, Springer. p. 195-224.

59. Farage, M.A., K.W. Miller, and H.I. Maibach, *Textbook of aging skin*. 2009: Springer Science & Business Media.

60. Trojahn, C., et al., *Measuring skin aging using optical coherence tomography in vivo: a validation study.* Journal of biomedical optics, 2015. **20**(4): p. 045003.

61. Sakai, S., et al., *In vivo evaluation of human skin anisotropy by polarization-sensitive optical coherence tomography.* Biomedical optics express, 2011. **2**(9): p. 2623-2631.

62. Grove, G.L., M.J. Grove, and J.J. Leyden, *Optical profilometry: an objective method for quantification of facial wrinkles.* Journal of the American Academy of Dermatology, 1989. **21**(3): p. 631-637.

63. Friedman, P.M., et al., *3D in-vivo optical skin imaging for topographical quantitative assessment of non-ablative laser technology.* Dermatologic surgery, 2002. **28**(3): p. 199-204.

64.   Iftimia, N., et al., *Combined reflectance confocal microscopy/optical coherence tomography imaging for skin burn assessment.* Biomedical optics express, 2013. **4**(5): p. 680-695.

65.   Koehler, M.J., et al., *In vivo assessment of human skin aging by multiphoton laser scanning tomography.* Optics letters, 2006. **31**(19): p. 2879-2881.

66.   Fujimura, T., et al., *Global and systematic demonstration for the practical usage of a direct in vivo measurement system to evaluate wrinkles.* International journal of cosmetic science, 2007. **29**(6): p. 423-436.

67.   Jacobi, U., et al., *In vivo determination of skin surface topography using an optical 3D device.* Skin Research and Technology, 2004. **10**(4): p. 207-214.

68.   Askaruly, S., et al., *Quantitative evaluation of skin surface roughness using optical coherence tomography in vivo.* IEEE Journal of Selected Topics in Quantum Electronics, 2018. **25**(1): p. 1-8.

69.   Wang, Z., et al., *Cubic meter volume optical coherence tomography.* Optica, 2016. **3**(12): p. 1496-1503.

70.   Taghavikhalilbad, A., et al., *Semi-automated localization of dermal epidermal junction in optical coherence tomography images of skin.* Applied optics, 2017. **56**(11): p. 3116-3121.

71.   Xu, D., Y. Huang, and J.U. Kang, *Real-time compressive sensing spectral domain optical coherence tomography.* Optics letters, 2014. **39**(1): p. 76-79.

72.   Doillon, C., et al., *A collagen-based scaffold for a tissue engineered human cornea: physical and physiological properties.* The International journal of artificial organs, 2003. **26**(8): p. 764-773.

73.   Shah, A., et al., *The development of a tissue-engineered cornea: biomaterials and culture methods.* Pediatric research, 2008. **63**(5): p. 535.